Electronic Theses and Dissertations

Theses, Dissertations, and Major Papers

10-5-2017

Thermal Management of Lithium-ion Battery Modules for Electric Vehicles

Farid Bahiraei
University of Windsor

Thermal Management of Lithium-ion Battery Modules for Electric Vehicles

By

Farid Bahiraei

A Dissertation
Submitted to the Faculty of Graduate Studies
through the Department of Mechanical, Automotive & Materials Engineering
in Partial Fulfillment of the Requirements for
the Degree of **Doctor of Philosophy**
at the University of Windsor

Windsor, Ontario, Canada

2017

Thermal Management of Lithium-ion Battery Modules for Electric Vehicles

by

Farid Bahiraei

APPROVED BY:

_____
S. Putatunda

External Examiner, Wayne State University

_____
G. Rankin
Department of Mechanical, Automotive & Materials Engineering

_____
N. Zamani
Department of Mechanical, Automotive & Materials Engineering

_____
R. Riahi
Department of Mechanical, Automotive & Materials Engineering

_____
A. Fartaj, Co-Advisor
Department of Mechanical, Automotive & Materials Engineering

_____
G. Nazri, Co-Advisor
Department of Electrical and Computer Engineering

September 15, 2017

DECLARATION OF CO-AUTHORSHIP/PREVIOUS PUBLICATION

I. Co-Authorship Declaration

I hereby declare that this thesis incorporates material that is result of my research under the supervision of Dr. Amir Fartaj and Dr. Gholam-Abbas Nazri, University of Windsor. In chapters 2-7, the key ideas, primary contributions, experimental designs, data analysis and interpretation, were performed by the author, and the contribution of Dr. Fartaj and Dr. Nazri was primarily through the provision of supervision. Ms. Ghalkhani collaboration is covered in the chapters 3 and 6 of the dissertation.

I am aware of the University of Windsor Senate Policy on Authorship and I certify that I have properly acknowledged the contribution of other researchers to my thesis, and have obtained written permission from each of the co-author(s) to include the above material(s) in my thesis.

I certify that, with the above qualification, this thesis, and the research to which it refers, is the product of my own work.

II. Declaration of Previous Publication

This thesis includes 5 original papers that have been previously published/submitted for publication, as follows:

Thesis Chapter	Publication title/full citation	Publication status
Chapter 2	Farid Bahiraei, Amir Fartaj, Gholam-Abbas Nazri, "Numerical investigation of active and passive cooling systems of a lithium-ion battery module for electric vehicles", SAE Technical Paper 2016-01-0655, SAE World Congress, 2016	*Published*
Chapter 3	Farid Bahiraei, Maryam Ghalkhani, Amir Fartaj, Gholam-Abbas Nazri, "A pseudo 3D electrochemical-thermal modeling and analysis of a lithium-ion battery for electric vehicle thermal management applications", Applied Thermal Engineering	*Published*
Chapter 4	Farid Bahiraei, Amir Fartaj, Gholam-Abbas Nazri, "Electrochemical-thermal Modeling to Evaluate Active Thermal Management of a Lithium-ion Battery Module", Electrochimica Acta	*Accepted*

Chapter 5	Farid Bahiraei, Amir Fartaj, Gholam-Abbas Nazri, "Experimental and numerical investigation on the performance of carbon-based nanoenhanced phase change materials for thermal management applications", Energy Conversion and Management	*Submitted*
Chapter 6	Farid Bahiraei, Maryam Ghalkhani, Amir Fartaj, Gholam-Abbas Nazri, "An integrated thermal management system for lithium-ion battery modules with nano-enhanced phase change materials and highly oriented pyrolytic graphite", Energy	*Submitted*

I certify that I have obtained a written permission from the copyright owner(s) to include the above published material(s) in my thesis. I certify that the above material describes work completed during my registration as graduate student at the University of Windsor.

I declare that, to the best of my knowledge, my thesis does not infringe upon anyone's copyright nor violate any proprietary rights and that any ideas, techniques, quotations, or any other material from the work of other people included in my thesis, published or otherwise, are fully acknowledged in accordance with the standard referencing practices. Furthermore, to the extent that I have included copyrighted material that surpasses the bounds of fair dealing within the meaning of the Canada Copyright Act, I certify that I have obtained a written permission from the copyright owner(s) to include such material(s) in my thesis.

I declare that this is a true copy of my thesis, including any final revisions, as approved by my thesis committee and the Graduate Studies office, and that this thesis has not been submitted for a higher degree to any other University or Institution.

ABSTRACT

This research is particularly focused on studying thermal management of lithium-ion (Li-ion) battery modules in electric vehicles by using active, passive and hybrid active-passive methods. The thermal behavior prediction of batteries is performed by a novel electrochemical-thermal model. Different approaches such as single- and double-channel liquid cooling, pure passive by using phase change materials (PCM), and hybrid active-passive thermal management systems are investigated. Various cooling system configurations are examined to expand understanding of effect of each approach on the battery module thermal responses during a standard driving cycle. It is observed that the temperature distribution of Li-ion batteries is strongly influenced by the electrical and thermal operating conditions and simplified bulk models cannot precisely predict the thermal behavior of these batteries.

Additionally, the PCM-based passive systems show advantages such as compactness and simplicity over the active liquid cooling systems. However, these systems suffer from non-uniform temperature distribution due to inherently low thermal conductivity of organic PCM. An effort has been made to enhance the thermal conductivity of a paraffin wax by adding various carbon-based nanoparticles. The results revealed that the thermal conductivity of the base PCM can be improved by about 11 times when using 10% mass fraction of graphite nanopowder. The heat transfer in the nano-enhanced PCM samples showed that the presence of nanoparticles drastically repress the natural convection in the melted nanocomposites.

Among the battery thermal management systems studied, the air assisted hybrid cooling system provides the best temperature distribution uniformity in the module while keeping the batteries temperature within the safe limits. Furthermore, this work attempted to recognize the most influential parameters on the temperature distribution in the battery module. It is seen that the thickness of cooling plates and PCM layers in active and hybrid systems has a significant effect on the thermal behavior of the batteries.

DEDICATION

To my family

ACKNOWLEDGEMENTS

TABLE OF CONTENTS

LIST OF TABLES

LIST OF FIGURES

xv

Chapter 1 INTRODUCTION

1.1. Motivation and Background

High efficiency energy conversion is one of the most significant challenges for today's world due to environmental concerns and depleting resources. Intensive research activities are being conducted throughout the world for thermal management enhancement to meet industry needs. While industry remains committed to the evaluation of alternatives in these areas; technology likely will be judged in three critical criteria: environmental effects, safety, and cost. A primary consideration is the influence on the environment and global warming. Recent evaluations show that Canada is warming at a faster rate than most regions in the world [1]. The transportation, buildings and electricity sectors are responsible for about half of Canada's total greenhouse gas (GHG) emission in 2015 [2].

Developing full electric vehicles (EV) and hybrid electric vehicles (HEV) can reduce the amount of GHG emissions due to lower fossil fuel consumption. These vehicles are the best candidates in the transportation sector to address air quality and climate change while promoting sustainable energy development. In both HEV and EV, the battery pack is the key component to reduce GHG emission.

Lithium-ion (Li-ion) batteries show advantages such as high energy density, high power, environmental adaptability and longer lifespan compared to other battery chemistries. Moreover, Li-ion batteries are offering further benefits such as rapid charging, high load capabilities, and low self-discharge. These traits make the lithium batteries the most promising technology for use in the EV and HEV [3–5].

The main barriers to the wide use of Li-ion batteries in electric vehicles are safety, cost related to cycle and calendar life, and low temperature performance [6]. These challenges are strongly coupled to the thermal behavior and non-uniform temperature distribution in the battery and may reduce its performance and lifetime [7,8] or lead to thermal runaway [9]. Thermal runaway is one of the most catastrophic safety issues of lithium-ion batteries, where multiple cells in a battery fail due to an individual cell failure. Numerical investigations showed that conductivity of the electrolyte increases with temperature, causing more current to be directed to hotter regions of the battery. This generates more heat which raises the temperature and allowing even more current to pass through it. This positive feedback has the potential to lead to thermal runaway [10]. Hence, the numerical simulation of Li-ion batteries is essential in developing an understanding of thermal behavior of these batteries in order to enhance their application in the EV and HEV.

Several active and passive methods have been utilized for the thermal management of Li-ion batteries and improving their performance and safety such as air cooling, liquid

cooling, and using phase change materials (PCM) [11,12]. Forced air cooling can moderate the batteries temperature rise, but in large battery packs, aggressive driving cycles and/or at high operating temperatures it will result in a large non-uniform temperature distribution in the module [13]. Liquid cooling using water, oil or refrigerants as the heat transfer medium demonstrates better thermal efficiency due to the higher heat capacity of liquids compared to air. However, these systems require complex control strategies and refrigeration cycles [14].

The passive PCM-based cooling of batteries benefits from advantages such as high compactness, low cost, no need for circulatory network, desired cooling effect and better performance in case of thermal run away. Despite these advantages, there are some drawbacks in this method such as volume and weight increase of the battery system, heat accumulation in the PCM and unfavorable thermal inertia [15].

Choosing the most suitable cooling scenario to obtain the best thermal performance is challenging due to the advantages and drawbacks of various battery thermal management systems (BTMS). The electrical performance and capacity fading of Li-ion batteries are strong functions of their temperature-dependent electrochemical performance. Therefore, to achieve the optimal vehicle operation an appropriate coupled electrochemical-thermal model of BTMS is vital. The objective of this dissertation is to develop such a coupled model and to investigate the effects of various thermal management strategies on the thermal behavior of battery modules. The outcomes of this work are expected to improve the understanding of the electrochemical-thermal performance of Li-ion batteries which helps the battery and BTMS designers to optimize the temperature control methods in EV and HEV.

1.2. Dissertation Objective and Overview

The ultimate objective of the current research is to develop a computationally affordable electrochemical-thermal modeling tool to investigate the effects of various thermal management scenarios on the performance of Li-ion battery modules in HEV. To achieve this goal, a set of numerical models are developed and the results are validated with the experimental data obtained from this study. The scope of this research work includes:

1. Develop battery electrical and thermal characterization experiment protocols to collect the data required for generating the coupled models.
2. Establish a fast simulation 3D electrochemical-thermal coupled model to use in the thermal management system studies. The coupled models demand large computational times due to the highly nonlinear electrochemical governing equations. Therefore, thermal management investigations in the module and pack levels are mainly conducted either by lumped thermal models with heat generation data obtained from experiment data or equivalent circuit models.

However, accurate assessment of battery electrical and thermal responses to different cooling scenarios needs 3D coupled electrochemical-thermal models.

3. Provide an in-depth insight of the current density and temperature distribution in Li-ion batteries components to provide an understanding of interactions between the electrochemical and thermal behavior of Li-ion batteries under dynamic loading currents

4. Employ the streamlined coupled battery model in active cooling systems to assess the effects of operating and design parameters on the thermal behavior of batteries.

5. Develop an experimental procedure to synthesis and characterization of nano-engineered phase change materials to use in passive or hybrid BTMS. The efforts are focused on thermal conductivity enhancement of organic PCM.

6. Study the phase change heat transfer in the PCM nanocomposites to obtain an understanding of the effects of additives on the conductive and convective heat transfer in these materials.

7. Investigate the effects of developed nano-enhanced PCM (NePCM) on the thermal responses of a battery module under driving cycles. The effects of materials formulation and thickness on the temperature distribution in the battery module are studied.

Different steps of the current research work are explained in the chapters of this dissertation. An overview of these chapters is as follows:

Chapter 1 (Introduction, current chapter)

The motivation, objective and an overview of the dissertation are presented.

Chapter 2

This chapter introduces the Li-ion battery thermal issues and examines the parameters affecting the battery temperature distribution under constant current discharge. A simplified electrochemical-thermal battery simulation model is described and the feasibility of this model in both active and passive thermal management systems is investigated. The Li-ion thermal issues and a comparison between liquid- and PCM-based BTMS are presented in this section. Chapter 2 also summarizes the effective heat capacity method to model the phase change in the PCM.

Chapter 3

In this chapter, the pseudo 3D coupled model is improved to consider the effects of current collecting tabs on the current density and temperature distribution in the battery. The verification of the electrical and thermal predictions is carried out by comparing the

numerical results with experimental data from a 4Ah NCA prismatic battery. The electrochemical model is solved in 1D to make the coupled model streamlined enough to be embedded into BTMS. The Ohmic heat generation and heat conduction in the cells are evaluated in 3D to investigate the non-uniform temperature distribution during the battery operation. The dependency of different heat generation contributions on the current load and their distribution along the battery thickness are investigated in details.

The developed model featured a greater degree of accuracy in predicting battery thermal responses compared with the lumped or empirical thermal models. The results also showed that temperature gradients along the battery thickness direction can be considerable even in the case of high forced convection cooling.

Chapter 4

In this chapter, the fast simulation coupled model is employed in an active liquid cooled thermal management system. Two BTMS designs are considered and their module temperature distribution under a driving cycle is investigated. The average and maximum temperature of batteries, their temperature uniformity and added volume of both cooling systems are compared. The effects of cooling plate thickness and coolant Reynolds number on the thermal behavior of batteries are studied by using a series of coupled heat transfer, electrochemical-thermal, and flow dynamics simulations.

The results revealed that at identical Reynolds number and cooling plate thickness, the BTMS with two cooling channels leads to a lower maximum and average temperature, and more uniform temperature distribution. It is also observed that there is a trade-off between the batteries temperature rise and uniformity which should be considered in the design of liquid cooling systems.

Chapter 5

The results of chapter 2 showed that using the PCM-based cooling approach may result in deficient temperature control due to the low thermal conductivity of these materials. In this section, three types of carbon-based nanostructures are embedded in a paraffin wax to enhance the thermal conductivity of the based material. 12 nanocomposites are prepared by adding carbon nanofiber, graphene nanoplatelets and graphite nanopowder with mass fractions from 2.5% to 10%. An identical preparation method is used for all nanocomposites to provide a framework for comparing the effects of nanoparticles morphology on the thermophysical properties of the based PCM. The temperature-dependent thermal conductivity, specific and latent heats, as well as dynamic viscosity of nanocomposites are measured.

The experimental and numerical investigations of the thermal behavior of nanocomposites during the melting process are performed. It is shown that the

nanoparticles matrices severely degrade natural convection heat transfer in the liquid phase which may lead to a weaker temperature control compared to the pure paraffin.

The results of this chapter suggest that there is a trade-off between the degradation of natural convection and increase in thermal conductivity caused by nanoparticles that should be considered in PCM-based thermal management systems design. Furthermore, monitoring the temperature distribution in the nanocomposites shows that the NePCM samples can provide a better temperature control with consuming 18% less latent heat capacity of the system as compared to the pure wax.

Chapter 6

In this chapter, two of the nanocomposites examined in chapter 5 are used in a new hybrid thermal management system for Li-ion battery modules. Layers of 5% and 10% graphite-based nanocomposites with various thicknesses are employed in a module to investigate the effects of NePCM formulation and geometry on the thermal responses of batteries.

The heat accumulation in PCM due to ineffective cooling and added thermal inertia of these materials may lead to the thermal management system failure. In this chapter, a hybrid air-cooled active-passive thermal management system is developed to address the raising concerns regarding the potential failures of passive PCM-based thermal management systems. The fast simulation coupled electrochemical-thermal model is used to find the batteries heat generation during a standard driving cycle.

Two techniques are used to enhance the thermal conductivity of the pure PCM by utilizing graphite nanopowder and highly oriented pyrolytic graphite sheets. The effects of mass fraction of NePCM, thickness of PCM layer, and air inlet temperature on the module temperature distribution are investigated. The proposed compact hybrid BTMS offers excellent temperature uniformity among batteries in the module by using a constant air flow during the driving cycle.

Chapter 7 (Conclusion)

The final chapter attempts to synthesize the work in previous chapters and summarize the results obtained in chapters 2 to 6. It also suggests some strategies for next steps.

References

[1]   K.G. Palko, D.S. Lemmen, Climate Risks & Adaptation Practices for the Canadian Transportation Sector 2016, Government of Canada, Ottawa, 2016.

[2]   Canadian Environmental Sustainability Indicators: Greenhouse Gas Emissions.

Consulted, Environment and Climate Change Canada, Ottawa, 2017.

[3]   J.Y. Yong, V.K. Ramachandaramurthy, K.M. Tan, N. Mithulananthan, A review on the state-of-the-art technologies of electric vehicle, its impacts and prospects, Renew. Sustain. Energy Rev. 49 (2015) 365–385. doi:10.1016/j.rser.2015.04.130.

[4]   L. Lu, X. Han, J. Li, J. Hua, M. Ouyang, A review on the key issues for lithium-ion battery management in electric vehicles, J. Power Sources. 226 (2013) 272–288. doi:10.1016/j.jpowsour.2012.10.060.

[5]   M. Khan, M. Swierczynski, S. Kær, Towards an Ultimate Battery Thermal Management System: A Review, Batteries. 3 (2017) 9. doi:10.3390/batteries3010009.

[6]   T.M. Bandhauer, S. Garimella, T.F. Fuller, A Critical Review of Thermal Issues in Lithium-Ion Batteries, J. Electrochem. Soc. 158 (2011) R1. doi:10.1149/1.3515880.

[7]   N. Omar, M.A. Monem, Y. Firouz, J. Salminen, J. Smekens, O. Hegazy, H. Gaulous, G. Mulder, P. Van den Bossche, T. Coosemans, J. Van Mierlo, Lithium iron phosphate based battery - Assessment of the aging parameters and development of cycle life model, Appl. Energy. 113 (2014) 1575–1585. doi:10.1016/j.apenergy.2013.09.003.

[8]   A. Barré, B. Deguilhem, S. Grolleau, M. Gérard, F. Suard, D. Riu, A review on lithium-ion battery ageing mechanisms and estimations for automotive applications, J. Power Sources. 241 (2013) 680–689. doi:10.1016/j.jpowsour.2013.05.040 Review.

[9]   A. Veeraragavan, A. Lenert, B. Yilbas, S. Al-Dini, E.N. Wang, Corrigendum to "Analytical Model for the Design of Volumetric Solar Flow Receivers" [Int. J. Heat Mass Transfer 55 (2012) 556–564], Int. J. Heat Mass Transf. 62 (2013) 578. doi:10.1016/j.ijheatmasstransfer.2013.03.010.

[10]   Z. Rao, S. Wang, M. Wu, Z. Lin, F. Li, Experimental investigation on thermal management of electric vehicle battery with heat pipe, Energy Convers. Manag. 65 (2013) 92–97. doi:10.1016/j.enconman.2012.08.014.

[11]   J. Jaguemont, L. Boulon, Y. Dub, A comprehensive review of lithium-ion batteries used in hybrid and electric vehicles at cold temperatures, Appl. Energy. 164 (2016) 99–114. doi:10.1016/j.apenergy.2015.11.034.

[12]   T.M. Bandhauer, S. Garimella, T.F. Fuller, A Critical Review of Thermal Issues in Lithium-Ion Batteries, J. Electrochem. Soc. 158 (2011) R1.

doi:10.1149/1.3515880.

[13]   M. Zolot, A. a. Pesaran, M. Mihalic, Thermal Evaluation of Toyota Prius Battery Pack, (2002). doi:10.4271/2002-01-1962.

[14]   Q. Wang, B. Jiang, B. Li, Y. Yan, A critical review of thermal management models and solutions of lithium-ion batteries for the development of pure electric vehicles, Renew. Sustain. Energy Rev. 64 (2016) 106–128. doi:10.1016/j.rser.2016.05.033.

[15]   Z. Ling, Z. Zhang, G. Shi, X. Fang, L. Wang, X. Gao, Y. Fang, T. Xu, S. Wang, X. Liu, Review on thermal management systems using phase change materials for electronic components, Li-ion batteries and photovoltaic modules, Renew. Sustain. Energy Rev. 31 (2014) 427–438. doi:10.1016/j.rser.2013.12.017.

Chapter 2 NUMERICAL INVESTIGATION of ACTIVE and PASSIVE COOLING SYSTEMS of a LITHIUM-ION BATTERY MODULE for ELECTRIC VEHICLES

2.1. Introduction

Electric and hybrid electric vehicles (EV and HEV) are considered as the best near-term solution to reduce the emissions of greenhouse gases in the transportation sector. Rechargeable lithium-ion (Li-ion) batteries have high specific energy and energy density relative to other cell chemistries which makes them well-suited for electrification of vehicles. The main barriers to the use of Li-ion batteries in electrical/hybrid vehicles are safety, cost related to cycle and calendar life, and low temperature performance [1]. These challenges are strongly coupled to the thermal effects and non-uniform temperature distribution in the battery. Furthermore, in case of overcharging, a lithium-ion battery may experience thermal runaway and explode due to the decomposition of battery components that generate flammable gaseous species. In addition, heating the battery outside a specific range can accelerate the battery aging and sever capacity fading. Therefore, the goal of battery thermal management system (BTMS) is to increase the lifetime of Li-ion cells by moderating the operating temperature of the cell. A modest and uniform temperature across each cell and across cell modules and pack helps to limit battery aging. It has been shown that large temperature gradients over a single cell reduce its lifetime [2]. Premature aging of a single cell decreases the performance of a module remarkably because when the batteries are connected in series, the weakest cell will influence the maximum capacity of the system.

Different BTMS has been used for battery packs with different heat generation rates, and in general, the approaches utilized by BTMS embrace active cooling (air and liquid cooling) and passive cooling.

Since the specific heat capacity of air is much lower than many other cooling fluids, air cooling is usually unable to control the battery temperature within an optimal range, especially in the case of large size battery packs and high discharging rates [3]. Pesaran et al. [4] showed liquid based thermal management could achieve better performance than air cooling for EVs and series HEVs. Liquid cooling BTMS has been investigated in many studies [5-10]. Karimi and Dehghan [5] compared the performance of two working fluids, silicon oil and air, in the flow network cooling circulations for Li-ion battery pack. They showed that the use of silicon oil could reduce the maximum temperature and Z-shape flow network is more efficient than the U-shape one. Cold plates have recently emerged as a useful approach for active liquid cooling systems because of its compactness and ability to separate fluid and battery, which improves the safety of battery system [7-10]. The cold plate cooling method relies on the circulation of liquid inside the mini-channels that closely arranged in the plate. Jin et al. [7] reported that with

the fluid cooled in the condenser, the cold plate can continuously absorb the heat generated from the battery pack. A three dimensional thermal model was developed by Huo et al. [8] to examine the performance of the cold plate with straight channels and with water as the medium. By adjusting the number of channels, the flow rate, and the flow directions inside the channels, the optimal parameter values were specified. The effect from the geometry of the channels was also stressed in another study by looking at the temperature uniformity, mean temperature, and pressure drop resulted from different serpentine channel designs. Smith et al. [11] presented a simulative method to predict the optimal cooling circuit operating conditions (coolant volumetric flow rate and inlet temperature) of the clod plate BTMS system. They used 2D and 3D models in order to minimize the pressure loss across the BTMS, the temperature gradients over and amongst the cells, and the maximum cells temperatures. Their results indicated that the maximum temperature could be controlled only at the expense of relatively large temperature difference over the battery module.

The PCM cooling for BTMS was first introduced by Al-Hallaj and Selman [12] in which the PCM used was the mixture of pentacosane and hexacosane. They showed that PCM cooling systems benefit from many advantages such as high compactness, low cost, no need for circulatory network, desired cooling effect, better performance in case of thermal run away and more uniform temperature distribution. Despite this there are some drawbacks in this method such as volume and weight increase of battery system, and unfavorable thermal inertia. Javani et al. [13, 14] predicted the performance of n-octadecane based PCM BTMS using two types of surrounding layouts for Li-ion batteries. By varying the input parameters, the minimum amount of PCM to obtain a desirable maximum temperature was determined. Ramandi [15] developed a hybrid PCM system using four kinds of phase change materials in their simulation. In the conditions of combining caprice acid with either one of the other three materials, the capacities of the double shell PCM cooling system were compared with the single shell one. The results indicated that the double shell design had higher exergy efficiency than the single shell system in most cases. Application of carbon fiber filler added PCM was introduced by Babapoor et al. [16]. They utilized four kinds of carbon fibers with the average lengths and then the cooling capability of these PCM composites was examined. They showed that PCM with 2 mm long carbon fiber at a mass fraction of 0.46% could give batteries the smallest temperature gradient throughout discharge. Expanded graphite matrix (EG) for battery cooling was first reported by Mills et al. [17], who stated the production method of expanded graphite in this paper. One advantage of this type of cooling composite was that the liquid state PCM could be well stored inside the matrix with strong capillary force, thus avoiding the leaking problem. Afterwards, the PCM/EG cooling matrix was experimentally and numerically studied in many works [18-21]. Kizilel et al. [22] simulated the performance of the composite cooling matrix at extreme condition when one cell in battery pack underwent thermal runaway. It was proved that

the composite matrix was capable of rapidly conducting the heat away before the surrounding cells being heated to the threshold temperature of the same danger. The PCM/copper foam cooling matrix has been examined by Li [23]. Copper foams with different porosities and pore densities were used in their work. A low porosity was recommended due to the preferable heat conduction, which enhances the temperature distribution uniformity and controls maximum temperature of the battery pack.

In all of the above mentioned numerical studies, battery heat generation is estimated based on simplified models. [3-6, 9-11, 12-14, 16, 18, 19] used uniform heat generation model in their studies. Although uniform heat generation can significantly simplify the numerical model, it leads to underestimated temperature non-uniformity prediction over the cell and module scale. In order to solve this drawback, Jarret and Kim [24] used four simplified linear heat generation distributions with a constant total heat generation. This method can improve the accuracy of temperature gradient estimation, however the temperature distribution in Li-ion batteries is not necessarily linear and the heat generation is not constant during a charge and/or discharge cycle.

Understanding of heat generation in Li-batteries is crucial for realistic estimate of effects of thermal management system on the performance of battery module. In the present study, a pseudo three-dimensional thermal-electrochemical model was developed for a commercial prismatic LiMon2O4/graphite battery by coupling mass, charge, and energy conservations, and electrochemical kinetics. The model solves the local cell unit as 1D and the current conservation equation as 3D in the battery. The numerous 1D local electrochemical cell units were connected in parallel to calculate the reaction heat generation per unit volume of the battery while the Ohmic heat generation is found by solving 3D current conservation equation. Finally, the 3D heat conduction governing equation is solved to find the temperature distribution of battery. Then, this model was used to compare the effects of liquid and PCM cooling systems on the temperature distribution over the cell and module scale.

Nomenclature

c_s	concentration of lithium in the active material particles (mol m-3)
c_l	electrolyte concentration (mol m-3)
D_s	diffusion coefficient of lithium in the active material (m2 s-1)
D_l	diffusion coefficient of electrolyte (m2 s-1)
E_{aD}	diffusion activation energy (kJ mol-1)
E_{aR}	reaction activation energy (kJ mol-1)
$f_\pm$	average molar activity coefficient
F	Faraday's constant (C mol-1)
h	convective heat transfer coefficient (W m-2 K-1)
i	local working current density of the cell unit (A m-2)

j_0	exchange current density (A m-2)
j_n	local charge transfer current density (A m-2)
k_0	reaction rate constant (m2.5 mol-0.5 s-1)
k	thermal conductivity (W m-1 K-1)
L	thickness of each battery component (m)
Q_{rea}	reaction volumetric heat generation (W m-3)
Q_{pol}	polarization volumetric heat generation (W m-3)
Q_{Ohm}	Ohmic volumetric heat generation (W m-3)
R	gas constant, 8.314 (J mol-2 K-1)
r	radius distance variable of electrode particles (m)
r_0	radius of electrode particles (m)
S_a	specific surface area (m-1)
t	time (s)
t_+	transferring number of Li$^+$
T	temperature (K)
T_a	ambient temperature (K)
U_{eq}	open circuit potential of the electrode (V)
$U_{eq,ref}$	open circuit potential under the reference temperature (V)
Greek letters	
α_a	anode transfer coefficient
α_c	cathode transfer coefficient
ε	emissivity of the battery surface
ε_s	active material volume fraction
ε_l	electrolyte volume fraction
Φ_s	solid phase potential
Φ_l	electrolyte phase potential
γ	Bruggeman tortuosity exponent
σ_s	electronic conductivity in solid phase material (S m-1)
σ_l	ionic conductivity of electrolyte (S m-1)
η	local surface overpotential (V)
Subscripts and superscripts	
0	initial or equilibrated value
s	solid phase
l	electrolyte phase
eff	effective value

2.2 Numerical Model

2.2.1. Coupled electrochemical-thermal model

A pseudo 3D electrochemical-thermal model for a single cell in a prismatic $LiMn_2O_4$/graphite battery was developed. The nominal voltage and capacity of the cell under study are 3.2 V and 16.5 Ah, respectively. Figure 2-1 shows schematic of 1D and 3D model structures of the pseudo 3D single cell.

The current within the cell unit travels mainly in the through plane direction (as shown in Figure1) perpendicular to the sandwich structure, and the current parallel to the sandwich structure is negligible. Therefore, each local cell unit, including negative electrode, separator, and positive electrode, is considered as 1D to simulate the electrochemical reactions. The 1D local cell units are connected in parallel by current. In this model, the electrodes are the porous solid matrix that consists of active particles with spherical shapes of uniform sizes and additives. The positive electrode contains active material particles of $LiMn_2O_4$ and the negative electrode contains the active material particles of graphite (LiC_6) and the separator is a porous polymer membrane which creates a barrier between the two electrodes. The electrodes and separator are impregnated with $LiPF_6$/EC/DEC electrolyte, ensuring the transfer of lithium ions between the two electrodes.
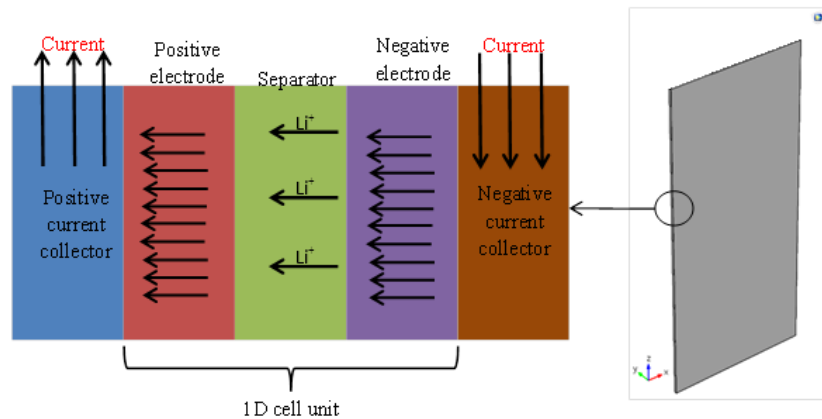
Figure 2-1 Schematic of overall model structure. The current enters and leaves the battery through the current collector tabs at specific surfaces on the battery

Table 2-1. Governing equations used in different solvers

Governing Equation	1D solver	3D Solver
Electrochemical kinetics	x	
Charge conservation	x	x
Mass conservation	x	
Heat Conduction		x
Reaction heat generation	x	
Ohmic heat generation		x

The electrochemical reactions that occur at the interface of the electrode and electrolyte during discharge are:

Negative Electrode: $LiC_6 \rightarrow xLi^+ + Lil_{-x}C^6 + e^-$

Positive Electrode: $xLi^+ + xe^- + LiMn_2O_4 \rightarrow Lil_{-x}Mn_2O_4$
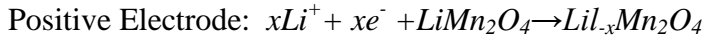
2.2.2. Electrochemical kinetics at the interface
The local charge transfer current density is determined by Butlere-Volmer equation is given below:

$$j_n = j_0 \left\{ \exp(\frac{\alpha_0 F}{RT} \eta) - \exp(\frac{\alpha_c F}{RT} \eta) \right\} \tag{2.1}$$

where j_0 is the exchange current density, α_0 and α_c are the anodic and cathodic charge transfer coefficients, h is the local surface overpotential, and F is the Faraday constant.

2.2.3. Charge conservation
The governing equation for charge conservation in the positive/negative electrodes is expressed as:

$$\nabla. i_1 + \nabla. i_2 = 0 \tag{2.2}$$
$$\nabla. i_1 = -S_a j_n \tag{2.3}$$

$$\nabla. i_2 = -S_a j_n \tag{2.4}$$

where i_1 refers to the electrical current density in the solid phase, i_2 is the ionic current density in the electrolyte phase, and S_a is the specific surface area.

2.2.4. Electron transport in the solid phase
The transport of electrons in the solid phase follows Ohm's law given by:

$$i_1 = \sigma_1^{eff} \nabla \Phi_1 \tag{2.5}$$

where σ_1^{eff} is the effective electrical conductivity of the solid phase.

2.2.5. Mass conservation

The mass conservation of lithium in the spherical active material particle is described as following:

$$\frac{\partial C_1}{\partial t} + \frac{1}{r^2}\frac{\partial}{\partial t}\left(-r^2 D_1 \frac{\partial C_1}{\partial r}\right) = 0 \tag{2.6}$$

where C_1 is the concentration of lithium in the active material particles of the electrode, t is the time, D_1 represents the diffusion coefficient of lithium in the solid phase, and r is the radial coordinate inside a spherical particle. It is assumed that r cannot exceed the particle's radius.

The mass conservation of lithium ions in the electrolyte is given by:

$$\varepsilon_2 \frac{\partial C_2}{\partial t} + \nabla . J_2 = \frac{S_a j_n}{F} \tag{2.7}$$

where:

$$J_2 = -D_2^{eff} \nabla . C_2 + \frac{i_2 . t_+}{F} \tag{2.8}$$

where J_2 is the molar flux of lithium ions that consists of two terms: the first term following Fick's law and the second accounting for electro-migration, D_2^{eff} shows the effective diffusion coefficient of lithium ions in the electrolyte, and ε_2 is the volume fraction of the electrolyte phase. Table 2-2 shows the values of parameters used in the governing equations.

2.2.6. Energy Equation

The energy balance in the lithium ion battery is given in Eq. (1), in which there are two sources of heat generation:

$$C_p \frac{\partial T}{\partial t} - k\nabla^2 T = Q_{reaction} + Q_{Ohmic} \tag{2.9}$$

where:

$$Q_{reaction} = S_a j_n T \frac{\partial U_{eq}}{\partial T} + S_a j_n \eta \tag{2.10}$$

$$Q_{Ohmic} = -i_l . \nabla \Phi_l - i_s . \nabla \Phi_s \tag{2.11}$$

As shown in Table 2-1, the charge conservation equations in the active battery material and current collectors are solved in 1D and 3D models, respectively.

Table 2-2. Parameters used in the pseudo 3D model

Parameter	Value[unit]
Solid phase Li-diffusivity Negative	$3.9e\text{-}14[m^2/s]$
Solid phase Li-diffusivity Positive	$1e\text{-}13[m^2/s]$
Particle radius Negative	$12.5[\mu m]$
Particle radius Positive	$8[\mu m]$
Solid phase volume fraction Positive	0.259
Electrolyte phase volume fraction Positive	0.444
Solid phase volume fraction Negative	0.172
Electrolyte phase volume fraction Negative	0.357
Max solid phase concentration Negative	$26390[mol/m^3]$
Max solid phase concentration Positive	$22860[mol/m^3]$
Reaction rate coefficient Negative	$2e^{-11}[m/s]$
Reaction rate coefficient Positive	$2e\text{-}11[m/s]$
Initial Negative State of Charge	7917
Initial Positive State of Charge	16002
Initial electrolyte salt concentration	$2000[mol/m^3]$
Length of negative electrode	$55[\mu m]$
Length of separator	$30[\mu m]$
Length of positive electrode	$55[\mu m]$
Thickness of battery canister	$0.25[mm]$
Battery width	$70[mm]$
Battery height	$116[mm]$
Battery thickness	$27[mm]$
Negative current collector thickness	$7[\mu m]$
Positive current collector thickness	$10[\mu m]$

In Eq. (2.1) ρ, C_p and k are the local density, heat capacity and thermal conductivity of the cell medium, T is the temperature, t is the time and Q is the heat generated.

2.2.7. Boundary Conditions

At the electrode/separator interface, as shown in figure 1, insulation is specified for the electrical current of the solid phase. Continuity is used for the ionic current, lithium ion flux of electrolyte phase and heat flux:

$$n.i_1 = 0, n.i_2|_{I+} = n.i_2|_{I-}, n.J_2|_{I+} = n.J_2|_{I-}, n.q|_{I+} = n.q|_{I-} \qquad (2.12)$$

2.3. Liquid Cooling System

A commonly implemented building block in the design of a battery system is a module. The module must be coupled to the BTMS to optimize the thermal contact but not to jeopardize the electrical insulation between cells (if the cooling plate is electrically conductive). Figure 2-2 shows the layout of a battery module for prismatic cells. In the module, eight 16.5 Ah LiMon2O4/graphite battery cells (116mm×70mm×27mm) are arranged in series electrically with their terminal tabs located on the top side of module. The cells in the module are cooled via a cooling plate with the height H=2mm. The cells are thermally coupled to the cooling plate via a commercially available, 0.5 mm thick ductile interface with high thermal conductivity. The channel hydraulic diameter is considered as the characteristic length and based on this characteristic length and the fluid inlet velocity the flow is in the laminar region (Reynolds Number<2100) for all cases.
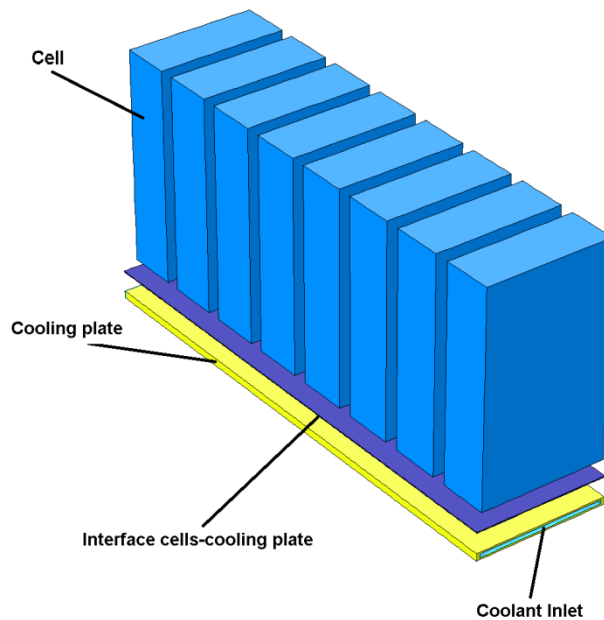
Figure 2-2. Schematic of the liquid cooling system

The density, specific heat capacity, and thermal conductivity of the cooling fluid are assumed constant. However, viscosity varies significantly and is therefore described as a polynomial function in COMSOL Multiphysics software. Pressure outlet and velocity inlet boundary conditions are applied. The contact thermal resistance between the cells and the ductile mate as well as between the ductile mate and the cooling channel are

neglected. All external walls are assumed adiabatic. The transient solution is calculated with the COMSOL v5.1 from an initial module temperature of 293 K.

The thermal effect of coolant flow rate on the maximum temperature (T_{max}) and maximum temperature difference over the module (T_{max}-T_{min}) are investigated using the coupled thermal-electrochemical model. The model solves the thermal behavior of the module for three C-rates (1C, 3C, 5C) to evaluate these parameters for different coolant operating conditions.

In the both liquid and PCM cooling scenarios, the heat transfer from batteries to surroundings is neglected. Using insolation boundary condition creates a framework to compare the effects of different cooling systems on the thermal performance of battery module.

2.4. PCM Cooling System
Thermal management for battery systems can be achieved without excessive complexity of liquid cooling apparatus by using a PCM cooling system. Figure 2-3 shows the schematic of this system. In this design each cell is bounded by two relatively thin layer of PCM, and therefore, for a module with n cell, n+1 layers of PCM are used.
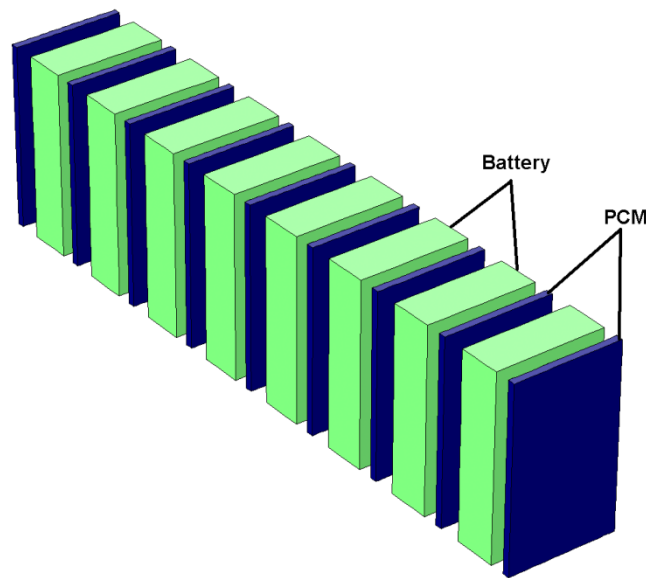
Figure 2-3. Schematic of the PCM cooling system

Due to its large latent heat of fusion, the PCM integrated into the module will act as a heat sink for the heat generated during the charge of a Li-ion battery. The heat stored in

PCM will be rejected later when the battery temperature drops during the charging cycle, which is much less exothermic compared to the discharging process, or by natural convection to the surroundings.

The most important parameters for selecting a PCM are the melting temperature and latent heat. The ideal PCM candidate for Li-ion battery thermal management will have a melting temperature between 45 to 65°C, high latent heat per unit volume, and a narrow melting temperature range. Furthermore, the material should be chemically stable, safe, non-corrosive with respect to other battery components, nontoxic, cheap, and light.

Since phase change is involved in this cooling system, the energy equation must be written separately for the solid and liquid phases. One difficulty of using such an approach is how to track the moving interface. The effective heat capacity method may be used to simplify the two-phase energy equation. This method applies a single energy equation in both phases; hence, there is no need to consider liquid and solid phases separately. In the method, the PCM was assumed to melt and solidify within a temperature range of 2–4°C, which represents the true situation of most commercial grade Paraffins. The essence of effective heat capacity method is to take into account the latent heat, in the phase-change region, by using an effective heat capacity (C_{p_e}). The values of C_{p_e} change from a small value of the solid to a maximum value at the melting temperature range. Any function may be selected such that:

$$\int_{T_{m1}}^{T_{m2}} Cp_e \, dT = \lambda \tag{2.13}$$

where λ is the latent heat of fusion of PCM.

Farid et al. [27] proposed the following equations to describe the effective heat capacity in the two-phase region:

$$Cp_e = a + b(T - T_{m1}) \quad T_{m1} < T < T_{m2} \tag{2.14}$$

where

$a = \frac{Cp_m - Cp_s}{T_m - T_{m1}}, \; b = \frac{Cp_m - Cp_l}{T_{m2} - T_m}, \; Cp_m = \frac{2\lambda}{(T_{m2} - T_{m1})} + Cp_s$

T_{m1}=Beginning of melting temperature

T_m=Melting temperature

T_{m2}=End of melting temperature

where $T_{m1} < T < T_{m2}$ represents the melting temperature range.

The model used in this study accounts for the change in thermal property values of the PCM by assigning different values for the solid, mushy, and liquid phases, using the effective heat capacity method. It should be mentioned that natural convection during melting of the PCM may have a role on the heat transfer inside the battery module. All contact resistances are neglected and external walls are assumed adiabatic. For simplification, we did not account for it in the present model; however, in future work the effect of natural convection should be included. Table 2-3 shows the physical properties of the paraffin wax (SUNTECH P116) used in the simulations [27].

Table 2-3. Thermophysical properties of the PCM used in simulations

Parameter	Value
Cp_s (kJ kg^{-1} K^{-1})	1.77
Cp_l (kJ kg^{-1} K^{-1})	1.77
k_s (W m^{-1} K^{-1})	0.29
k_l (W m^{-1} K^{-1})	0.21
ρ_s (kg m^{-3})	910
ρ_l (kg m^{-3})	822
λ (kJ/kg)	224.36

2.5. Results

2.5.1. Battery thermal behavior
A pseudo 3D coupled thermal-electrochemical model has been developed for a $LiMn_2O_4$ prismatic battery. The current collecting tabs on the battery have been considered as the upper surface of current collectors. The reaction heat generation is obtained from the 1D cell unit model and is assumed to be uniform over the active battery material (porous electrodes and the separator). The 3D single cell model solves the current conservation equation and corresponding Ohmic heat generation over the whole cell unit (active material and current collectors). Figure 2-4 shows the temperature distribution of the single cell under various discharge rates at DOD=40%.

The maximum temperature difference, between the hottest and the coldest spots, during 1C, 3C and 5C discharge are 0.8K, 2.6K, and 5.7K, respectively. The charge and discharge current of a battery is measured in C-rate. A discharge of 1C draws a current equal to the rated capacity, and 3C-rate discharge draws a current equal to three times of rated capacity. The temperature is higher in the region close to the upper surface of current collectors. The reason is that the current converges at these regions, thus the

Ohmic heat generation, and consequently, higher temperature is observed close to current terminals.

In the next sections, the pseudo 3D model developed will be used to investigate the effects of different thermal management systems on the maximum temperature and temperature distribution under different working conditions.
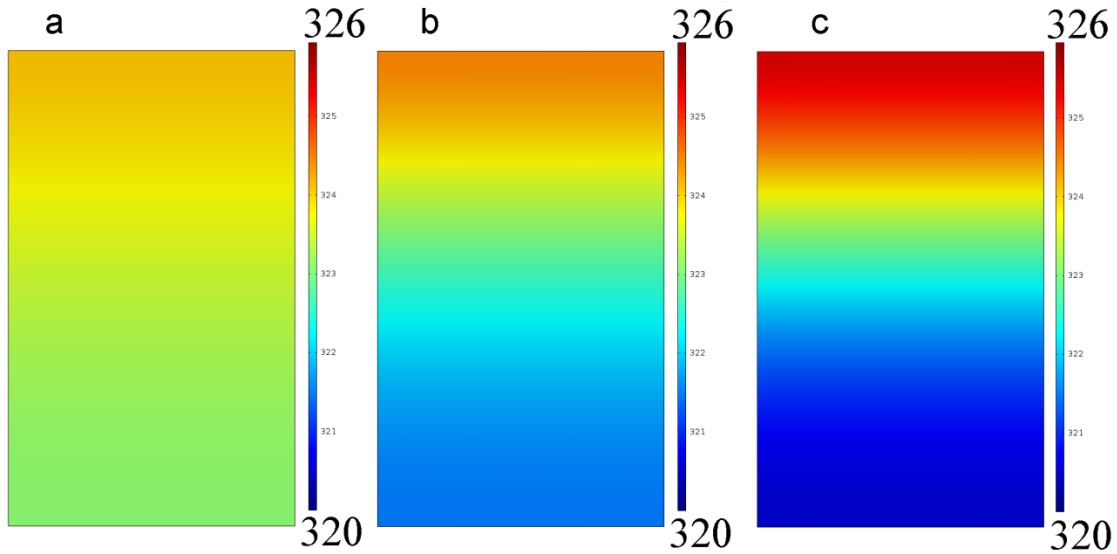
Figure 2-4. Single cell temperature distribution at DOD=80% under 1)1C, b)3C and c)5C discharge rate

2.5.2. Cooling plate

Battery module temperature distribution was modeled at 1C, 3C and 5C discharge rates. Figure 2-5 shows the temperature distribution of initially fully charged battery module at the end of discharge process (DOD=80%).
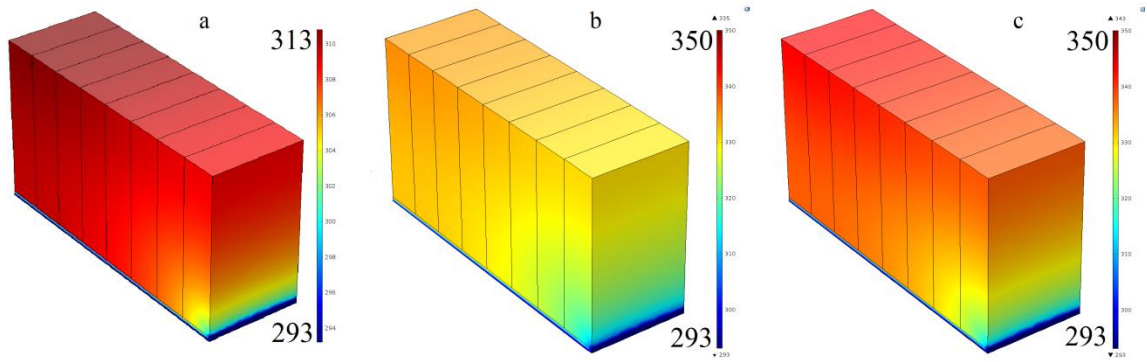
Figure 2-5. Module temperature distribution with liquid cooling system at DOD=80% at a)1C, b)3C, c)5C discharge rate.

As can be seen from Figure 2-5, the temperature non-uniformity increases with the C-rate. This is mainly because of the higher battery heat generation at bigger C-rates. The maximum temperature occurs at the left top corner of the module which has the biggest distance from the coolant entrance.

In order to examine the effects of coolant operating condition on the module temperature distribution three coolant inlet velocities were used. The coolant enters at 293K and three different velocities i. e. 0.5m/s, 1m/s and 2m/s. As Figure 2-6 depicts, the inlet velocity has minor effect on the variation of module average temperature with time. Due to the low thermal conductivity of batteries a weak thermal contact exists between the battery high temperature regions and the cooling plate, and therefore, an increase in convective heat transfer coefficient inside the plate will not affect the temperature considerably.
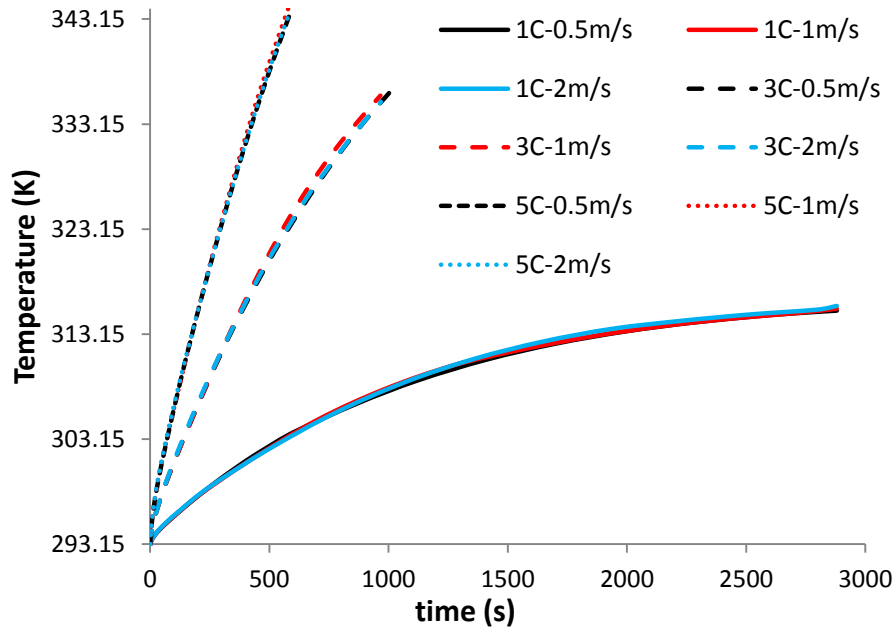
Figure 2-6. Effect of coolant inlet velocity on the batteries maximum temperature

Better heat distribution can be achieved by using thin Aluminum fins attached to the cooling plate or by re-arranging the batteries to increase the effective heat transfer area between the cells and the cooling plate.

Three cooling system with different thickness of PCM layer were considered. In the first layout the PCM layer thickness is half of that of batteries. Figure 2-7 shows the module temperature distribution at the end of discharge process and for different C-rates. The maximum temperature in the module is 316.2K, 316.4K and 317.3K at 1C, 3C and 5C discharge rates, which are 5K higher, and 20K and 26K lower than the cooling plate system, respectively. Unlike the cooling plate design the maximum battery temperature in PCM system occurs at the middle of the module were the natural convection cooling effects to the surroundings are minimal.
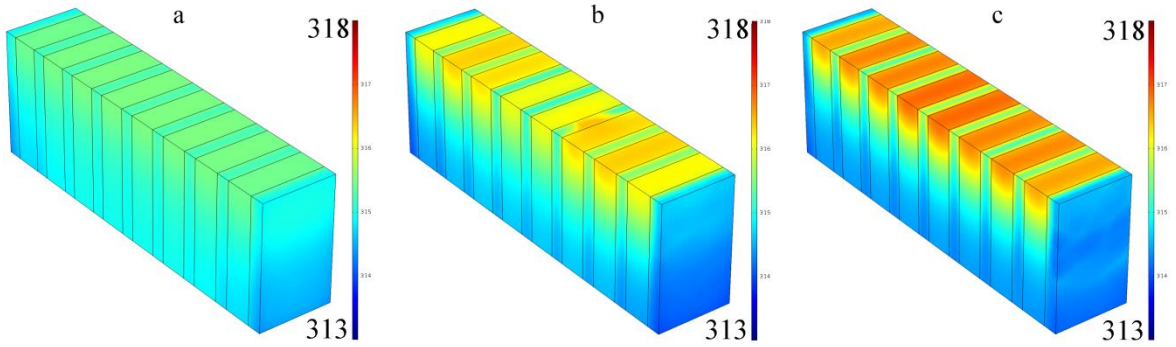
Figure 2-7. Module temperature distribution with PCM cooling system at DOD=80% at a)1C, b)3C, c)5C discharge rate

Figure 2-8 depicts the variation of the batteries maximum temperature for both liquid and PCM cooling systems. Both systems show the same trend   for   the   1C   discharge   rate however, at higher C-rates the PCM shows advantage over the liquid system.
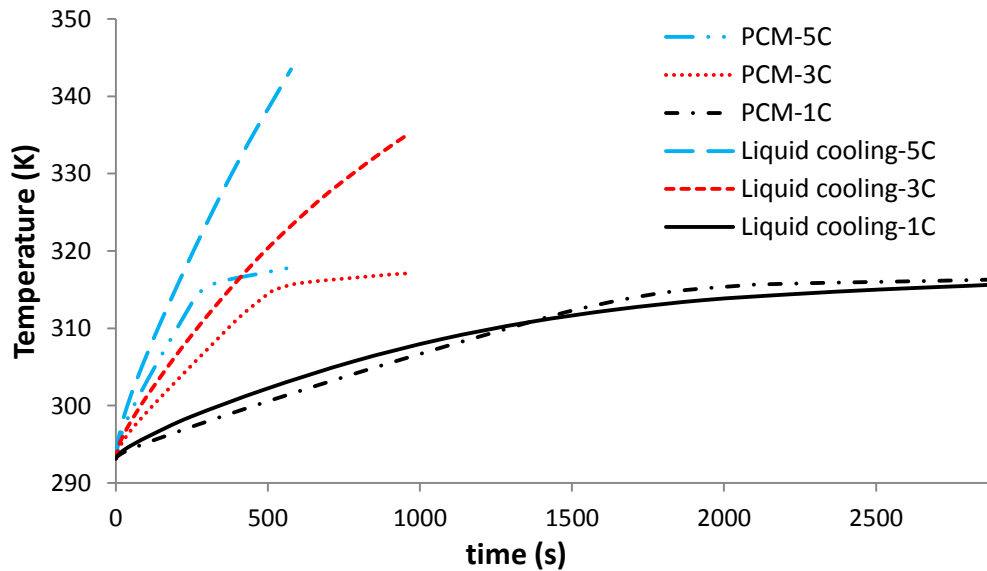
Figure 2-8. Variation of the batteries maximum temperature for both liquid and PCM cooling systems

At temperatures lower than PCM melting point, the PCM system temperature rise is slightly lower than that of liquid cooling system due to the thermal inertia added by the sensible heat of PCM and also more effective heat transfer surface on the sides of the cells. As the maximum temperature approaches the melting point of PCM (317K), the

excess heat is stored as the latent heat at constant temperature. Therefore, most of the heat rejected from the cell during discharge was stored as latent heat in the PCM by changing its phase from solid to liquid. This stored heat will be released by natural convection after the end of discharge during the time when the cell is left to relax.
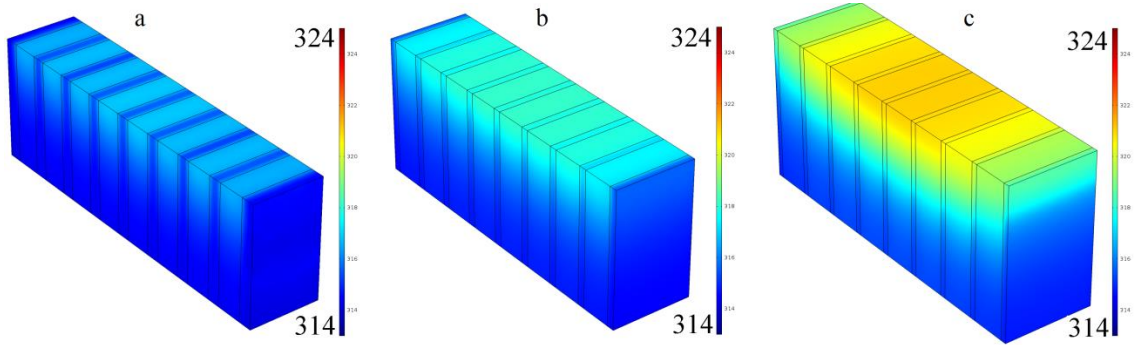
Figure 2-9. Module temperature distribution with PCM cooling system at DOD=80% with PCM thickness equals a) half of battery thickness, b) one fourth of battery thickness, and c) one sixth of battery thickness.
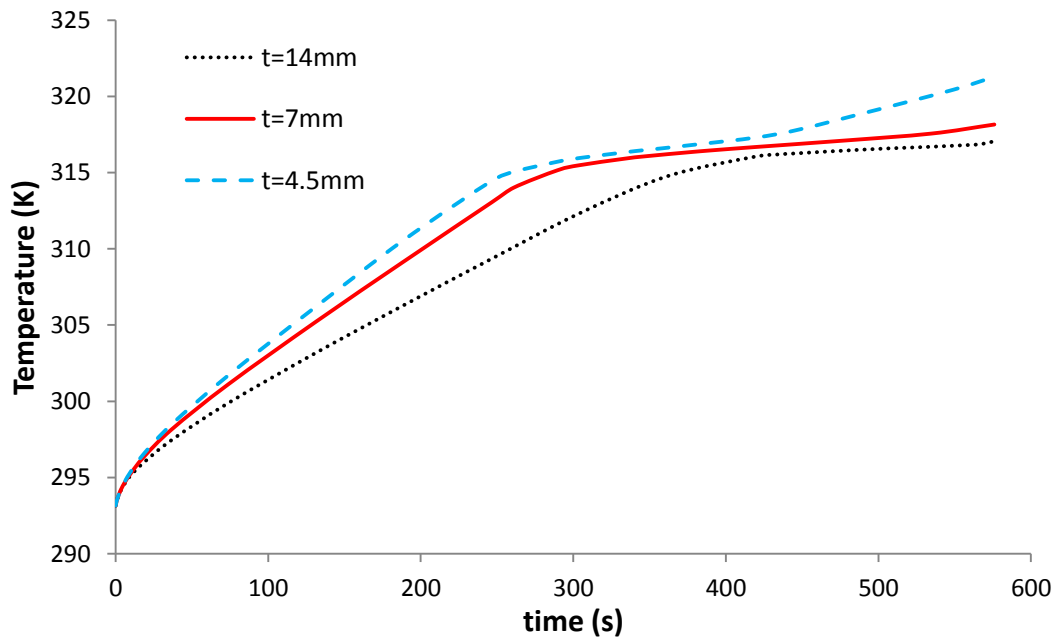
Figure 2-10. Effect of PCM layer thickness on the batteries maximum temperature

It is noteworthy to mention that in Figure 7c the temperature in the half bottom region of module is less than the melting point while the upper region is in liquid phase. This is because of the very low PCM thermal conductivity which acts as a thermal barrier between cells. Increasing the thermal conductivity of PCM will enhance the heat transfer inside the module that leads to more uniform temperature distribution and higher amount of heat stored in the PCM per unit volume. Another approach to tackle this problem is to lower the thickness of PCM which can increase the heat conduction between two adjacent cells.

Figures 2-9 and 2-10 show the module temperature distribution and the battery maximum temperature at the end of 5C discharge for three different PCM thicknesses. The desired temperature can be achieved when the PCM layer thickness is one fourth of cell thickness. This shows that there is an optimal value for the thickness of PCM layer for this module design.

2.6. Conclusion

A pseudo 3D thermal-electrochemical coupled model has been developed for a 16.5Ah LiMn2O4 prismatic battery. The model treated the reaction heat generation with many 1D local cell units and Ohmic heat generation by a 3D model. The model presented the non-uniform distribution of the heat generation rate of the cell during discharge process. Using this model, two thermal management systems that incorporate liquid cooling, and a phase-change material (PCM) was presented and investigated. Simulation results for the module using the PCM showed that the temperature rise of the module was significantly lower than that for the same cell under the liquid cooling conditions. Furthermore, using PCM increased the temperature uniformity which results in longer cycle life the batteries. Another advantage of the PCM thermal management system is that the heat stored as latent heat in the PCM is transferred to the cell module during relaxation and keeps it at a temperature above the surrounding temperature for a long time that increases the overall energy efficiency of the battery system. Future research will explore heat generation of batteries during charging process to simulate the battery heat generation under real driving cycles.

References
[1] T. M. Bandhauer, S. Garimella and T. F. Fuller, A Critical Review of Thermal Issues in Lithium-Ion Batteries, J. Electrochem. Soc. 158 (2012) 1–25.

[2] A. A. Pesaran, M. Keyser, Santhanagopalan S., Large Lithium Ion Battery Technology & Application, presented at Advanced Automotive Battery Conference, USA, 2013.

[3] S. Al-Hallaj, J.R. Selman, Thermal modeling of secondary lithium batteries for electric vehicle/hybrid electric vehicle applications, J. Power Sources 110 (2002) 341-348.

[4] A.A. Pesaran, Battery Thermal Management in EVs and HEVs: Issues and Solutions, presented at Advanced Automotive Battery Conference, USA, 2001.

[5] G. Karimi, A. R. Dehghan, Thermal Management Analysis of a Lithium-Ion Battery Pack using Flow Network Approach, Int. J. Mech. Eng. (2012) 88-94.

[6] T. Zhang, Status and development of electric vehicle integrated thermal management from BTM to HVAC, Appl. Therm. Eng. (2015) 552-529.

[7] L.W. Jin, P.S. Lee, "Ultra-thin mini-channel LCP for EV battery thermal management", Appl. Energy 113 (2014) 1786-1794.

[8] Y. Huo, Z. Rao, X. Liu, J. Zhao, Investigation of power battery thermal management by using mini-channel cold plate, Energy Conv. . Manage. 89 (2015) 387-395.

[9] A. Jarrett, Y. Kim, Design optimization of electric vehicle battery cooling plates for thermal performance, J. Power Sources, 196 (2012)10359-10368.

[10] W. Tong, K. Somasundaram, Numerical investigation of water cooling for a lithium-ion bipolar battery pack, International Journal of Thermal Sciences, 94 (2015) 259-269.

[11] J. Smith, Simulative method for determining the optimal operating conditions for a cooling plate for lithium-ion battery cell modules, Journal of Power Sources (2014) 784-792.

[12] S. Hallaj, J. Selman, A Novel Thermal Management System for Electric Vehicle Batteries Using Phase Change Material, J. Electrochem. Soc. 147 (2000) 3231-3236.

[13] N. Javani, I. Dincer, B.S., Heat transfer and thermal management with PCMs in a Li-ion battery cell for electric vehicles, Int. J. Heat Mass Transfer 72 (2014) 690-703.

[14] N. Javani, Modeling of passive thermal management for electric vehicle battery packs with PCM between cells, App. Therm. Eng. 73 (2014) 307-316.

[15] M. Y. Ramandi, I. Dincer, Heat transfer and thermal management of electric vehicle batteries with phase change materials, Heat Mass Trans. 47 (2011) 777-788.

[16] A. Babapoor, M. Azizi, G. Karimi, Thermal management of a Li-ion battery using carbon fiber-PCM composites, App. Therm. Eng. 82 (2015) 281-290.

[17] A. Mills, M. Farid, J. R. Selman, S. Al-Hallaj, Thermal conductivity enhancement of phase change materials using a graphite matrix, App. Therm. Eng. 26 (2006) 1652-1661.

[18] A. Greco, An investigation of lithium-ion battery thermal management using paraffin/porous-graphite-matrix composite, J. Power Sources 278 (2015) 50-68.

[19] C. Lin, J. Liu, Experiment and simulation of a LiFePO4 battery pack with a passive thermal management system using composite phase change material and graphite sheets, J. Power Sources 275 (2015) 742-749.

[20] Schweitzer B., Wilke S., Khateeb S., Al-Hallaj S., Experimental validation of a 0-D numerical model for phase change thermal management systems in lithium-ion batteries, Journal of Power Sources, 287 (2015) 211-219.

[21] R. Kizilel, A. Lateef, Passive control of temperature excursion and uniformity in high-energy Li-ion battery packs at high current and ambient temperature, J. Power Sources 183 (2008) 370-375.

[22] Kizilel R., Sabbah R., J. Selman R., Al-Hallaj S., An alternative cooling system to enhance the safety of Li-ion battery packs, J. Power Sources 194 (2009) 1105-1112.

[23] W.Q. Li, Z.G. Qu, Experimental study of a passive thermal management system for high-powered lithium ion batteries using porous metal foam saturated with phase change materials, J. Power Sources 255 (2014) 9-15.

[24] A. Jarrett, Y. Kim, Influence of operating conditions on the optimum design of electric vehicle battery cooling plates, J. Power Sources 245 (2014) 644-655.

[25] M. Doyle, J. Newman, A.S. Gozdz, C.N. Schmutz, Tarascon J.M., Comparison of Modeling Predictions with Experimental Data from Plastic Lithium Ion Cells, J. Electrochem. Soc. 143 (1996) 1890–1903.

[26] S. Khateeb, Thermal management of Li-ion battery with phase change material for electric scooters: experimental validation, J. Power Sources 142 (2005) 345–353.

[27] M.M. Farid, F.A. Hamad, M. Abu-Arabi, Melting and solidification in multi-dimensional geometry and presence of more than one interface, Ener. Conv. Manage. 39 (1998) 809–818.

Chapter 3 A PSEDUO 3D ELECTROCHEMICAL-THERMAL MODELING and ANALYSIS of a LITHIUM-ION BATTERY for ELECTRIC VEHICLE THERMAL MANAGEMENT APPLICATIONS

3.1. Introduction

Lithium-ion (Li-ion) batteries are considered as suitable energy storage devices for the electrification of vehicles due to their high specific energy and power densities [1, 2], low self-discharge rate [3], and no memory effect [4]. The main barriers to the use of Li-ion batteries in electric vehicles (EV) are safety, cost related to cycle and calendar life, and low temperature performance [5]. These challenges are strongly coupled to the thermal behavior and non-uniform temperature distribution in the battery and may reduce its performance and lifetime [6,7] or lead to thermal runaway [8,9]. Hence, Li- ion batteries numerical simulation has become vital in developing a fundamental understanding of thermal characteristics of these batteries in order to improve battery thermal management systems (BTMS).

sSeveral 1D electrochemical models are reported in the literature based on the kinetics models to solve the electrochemical and/or thermal characteristics of a cell unit [10–12]. These models are commonly solved in the 1D thickness dimension of the electrodes, assuming that the electric potential is uniform in the plane of the current collectors. This assumption is applicable to small format batteries and can be used to estimate average values for large batteries. However, it does not consider the issue of non-uniform thermal and current distributions observed in large-format cells. Therefore, multi-dimensional models are desirable for batteries used in EV to understand the cell current and temperature distributions [13,14].

A number of multidimensional mathematical models, such as single particle models [15], equivalent circuit models [16,17], and 3D lumped thermal models [18–22], have been developed to estimate the charging and discharging profiles and heat generation within the lithium ion cells. The single particle model is a simplified method by assuming the uniform concentration gradient in the electrolyte. The equivalent circuit model, which is consist of a network of resistors and the voltage source, is utilized for electrochemical impedance characterization of Li-ion batteries. The three dimensional lumped thermal models treat the layer structure of the cell unit as homogeneous material with uniform electrical and thermal properties, heat generation and temperature distribution. The majority of three dimensional lumped thermal models do not take the electrochemical reactions into account. In these models, the heat generation due to the electrochemical reaction is simply added to the energy equation as a source term.

Different approaches have been reported in the literature in order to develop numerical 3D inhomogeneous thermal models. Some researchers [23–25] used basic principles of conservation of energy, established by Bernardi et. al. [26] to derive heat generation equations. These models are relatively timesaving, but ignore the detailed electrochemical process and assume heat generation is uniform within the cell. Coupled electrochemical-thermal modeling is an alternative approach to simulate the thermal behavior of Li-ion batteries [27,28]. The model is based on the porous electrode method combined with an energy conservation equation proposed by Pals and Newman [29,30].

Several 2D and 3D electrochemical-thermal numerical models have been developed to simulate the detailed charge and mass transfer processes occurring in the porous electrodes and electrolyte. However, coupled multi-dimensional simulations are highly nonlinear and computationally demanding. In order to reduce the numerical complexity and computational time, a few pseudo 3D models have recently been developed. Lai [31] presented 2D electrochemical model coupled with a 3D heat transfer model to investigate the heat generation and thermal behavior of a lithium iron phosphate (LFP) cell unit. In their proposed model the reaction, active polarization and Ohmic heat generations were considered. However, solving charge conservation in 2D cannot reflect the effects of tab geometry and location on the battery thermal behavior. Xu et. al. [32] developed a pseudo 3D electrochemical-thermal model for a prismatic $LiFePO_4$/graphite cell unit. The model treated the battery with current collectors as 3D and the local cell units as 1D to constitute the 3D cell unit. Although this model showed good agreement with experimental values, it will be computationally highly expensive for a battery consisting of numerous cell units.

In order to reduce the computational time required, the majority of multidimensional non-uniform thermal models in the literature considered one unit cell as the computational domain. The total thickness of the battery is usually an order of magnitude bigger than that of a cell unit. Commonly, rough estimations are required to adopt the convection heat transfer boundary conditions for a cell unit which can severely affect the battery temperature distribution. Furthermore, the temperature gradient across the battery thickness dimension is usually ignored in the numerical modeling, however, in most thermal management systems the battery is exposed to high and non-uniform heat transfer boundary conditions which can result in considerable temperature difference in the thickness direction. Such a temperature difference will result in a rapid capacity fade and decreases the battery useful life. The battery thermal management systems are composed of numerous elements, hence the time necessary to fulfill the calculations will exceed practical requirements. Therefore, a fast simulation coupled electrochemical-thermal model is vital to reduce the computational time and attain reasonable results.

In the current study, a fast simulation pseudo three dimensional electrochemical-thermal model for a commercial 4Ah Lithium Nickel Cobalt Aluminum Oxide (NCA) battery is developed. The model is based on the coupling of mass, charge, and energy conservations, as well as electrochemical kinetics. The presented model uses a 1D local electrochemical cell unit to find the reaction and polarization heat generations as well as electrolyte concentration in the active battery material. The values of concentration substitute in a 3D electric current conservation solver to calculate the distributed Ohmic heat generation. Finally, the 3D energy conservation equation is solved to find the temperature distribution considering all three heat generation contributions.

The model numerically solved in COMSOL Multiphysics 5.2, using Finite Elements Method (FEM). Experimental verification of battery surface temperature is performed with infrared thermal imaging. The adopted simulation methodology meets Li-ion battery thermal design research requirements and allows more accurate assessment of thermal management systems for electric vehicles.

Nomenclature

c_s	concentration of lithium in the active material particles (mol m-3)
c_l	electrolyte concentration (mol m-3)
D_s	diffusion coefficient of lithium in the active material (m2 s-1)
D_l	diffusion coefficient of electrolyte (m2 s-1)
E_{aD}	diffusion activation energy (kJ mol-1)
E_{aR}	reaction activation energy (kJ mol-1)
$f_\pm$	average molar activity coefficient
F	Faraday's constant (C mol-1)
h	convective heat transfer coefficient (W m-2 K-1)
i	local working current density of the cell unit (A m-2)
j_0	exchange current density (A m-2)
j_n	local charge transfer current density (A m-2)
k_0	reaction rate constant (m2.5 mol-0.5 s-1)
k	thermal conductivity (W m-1 K-1)
L	thickness of each battery component (m)
Q_{rea}	reaction volumetric heat generation (W m-3)
Q_{pol}	polarization volumetric heat generation (W m-3)
Q_{Ohm}	Ohmic volumetric heat generation (W m-3)
R	gas constant, 8.314 (J mol-2 K-1)
r	radius distance variable of electrode particles (m)
r_0	radius of electrode particles (m)
S_a	specific surface area (m-1)
t	time (s)
t_+	transferring number of Li$^+$
T	temperature (K)
T_a	ambient temperature (K)
U_{eq}	open circuit potential of the electrode (V)
$U_{eq,ref}$	open circuit potential under the reference temperature (V)
Greek letters	
α_a	anode transfer coefficient
α_c	cathode transfer coefficient
ε	emissivity of the battery surface

ε_s	active material volume fraction
ε_l	electrolyte volume fraction
Φ_s	solid phase potential
Φ_l	electrolyte phase potential
γ	Bruggeman tortuosity exponent
σ_s	electronic conductivity in solid phase material (S m-1)
σ_l	ionic conductivity of electrolyte (S m-1)
η	local surface overpotential (V)
Subscripts and superscripts	
0	initial or equilibrated value
s	solid phase
l	electrolyte phase
eff	effective value

3.2. Experimental Setup

Figure 3-1 shows the schematic of the experimental setup. The battery under study is a 4 Ah lithium ion battery with graphite anode coated on a copper foil (as negative current collector) and NCA cathode on an aluminum foil. The battery contains a highly porous polymer separator and the battery dimensions are about 7×46×138 mm. The battery is mounted inside a constant temperature chamber to ensure uniform natural convection heat transfer from all sides. Thermal imaging measurement is conducted to investigate the temperature distribution on the surface of the battery utilizing an infrared (IR) camera. The camera resolution is 640×480 pixels and exhibits an accuracy of ±0.01 K. In order to avoid reflection in the infrared spectra all chamber interior surfaces are covered by a dark paper and to ensure a constant emission coefficient, the battery surface is coated with a very thin layer of Aluminum Chlorohydrate. The battery surface temperature with and without Aluminum Chlorohydrate coating are compared and no difference is observed.
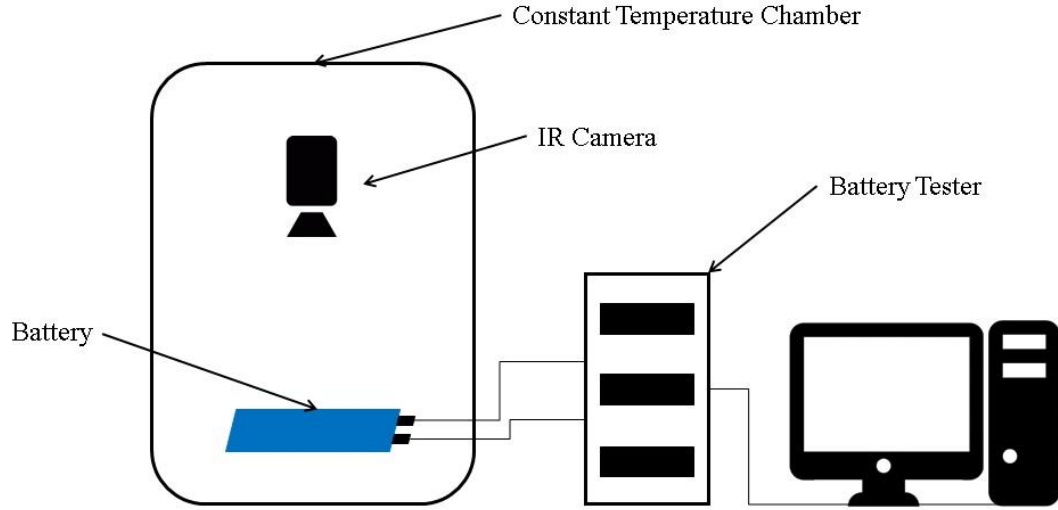
Figure 3-1. Schematic of the experimental setup

It is necessary to minimize the electrical contact resistance in order to prevent significant heat flow from the tabs contact area to the battery active material. Therefore, a conductive epoxy containing silver is used to develop a stable and relatively small contact resistance for the connection of the load cables.

Possible changes in the air flow conditions inside the constant temperature chamber have a strong effect on the temperature distribution of battery. Different procedures are described in the literature to measure the convective heat transfer coefficient [33]. In the present study, an aluminum dummy with an identical geometry of the test battery is used to determine the convective heat transfer coefficient.

The energy balance for a lumped body (valid for the dummy) can be described by the following equation [34]:

$$Q_{rej} = hA(T - T_a) + \varepsilon\sigma A\left(T^4 - T_a{}^4\right) \tag{3.1}$$

where Q_{rej} is heat rejection rate from battery, h is convection heat transfer coefficient, A is battery surface area, T and T_a are the dummy and ambient temperatures, respectively, ε is emissivity of the battery surface and σ is Stephen-Boltzmann constant.

The battery used in the experiments has a laminated aluminum jacket. Considering an emissivity of ε=0.02 for aluminum at room temperature [34] and average values of T and T_a observed in the tests, the radiation part is neglected.

In order to measure the convective heat transfer coefficient, the aluminum dummy is first heated to a high temperature (T_i) inside the chamber and then is cooled down with convection heat rejection. Neglecting radiation heat transfer, Eq. (3.1) for the dummy can be written as:

$$Q_{rej} = mC_p \frac{dT}{dt} = hA(T - T_a) \qquad (3.2)$$

with initial condition:

$$T = T_i \quad at \quad t = 0 \qquad (3.3)$$

The solution for the set of equations (3.2) and (3.3) is:

$$\ln\left(\frac{T - T_a}{T_i - T_a}\right) = st \qquad (3.4)$$

here slope is $s = \left(\frac{hA}{mC_p}\right)$.

Using a linear regression with the values of $A = 6.348 \times 10^{-3} \, m^2$, $m = 0.120 \, kg$ and $C_p = 0.9 \, kJ/kgK$ for the dummy, an average value of $h = 6.5 \pm 0.1 \, W/m^2K$ is found for the convective heat transfer coefficient and is used in the numerical simulations.

3.3. Coupled Electrochemical-thermal Model

3. 3. 1. Pseudo Model Establishment
A pseudo three-dimensional electrochemical-thermal model for a commercial NCA/graphite battery consisted of 20 double-coated single cells is developed. The nominal voltage and capacity of the battery are 3.7 V and 4 Ah, respectively.

The current within the cell components travels mainly in the direction perpendicular to the cell sandwich structure [35], therefore the model treats the single cell as 1D in this direction. The 1D model is based on porous electrode theory, and the principles of the mass, charge and energy conservations as well as the electrochemical kinetics. Application of this method involves the assumption of uniform electrochemical reactions over the electrodes. The uniformity is a desired feature for Li-ion batteries, as it means that active materials are evenly distributed and reaction current is uniform over the electrode surface. Although reaction current is not uniformly distributed over the electrodes, its impact on total heat generation is not significant during high discharge currents. At higher currents, which frequently occur in EV, the Ohmic heat generation is the dominant factor in the battery thermal behavior.

The reaction (Q_{rea}) and polarization (Q_{pol}) heat generations, as well as the electrolyte concentration distribution in y-direction are calculated in 1D solver. The values of salt concentration are inserted in the 3D computational domain, assuming that it is uniform in the direction parallel to the sandwich structure. The Ohmic heat generation (Q_{Ohm}), due to losses in the solid phase and the electrolyte phase, is calculated in the 3D domain.

Subsequently, total heat generation is used in the 3D heat transfer model to find the temperature distribution. The details of equations solved in different computational domains are listed in Table 3-1 and will be discussed in details in the following section.

Table 3-2. Governing equations in different computational and physical domains

Governing Equation	Computational Domain	Physical Domain
Electrochemical kinetics	1D	porous electrodes
Mass conservation	1D	porous electrodes and separator
Reaction heat	1D	porous electrodes
Polarization heat	1D	porous electrodes
Charge conservation	1D and 3D	all domains
Ohmic heat	3D	all domains
Energy balance	3D	all domains

3.3.2. Electrochemical Kinetics

The local charge transfer current density is determined by Butler-Volmer equation [18] as showed in equation (5):

$$j_n = j_0 \left\{ exp(\frac{\alpha_a F}{RT} \eta) - exp(-\frac{\alpha_c F}{RT} \eta) \right\} \tag{3.5}$$

where j_0 is the exchange current density, α_a and α_c are the anodic and cathodic charge transfer coefficients, respectively, F is the Faraday constant and η is the local over potential.

The exchange current density is found from equation (6) [35]:

$$j_0 = F k_0 c_l^{\alpha_a} (c_{s,max} - c_{s,surf})^{\alpha_a} c_{s,surf}^{\alpha_c} \tag{3.6}$$

where k_0 is the reaction rate constant, $c_{s,max}$ is the maximum lithium concentration in the electrodes and $c_{s,surf}$ is the lithium concentration on the surface of the active particles. The subscripts *s* and *l* represent the solid phase and electrolyte phase, respectively. The over potential is defined as [36]:

$$\eta = \Phi_s - \Phi_l - U_{eq} \tag{3.7}$$

where Φ_s is the solid phase potential, and Φ_l is the electrolyte phase potential. U_{eq} is the open circuit potential of the electrode that depends on the state of the charge (SOC) and temperature which can be approximated by a Taylor's series first order expansion:

$$U_{eq} = U_{eq,ref} + \frac{\partial U_{eq}}{\partial T}(T - T_{ref}) = U_{eq,ref} + \frac{\Delta S}{nF}(T - T_{ref}) \tag{3.8}$$

The values of open circuit voltage (U_{eq}) and the temperature derivative of open circuit voltage ($\frac{\partial U_{eq}}{\partial T}$) are showed in Fig. 3-2 (a) and (b), respectively [12, 14].
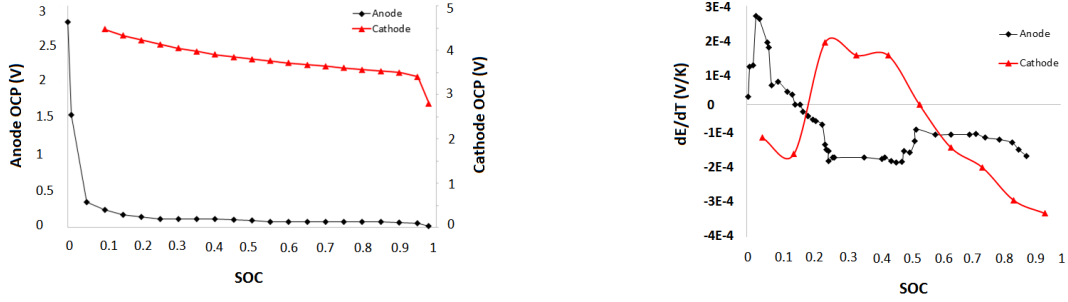
Figure 3-2. Electrodes properties as a function of SOC (a) reference open circuit potential (OCP), (b) potential-temperature coefficient [12, 14]

3.3.3. Charge Conservation

The charge conservation equations in the positive and negative electrodes are as follow [37]:

$$\nabla \cdot i_s + \nabla \cdot i_l = 0 \tag{3.9}$$
$$\nabla \cdot i_s = -S_a j_n \tag{3.10}$$
$$\nabla \cdot i_l = S_a j_n \tag{3.11}$$

where i_s refers to the electrical current density in the solid phase, i_l is the ionic current density in the electrolyte phase, and S_a is the specific surface area.

The transport of electrons in the solid phase is expressed by Ohm's law:

$$i_s = -\sigma_s^{eff} \nabla \Phi_s \tag{3.12}$$

where σ_s^{eff} is the effective electrical conductivity of the solid phase.

The transport of lithium ions in the electrolyte is defined by the following equation [38]:

$$i_l = -\sigma_l^{eff} \nabla \Phi_l + \frac{2RT\sigma_l^{eff}}{F}\left(1 + \frac{\partial ln f_{\pm}}{\partial ln c_l}\right)(1 - t_+)\nabla(ln c_l) \tag{3.13}$$

where σ_l^{eff} refers to the effective ionic conductivity of the electrolyte, $f_\pm$ is the average molar activity coefficient, t_+ is the transferring number of lithium ions in the electrolyte phase, and c_l is the lithium ion concentration in the electrolyte phase, R is the universal gas constant, and T is the electrolyte temperature.

3.3.4. Mass Conservation

The mass conservation of lithium in the spherical active material particle is expressed by equation (14) [37]:

$$\frac{\partial c_s}{\partial t} - \frac{1}{r^2}\frac{\partial}{\partial r}\left(r^2 D_s \frac{\partial c_s}{\partial r}\right) = 0 \tag{3.14}$$

where t is the time, D_s is the diffusion coefficient of lithium in the solid phase, and r represents the radial coordinate.

The mass conservation of lithium ions in the electrolyte is represented by the following equation [31]:

$$\varepsilon_l \frac{\partial c_l}{\partial t} + \nabla \cdot J_l = \frac{S_a j_n}{F} \tag{3.15}$$

where ε_l shows the volume fraction of the electrolyte phase and J_l is the molar flux of lithium ions and is defined by Eq. (16) [38]:

$$J_l = -D_l^{eff}\nabla c_l + \frac{i_l t_+}{F} \tag{3.16}$$

In this equation, D_l^{eff} is the effective diffusion coefficient of lithium ions in the electrolyte.

3.3.5 Energy Balance

The total heat generated is the summation of heat generated in the two electrodes, separator and current collectors. The primary contributions of heat sources are the reaction heat generation, Q_{rea}, polarization heat generation, Q_{pol}, and Ohmic heat generation, Q_{Ohm} [39].

The reaction heat generation is a reversible heat flow and can be calculated by the following equation [40]:

$$Q_{rea} = S_a j_n T \frac{\partial U_{eq}}{\partial T} \tag{3.17}$$

The energy needed to break the equilibrium between the Li ions' potential in the electrolyte phase, and the potential in the electrode material dissipates as polarization heat and is described by [40]:

$$Q_{pol} = S_a j_n \eta \tag{3.18}$$

Ohmic heat generation, Q_{Ohm}, is a crucial part of heat generation which is composed of electrical heat generation in the solid phase and ionic heat generation in the electrolyte phase as follow:

$$Q_{Ohm} = -i_s . \nabla \Phi_s - i_l . \nabla \Phi_l \tag{3.19}$$

The energy equation in the lithium ion battery is expressed by [34]:

$$\rho C_p \frac{\partial T}{\partial t} + \nabla . (-k \nabla T) = Q_{rea} + Q_{pol} + Q_{Ohm} \tag{3.20}$$

where ρ, C_p and k are the local density, specific heat and thermal conductivity of the battery material, respectively.

3.3.6. Parameter Evaluation

The positive and negative electrode active materials are $LiNiCoAlO_2$ (NCA) and Li_xC_6, respectively. The electrolyte is $LiPF_6$ dissolved in a mixture of 2:1 EC/DMC. The thermal-electrochemical coupled model is intrinsically nonlinear because of the strong dependence of electrochemical parameters to temperature or concentration. These parameters are the reaction rate, the open circuit potential, the potential-temperature coefficient, the ionic electrical conductivity of the liquid phase, and the diffusion coefficient of lithium ions in the liquid and solid phases.

Arrhenius equation was used to formulate the temperature dependency of reaction rate constant [41]:

$$k_0(T) = k_{0,ref} \exp \left[\frac{E_{aR}}{R} \left(\frac{1}{T_{ref}} - \frac{1}{T} \right) \right] \tag{3.21}$$

where the constant $k_{0,ref}$ is the reaction rate at the reference temperature T_{ref} and E_{aR} is the reaction activation energy.

The dependence of open circuit potential (U_{eq}) and potential-temperature coefficient ($\frac{dU_{eq}}{dT}$) on the SOC is commonly determined by experiments [22]. Fig. 3-2 presents the porous electrodes U_{eq} and $\frac{dU_{eq}}{dT}$ variation with the SOC at the reference temperature of 25°C.

The concentration and temperature dependency of electrolyte ionic electrical conductivity can be expressed as follow [42]:

$$\sigma_l(c_l, T) = 1.2544 \times 10^{-4} c_l \tag{3.22}$$
$$\times \begin{pmatrix} 0.22002 \times 10^{-6} c_l^2 + 0.26235 \times 10^{-3} c_l - \\ 0.1765 \times 10^{-9} c_l^2 T + 0.93063 \times 10^{-5} c_l T \\ +0.8069 \times 10^{-9} c_l T^2 - 0.2987 \times 10^{-5} T^2 - 8.2488 \end{pmatrix}$$

The temperature dependence diffusion coefficients in the liquid and solid phase are expressed as follow [41, 42]:

$$\log(D_l) = -\left(4.43 + \frac{54}{T - 229 - 0.005 \times c_l} + 0.0022 \times c_l\right) \tag{3.23}$$

$$D_s = [3.9 \times 10^{-14}(1.5 - SOC)^{3.5}]exp\left[\frac{E_{aD}}{R}(\frac{1}{T_{ref}} - \frac{1}{T})\right] \tag{3.24}$$

where E_{aD} is the activation energy for diffusion.

The battery geometrical and design parameters as well as kinetic, transport and thermal properties used in the numerical simulation are listed in Table 3-2.

Table3-2. Parameters used in numerical model [15, 31, 41]

Parameter (unit)	Al CC	Cathode	Electrolyte	Anode	Cu CC
c_0 (mol/m^3)	-	33956	1000	31507	-
c_p (kJ/kgK)	900	1240*	1518	1437	385
D (m^2/s)	-	1.5E-15	Eq. (23)	Eq. (24)	-
E_{aD} (kJ/mol)	-	18	-	4	-
E_{aR} (kJ/mol)	-	3	-	4	-
F (C/mol)	-	-	96487.332	-	-
k (W/mK)	160	1.3*	0.099	1.04	400

k_0 (m$^{2.5}$mol$^{-0.5}$/s)	-	3.255E-11	-	1.764E-11	-
r_0 (μm)	-	1.2	-	14.75	-
t_+	-	-	0.363	-	-
α_a, α_c	-	0.5	-	0.5	-
δ(μm)	23	46	26	48	16
ε	-	0.423	0.4	0.56	-
ρ (kg/m^3)	2700	4740	1210	5031	8960
σ (S/m)	3.8E7	3.3	Eq. (22)	100	6.3E7

3.3.7. Boundary and Initial Conditions

The insulation boundary condition is used for the electrical current of the solid phase at the electrode/separator interface. Continuity is specified for the ionic current, lithium ion flux of electrolyte phase and heat flux.

$$n.\,i_s|_{sep} = 0, n.\,i_l|_{elec} = n.\,i_l|_{sep}, n.\,J_l|_{elec} = n.\,J_l|_{sep}, n.\,Q|_{elec} = n.\,Q|_{sep} \qquad (3.25)$$

At the electrode/current collector interface, insulation is utilized for the ionic current and lithium ion flux of the electrolyte phase. Continuity was applied for the electrical current and heat flux.

$$n.\,i_l = 0, n.\,J_l = 0, n.\,i_s|_{elec} = n.\,i_s|_{cc}, n.\,Q|_{elec} = n.\,Q|_{cc} \qquad (3.26)$$

At the positive terminal, the current of the battery is applied, and the negative terminal is grounded to model discharge process:

Positive terminal: $n.\,i_s = i_{batt}$ $\qquad$ (3.27)
Negative terminal: $\Phi_s = 0$ $\qquad$ (3.28)

The battery is exposed to the natural convention heat transfer at the outer surface. Due to small temperature difference between the battery surface and surroundings, the radiation heat transfer is neglected. The following boundary condition is used in the 3D heat transfer model:

$$-n.\,Q = h(T_s - T_a) \qquad (3.29)$$

where T_s and T_a are the battery surface and ambient temperature, respectively.

The initial conditions are as follow:

$$c_s = c_{s,0}, c_l = c_{l,0}, T = T_a \tag{3.30}$$

3.3.7. Numerical Method

All equations are simultaneously solved in COMSOL Multiphysics 5.2 using the Finite Elements Method (FEM). Due to high nonlinearity of the governing equations, the performance and accuracy of the calculations strongly depend on the mesh. The mesh independency is checked to ensure reliability of the simulation results and to determine whether the decrease of mesh size influences the results or not. In the 3D solver, free quadrilateral mesh is used at the boundaries with the swept method along the battery thickness direction. Since the maximum values of current density occur near the tabs and current collectors interfaces, smaller meshes are used there. The number of elements has been varied from about 140,000 to 340,000. The mesh independency study shows that the main results i. e. current density, Ohmic heat generation and temperature are mesh independent when the number of total elements is more than about 224,000. Therefore, this mesh design is used in the simulations.

A two-way approach is used to couple the electrochemical and thermal solvers. The heat generation contributions are first calculated based on the derived values from electrochemical solver. Then, the 3D thermal solver uses the heat generations to find the temperature distribution in the battery. The distribution of temperature will be utilized in 3D solver while the average of temperature will be used in the 1D electrochemical solver. In order to save memory and time, the equations are coupled by using the segregated approach. At each time step, two segregated steps are considered: first, the temperature distribution is obtained by keeping the electrochemical variables constant; and second, the results of temperatures at each mesh node are utilized to update the local electrochemical and thermal parameters in 1D and 3D solvers. The local parameters of each mesh node are used to solve the governing equations and corresponding heat generations. The process is repeated at each node till the convergence is reached. For each time step, the maximum relative tolerance for all variables is 0.001. The computations are performed on a workstation with a 2.0 GHz eight core processor and 64 GB random access memory.

3.4. Results and Discussion

3.4.1. Model Validation

Fig. 3-3 compares the numerical and experimental cell voltages under 0.5C, 1C, 2C and 4C discharge rates. As shown in this figure, the simulated data agrees well with experimental data.
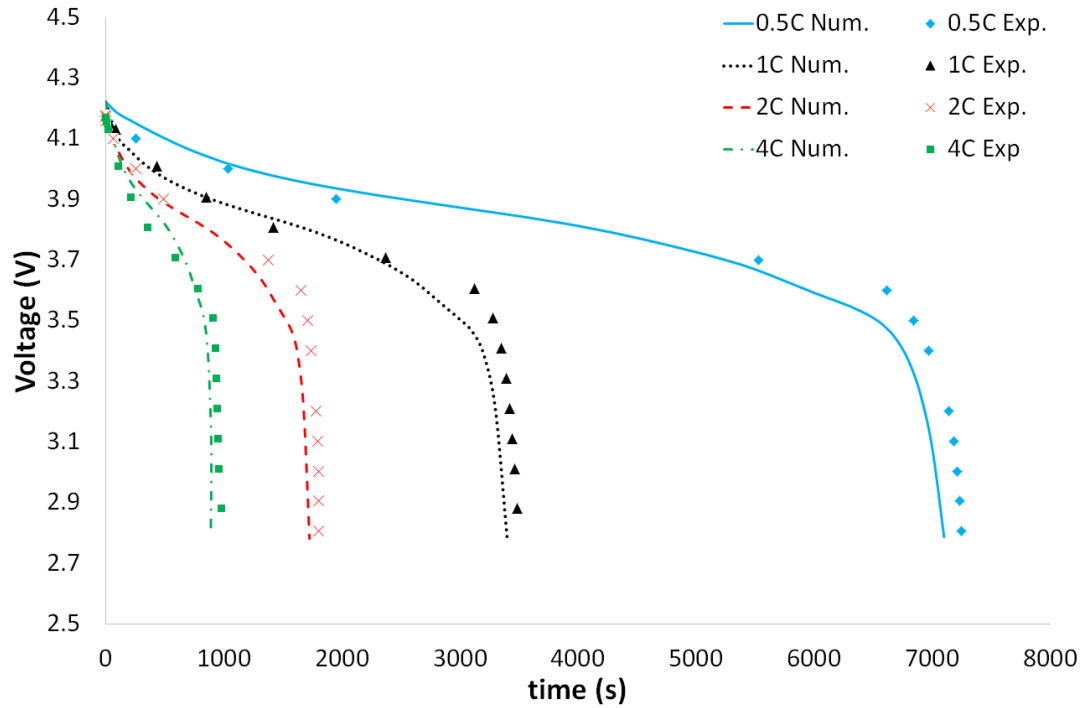
Figure 3-3. Experimental and numerical values of cell voltage for different discharge rates

The discrepancy between the numerical and experimental data becomes more evident at the late periods of the discharge process. The difference between the results can be explained as: (1) the parameters used in the simulation obtained from literature, which may differ from the real parameters of this experimental battery (2) the assumption of uniform electrochemical reaction over the active material surface does not completely hold in practice and (3) the internal equilibrium assumption may not precisely exist in the latter periods of discharge [43].

| $T_{max} = 34.15^0C, T_{min} = 32.17^0C$ | $T_{max} = 34.03^0C, T_{min} = 32.76^0C$ |
| $T_{ave} = 33.57 \ ^0C$ | $T_{ave} = 33.31 \ ^0C$ |
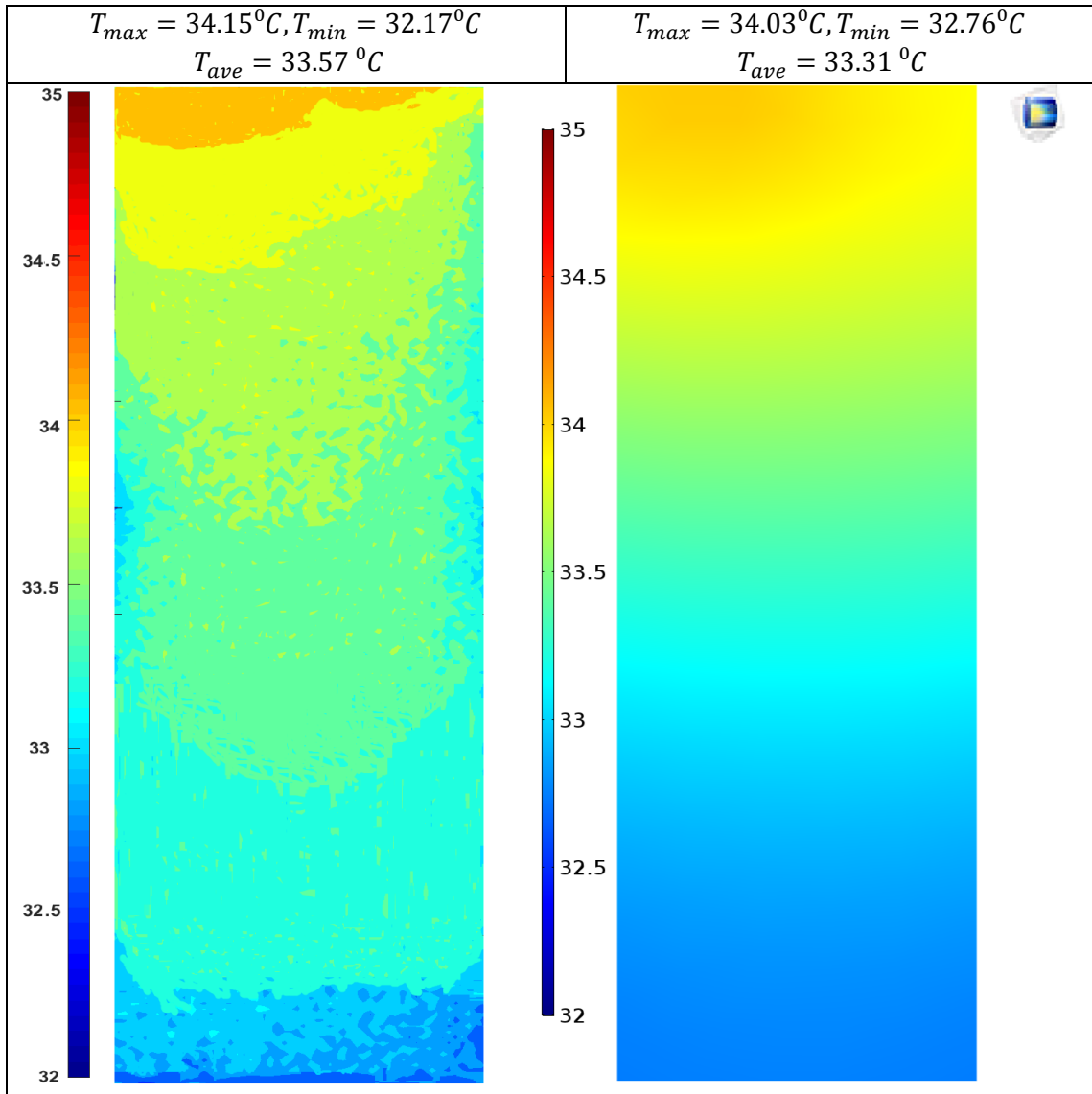
Figure 3-4. Battery thermal behavior validation under 1C discharge rate at DOD=75%
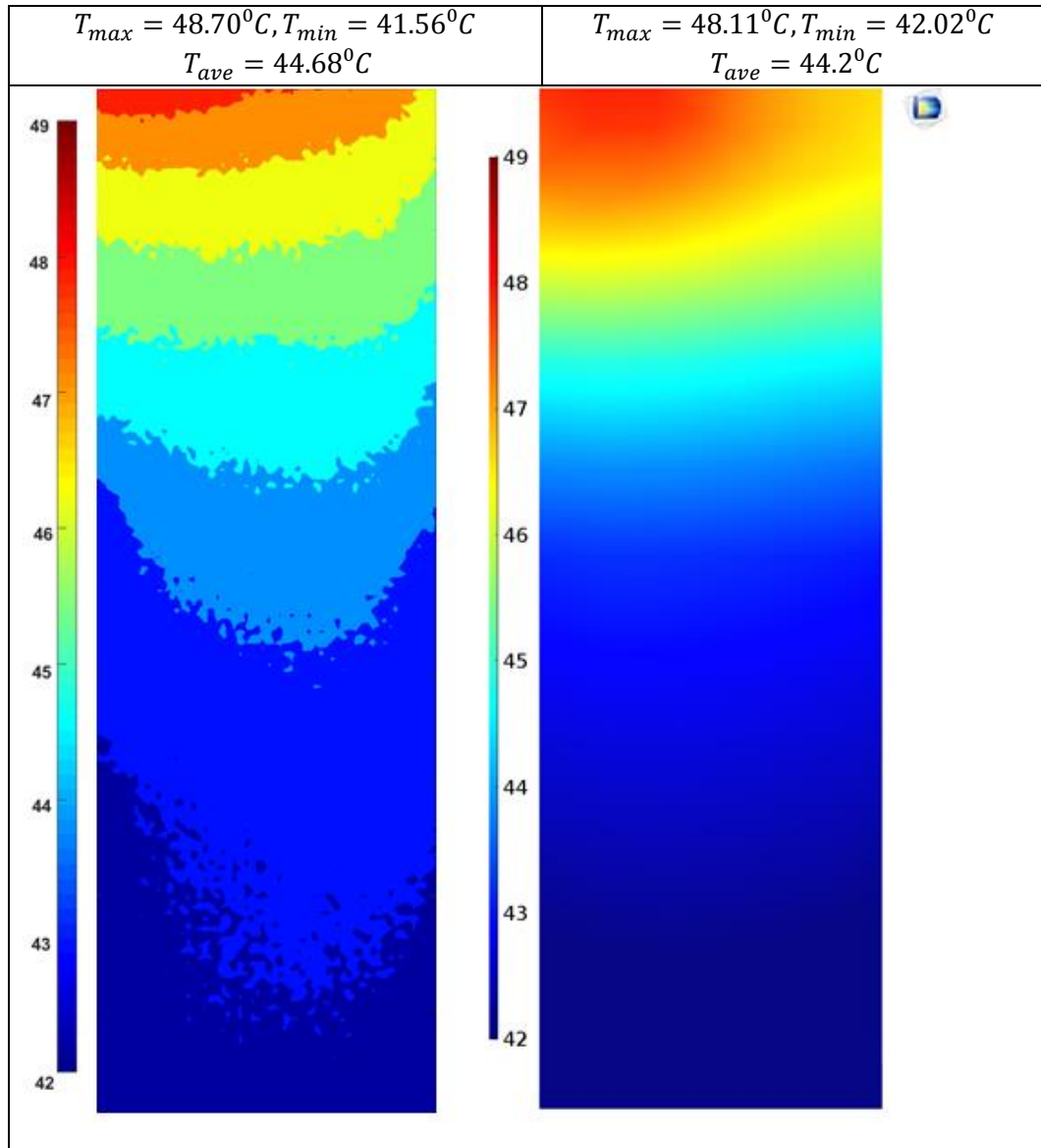
Figure 3-5. Battery thermal behavior validation under 4C discharge rate at DOD=75%

In order to validate the battery thermal behavior, the simulation results are compared with the infrared thermography at 1C and 4C discharge rates in Fig. 3-4 and 3-5. The results indicate that the present electrochemical-thermal model is a reliable tool to estimate the thermal behavior of NCA Li-ion batteries and is advantageous in fast simulating of the battery temperature distribution under different C-rates. However, the average temperature increase is slightly underestimated and the battery surface temperature is more evenly distributed in the simulations. The observed difference between the infrared thermography and simulation results are due to several factors that are explained below. Although every effort has been made to minimize the contact resistance between the load cables and battery tabs, a small electrical contact resistance is inevitable. A part of the

heat generated at the connecting tabs penetrates to the active material resulting in a higher and more non-uniform temperature distribution. In simulations, the battery is considered to be made of an idealized and uniform active material. However, it is highly challenging to achieve a uniform distribution of the internal active materials because of the actual battery manufacturing and packaging limitations. Finally, the electrochemical reactions are assumed to be uniform over the electrodes surfaces. This assumption results in overestimation and underestimation of heat generation in low and high temperature regions, respectively. This is due to reaction heat generation increment with temperature. In general, considering these sources of distinction between numerical and experimental results, the adopted model evaluates the thermal behavior of the Li-ion battery with an acceptable accuracy required for BTMS design and evaluation purposes.

3.4.2 Heat Generation Analysis
The measured and calculated average surface temperatures are compared in Fig. 3-6 for 0.5C, 1C, 2C and 4C discharge rates. The temperature rise at the end of 0.5C discharge is about 3.8°C, and the cell temperature significantly rises above the ambient temperature as the C-rate increases.
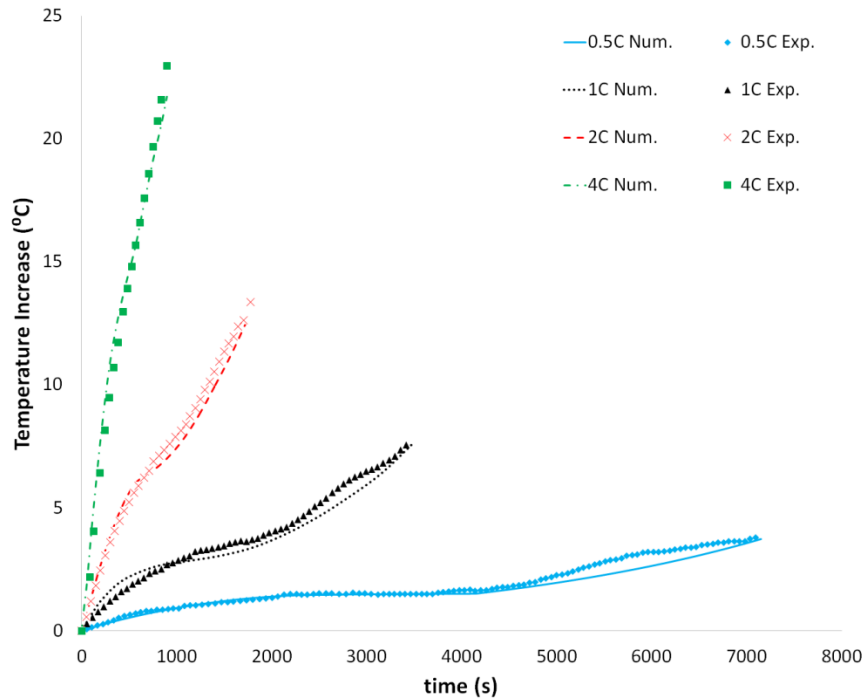
Figure 3-6. Numerical and experimental values of average surface temperature during various discharge rates

The discrepancy between measured and predicted values is more considerable at 4C discharge rate due to higher Ohmic heat generation from the contact resistance at tabs.

44

The temperature rise shows two rapid increments, one at the beginning and one at the end of discharge. This trend can be explained by the heat generation variation as a function of depth of discharge (DOD) as shown in Fig. 3-7.
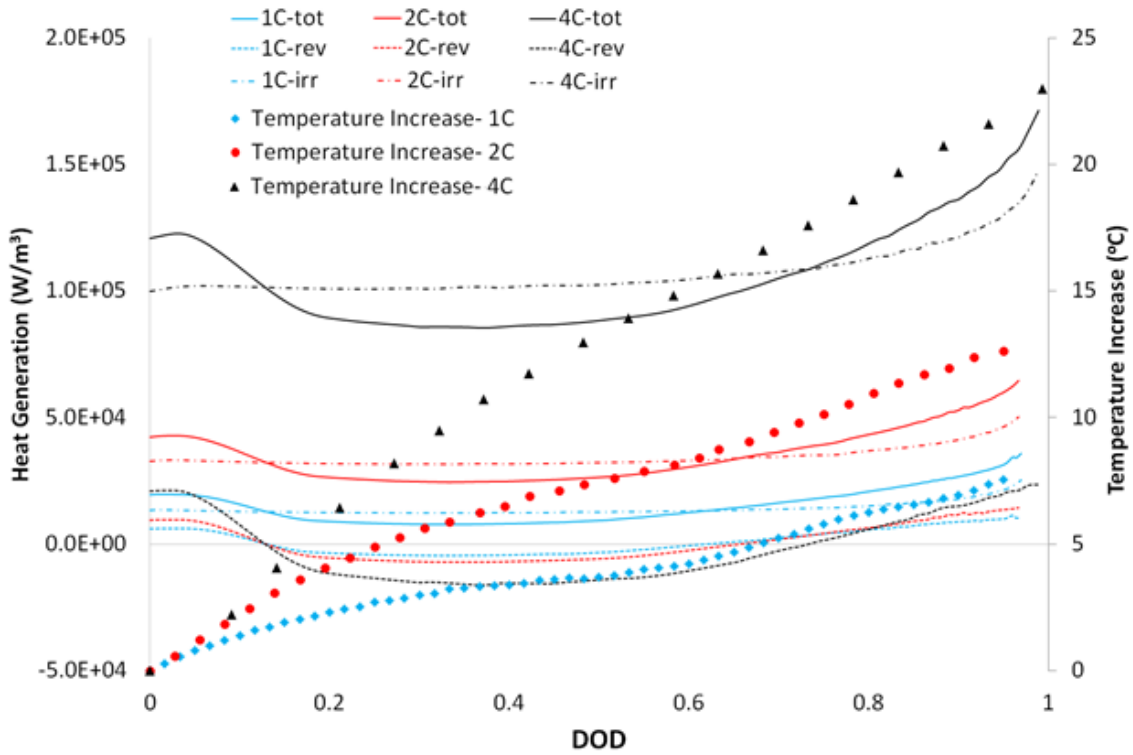
Figure 3-7. Experimental temperature variation and numerical values of total heat generation as functions of DOD

The total, reversible and irreversible heat generation rates, as well as temperature increase under different discharge rates are plotted in Fig. 3-7. Total heat generation inside a battery is a combination of reversible and irreversible components. The irreversible heat generation, composed of polarization and Ohmic contributions, is exothermic and increases with an increment in C-rate. It can be seen that the irreversible heat, and consequently the total heat, rises greatly with increasing discharge current. The Ohmic heat is quadratic dependent on current whereas reversible heat is proportional dependent on current. This shows why the irreversible heat is dominant at larger discharge currents. As presented in Fig. 5, the irreversible heat curve is stable over a wide range of DOD and increases at the end of discharge mainly due to sharp increment in battery internal resistance [5,19,20]. The variation of total heat generation at smaller DOD values mostly depends on the SOC influence on the reversible heat. As Fig. 2 (b) and Eq. (17) suggest,

the reversible heat is an exothermic process in the initial stages of discharge (DOD<0.15), then gradually transforms into an endothermic process and finally becomes exothermic (DOD~0.7) as the discharge process progresses. Fig. 3-7 evidently shows the strong effect of SOC on thermal stability of NCA batteries. The battery rapid temperature elevation and consequently its thermal safety issues can be avoided by limiting the operational SOC (in this case 0.2<DOD<0.8).

The reversible heat is a function of SOC and significantly depends on the chemistry of the porous electrodes. In order to clarify the impact of different parameters on irreversible and reversible heats inside NCA batteries, Fig. 3-8 to 3-10 show irreversible, reversible and total heat generations at different single cell components under 1C discharge rate. In these figures, the reaction and polarization heat generation are calculated in 1D domain, whereas the Ohmic heat equation (Eq. (3-19)) is solved in 3D domain and its distribution along the battery thickness (*y*-direction) is calculated as follow:

$$Q_{Ohm(y)} = \int_0^{z=h_{batt}} \int_0^{x=w_{batt}} Q_{Ohm(x,y,z)} \, dxdz \qquad (3.31)$$
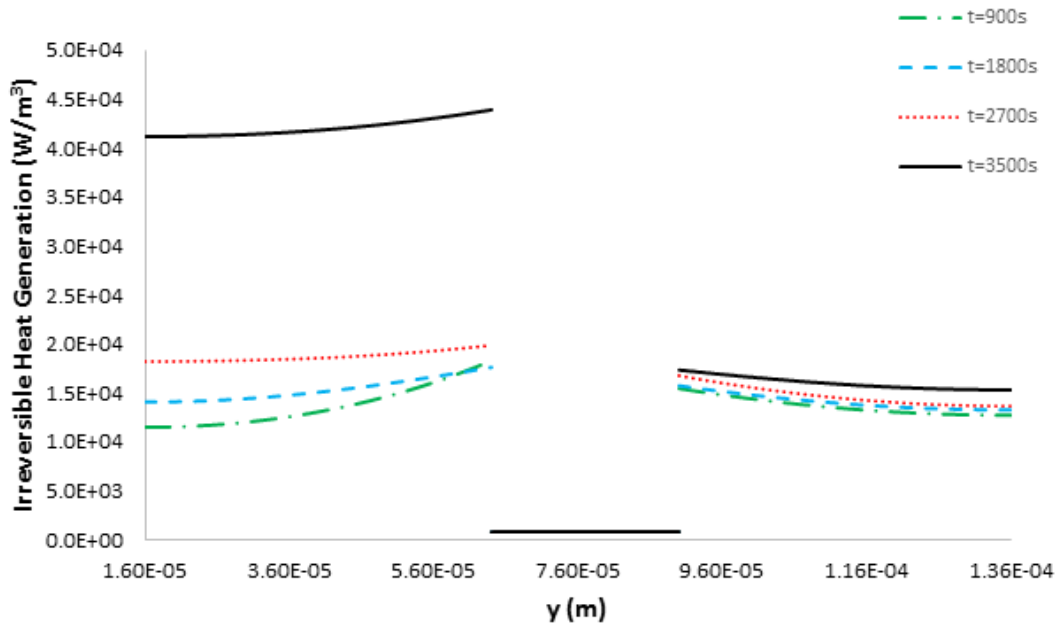
Figure 3-8. Distribution of irreversible heat generation in the porous electrodes and separator under 1C discharge rate
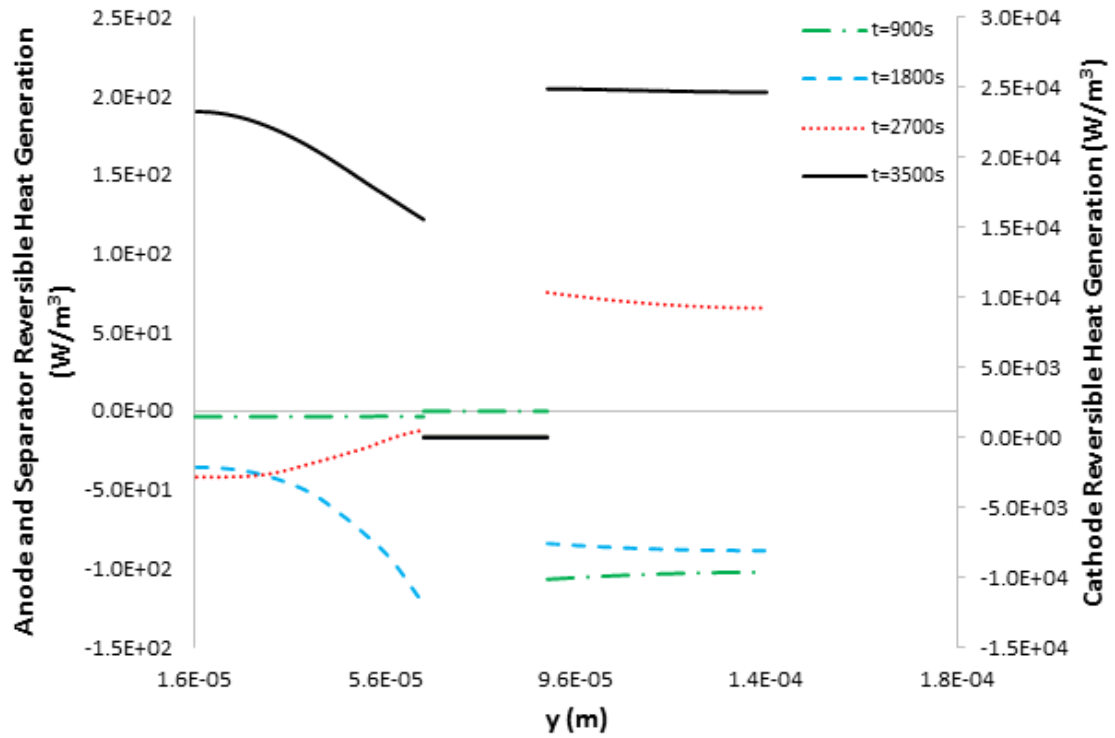
Figure 3-9. Distribution reversible heat generation in the porous electrodes and separator under 1C discharge rate
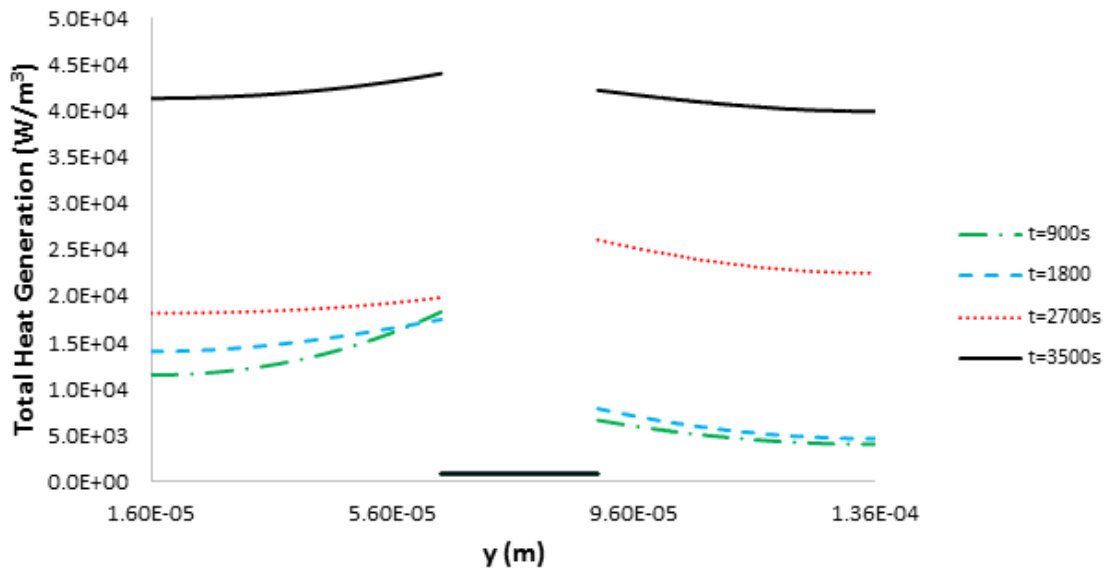
Figure 3-10. Distribution of total heat generation in the porous electrodes and separator under 1C discharge rate

Heat generation in current collectors is considered in 3D solver, however, the heat of current collectors originates from the electric current passing through them and due to the superb electrical conductivity of Copper and Aluminum is negligible [44]. Considering the irreversible heat as the sum of Ohmic and polarization heats, its variation with thickness and time can be explained. Ohmic heat is produced from the resistance of transportation of Li-ions during electrochemical reactions. Because more Li-ions flow through the interfaces between electrodes and separator than other areas, more Ohmic heat is generated at the separator/electrode interface.

As an indicator of polarization heat, overpotential in porous electrodes is plotted in Fig. 3-11. It can be observed that the overpotential is nearly constant through the thickness of both electrodes with a slight growth in regions close to the separator. However, it significantly increases with time which suggests a rapid rise in this heat contribution. As figure 2 (b) depicts, the magnitude of potential-temperature coefficient ($\frac{dE_{eq}}{dT}$) is greater for positive electrode except the values of 0<SOC<0.17 which explains why reversible heat in the positive electrode is more significant than the negative electrode. The endothermic and exothermic heat contributions are in agreement with the sign of potential-temperature coefficients in Fig. 2 (b). The negative electrode uneven heat distribution is due to its non-uniform SOC distribution which is consistent with the literature [45–47].
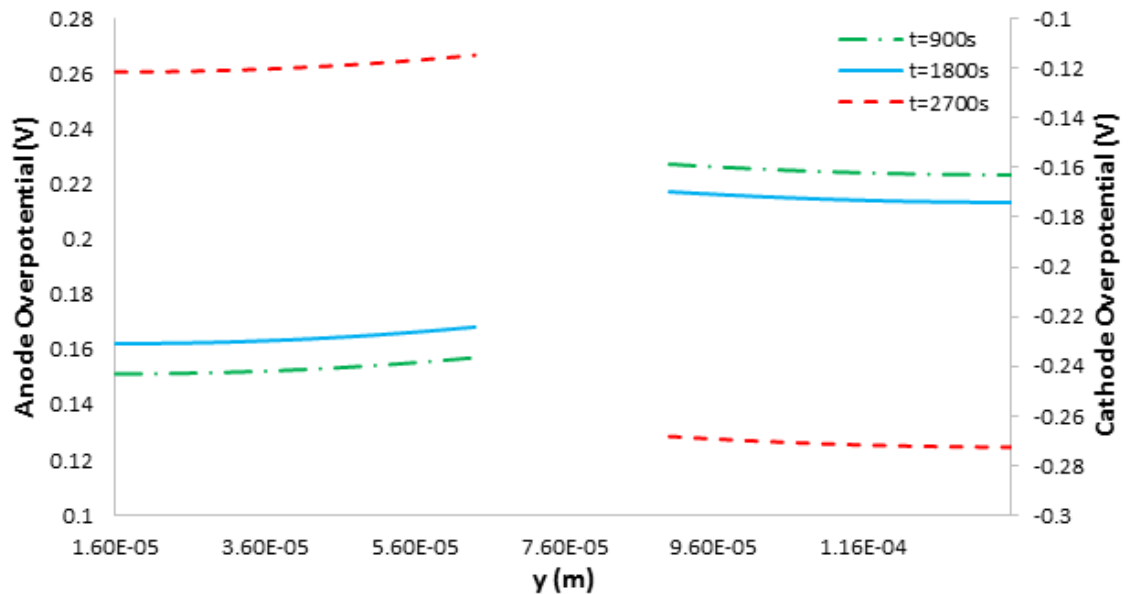
Figure 3-11. Overpotential distribution under 1C discharge rate at DOD=50%
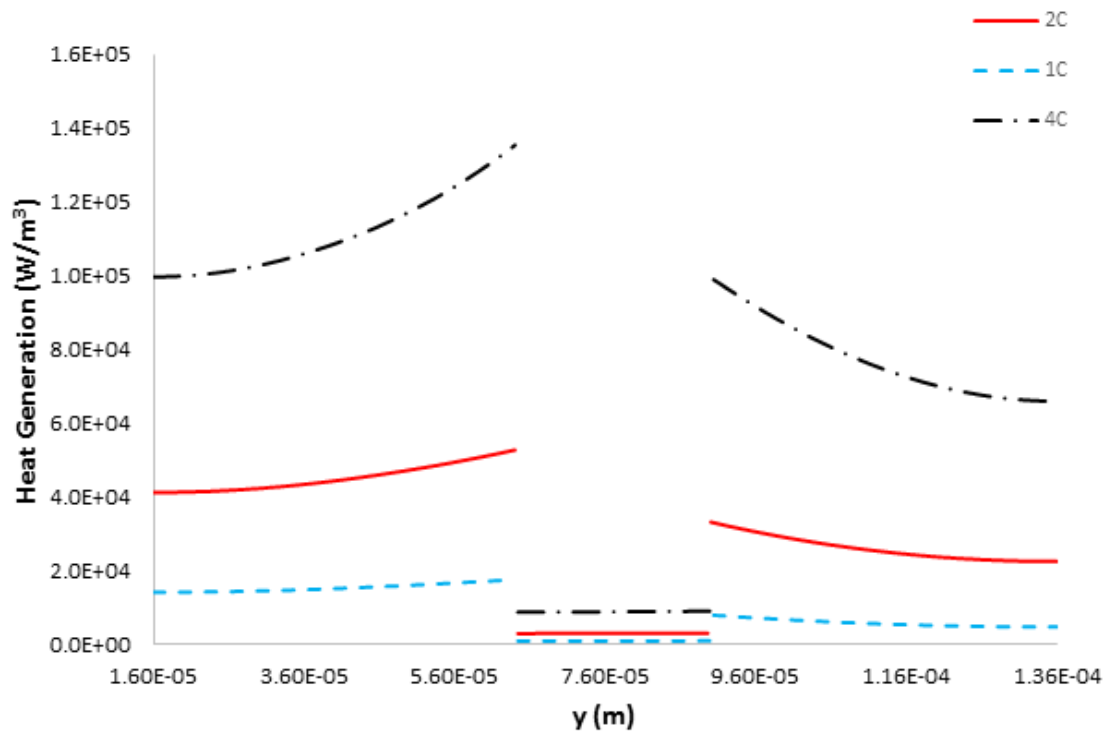
Figure 3-12. Total heat generation distribution in the active material under different discharge rates at DOD=50%

Figure 3-12 shows the effects of C-rate on the total heat generation distribution in the cell. The uneven heat distribution depicted in this figure increases the overall thermal instability across the electrochemical cell especially in the regions close to the separator. This phenomenon will finally lead to uneven fading rate across the electrodes and affect the performance and safety of the battery. There is no reaction heat generation in the separator and heat mainly originates from the process of lithium ions passing through it. At all discharge rates presented in Fig. 3-12, the heat generation inside the separator is relatively small compared with that in porous electrodes, proving to have little impact on the battery temperature distribution. Furthermore, the heat generation in separator tends to have a constant value which suggests that this component, as well as current collectors, can be modeled as 0D to save the computational time.

In order to obtain a better understanding of heat generation distribution, the Ohmic heat generation over both electrodes and separator surface under 1C discharge rate at DOD=50% is plotted in Fig. 3-13 (a)-(c). In this figure the heat generation over the surface is calculated as follow:

$$Q_{(x,z)} = \int_0^L Q_{(x,y,z)} dy \qquad (3.32)$$

where L is the thickness of corresponding component and $Q_{(x,y,z)}$ is calculated by 3D solver.

Since the values of current density, and consequently Ohmic heat, varies from extremely high values at the vicinity of tabs to small values at the other end of electrodes, Fig. 8 is plotted on logarithmic scale. The 2D heat distribution, as depicted in Fig. 3-13, combined with 1D heat distribution shown in Fig. 3-12, provides a comprehensive 3D demonstration of Ohmic heat generation in the porous electrodes and separator.
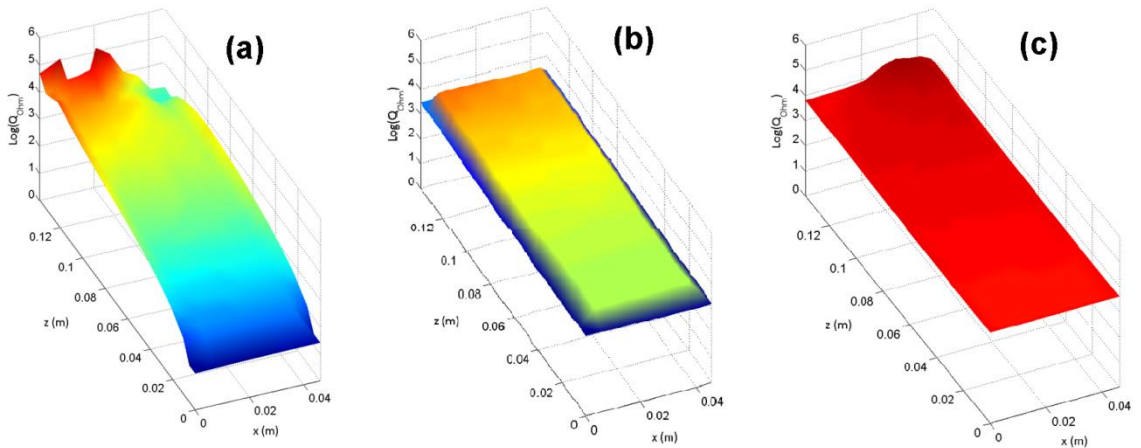
Figure 3-13. Logarithmic Ohmic heat generation distribution on (a) positive electrode, (b) separator and (c) negative electrode under 1C discharge rate at DOD=50%

As shown in Fig. 3-13 (a) and (c), a sharp increase in the current density occurs in the vicinity of electrode tabs due to constriction of the current flow [48] which leads to high Ohmic heating at the tabs. At high discharge rates, this high Ohmic heating and the resulted temperature rise near the tabs increases the rate of electrochemical reactions and the risk of thermal runaway. It is a reminder for designers to adjust the tab design parameters in order to achieve a smoother current flow path at the connecting edge of tabs and collectors. The dissimilarities in the Ohmic heat pattern between the positive and negative electrodes are because of different boundary conditions, as well as different electrical and thermal properties utilized. Note that the higher heat generation in the cathode tends to shift the maximum temperature to the positive tab which is in consistency with temperature distribution shown in Fig. 3-4 and 3-5. Separator exhibits a

relatively uniform heat generation with a higher value close to tabs due to higher normal current density. Ohmic heat is considerably smaller at the separator edges because heat in separator mainly arises from the normal current passing through it which is lower at the edges. This trend can negatively affect the heat dissipation from the battery since the heat generated accumulates at the center of the battery.

3.4 3. Application in Thermal Management Systems

One of the most catastrophic safety issues of a lithium-ion battery is cascading thermal runaway, where multiple cells in a battery fail due to an individual cell failure. Numerical investigations showed that conductivity of the electrolyte increases with temperature, causing more current to be directed to hotter sections of the battery. This generates more Ohmic heat in hotter regions, raising the temperature and allowing even more current to pass through it. This positive feedback has the potential to lead to thermal runaway [23]. Hence, one of the main objectives of BTMS is to reduce the battery temperature non-uniformity. Numerical modeling of BTMS involves fluid flow (in active systems) or phase change heat transfer (in passive systems) highly time demanding models. Thus, researchers have widely employed the lumped thermal models for batteries to save the computational time required [1,49–52]. Therefore, a fast simulation electrochemical-thermal model capable of estimating battery temperature gradient under different cooling scenarios is a valuable tool to enhance the safety and performance of lithium batteries in electric vehicles.

Fig. 3-14 (a)-(c) depict the temperature distribution over the active material surface and along its thickness under 4C discharge rate and at DOD=70%. To mimic an ideal air cooling system, the battery thermal behavior is modeled under high convection heat transfer coefficient (h=20 W/m^{2}K) and the results are compared with those from natural convection scenario. As shown Fig. 3-14 (a), both maximum temperature and surface temperature non-uniformity are successfully reduced by applying higher heat transfer coefficient. These two parameters are widely used in the literature as criteria for assessing BTMS [9,21,22,41] since the temperature is usually considered uniform along battery thickness direction.

Fig. 3-14 (b) shows the temperature distribution on the battery thickness under the natural convection heat transfer case (tabs are not shown). The maximum temperature difference in this figure is 1.8°C and 0.8°C at the top and bottom of the battery, respectively. The maximum temperature at the top of the battery occurs at the vicinity of tabs and positive current collector due to the high Ohmic heat generation as previously shown in Fig. 3-14 (b). In the absence of the tabs, the temperature is more uniform at the bottom of the battery. This figure shows that the uniform temperature assumption is not necessarily valid at high C-rates although the temperature at the corresponding points on the front and back surfaces is nearly equal.
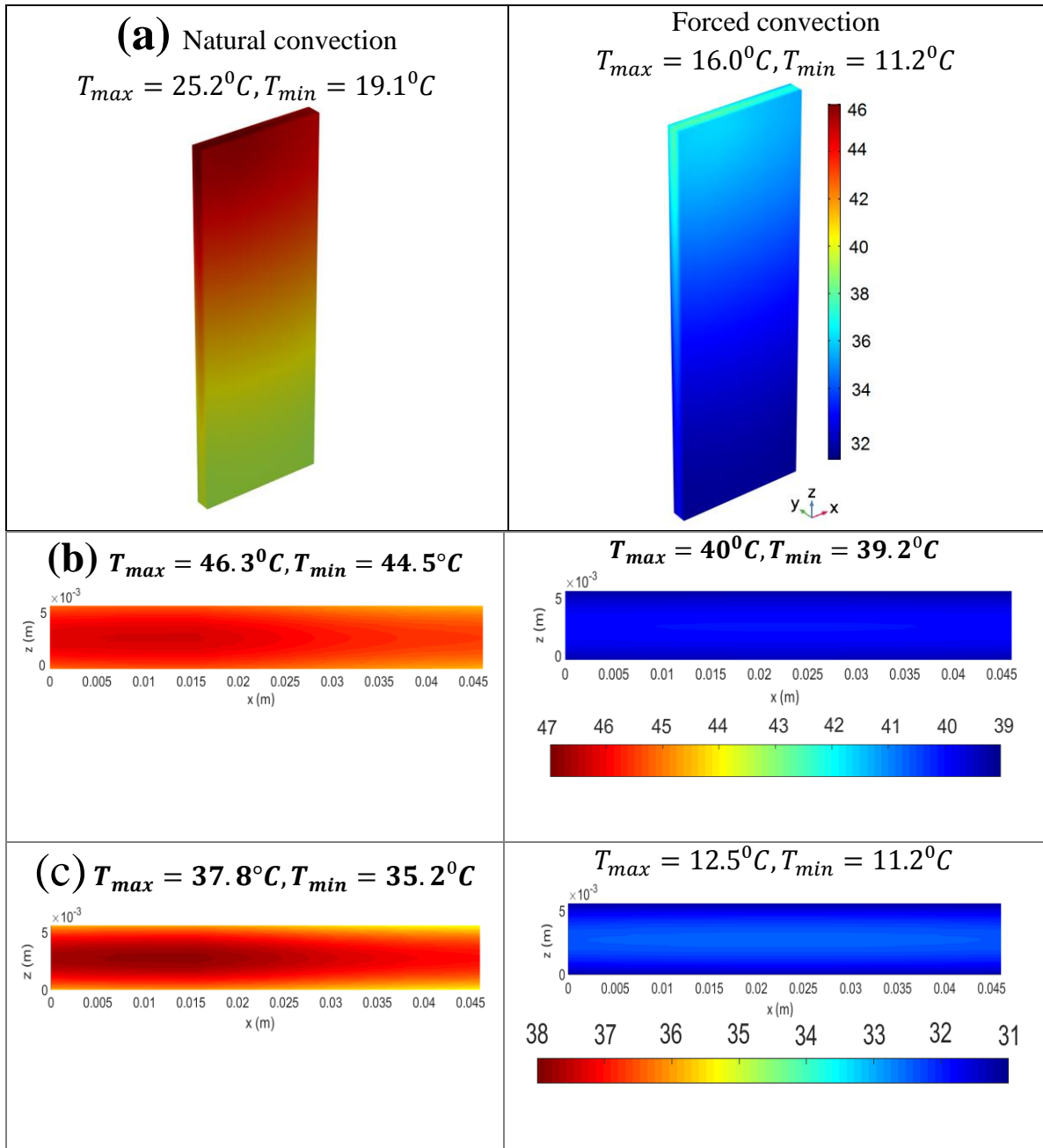
Figure 3-14. Temperature distribution under 4C discharge rate at DOD=70%. (a) active material surface, (b) top and bottom of active material thickness under natural convection and (c) top and bottom of active material thickness under forced convection

Figure 3-14 (c) depicts that the temperature difference in the battery thickness direction surprisingly increases in comparison with natural convection cooling. This shows that in the case of inappropriate thermal management strategy, considerable temperature difference along the battery thickness forms which can lead to premature capacity fading

of the inner cells. In addition, the higher temperatures observed in this figure can trigger the thermal runaway. Therefore, temperature gradient along battery thickness should be considered as a criterion for evaluating thermal management systems since decreasing maximum temperature and temperature non-uniformity on the battery surface does not necessarily lower temperature gradients in the thickness direction. An approach to reduce the mentioned temperature gradient is to reduce the battery thickness. However, this requires a larger electrode surface to achieve a specific energy capacity which will increase temperature non-uniformity on the battery surface. These observations suggest designers seek a trade-off between the active material surface area and thickness.

Conclusions

A simplified pseudo 3D coupled electrochemical-thermal model for an NCA prismatic battery that can be implemented into the automotive BTMS is developed. The presented model featured a greater degree of accuracy in predicting battery thermal responses compared with the lumped or empirical thermal models. The non-uniform Ohmic heat generation and temperature distributions during different discharge rates are considered in the model. The verification of the electrical and thermal predictions is carried out by comparing the numerical results with experimental data from a 4Ah NCA prismatic battery. The model showed good agreement with the experimental data, which suggests that the presented methodology can be used for the analysis of the battery thermal behavior for electric vehicle applications. During the high discharge rates, the Ohmic heat generation is dominant and the uniform reaction rate assumption results in reasonable temperature distribution estimations. The location and geometry of the positive and the negative current collecting tabs has a significant effect on the distributions of current density distribution and therefore the heat generation and temperature distribution within the battery. Temperature gradients along the battery thickness direction can be considerable even in the case of high forced convection cooling and should be considered in the design of any BTMS. The contact resistance between the cell unit components has been rarely considered in the literature. The model can be extended to include the effects of the electrical and thermal contact resistance between the cell components, and the effects of solid electrolyte interface (SEI) layer which can result in more accurate estimations of the temperature gradient, capacity fade and rate capability of the Li-ion batteries.

References

[1]   Z. Ling, Z. Zhang, G. Shi, X. Fang, L. Wang, X. Gao, Y. Fang, T. Xu, S. Wang, X. Liu, Review on thermal management systems using phase change materials for electronic components, Li-ion batteries and photovoltaic modules, Renew. Sustain. Energy Rev. 31 (2014) 427–438. doi:10.1016/j.rser.2013.12.017.

[2]   Z.G. Qu, W.Q. Li, W.Q. Tao, Numerical model of the passive thermal management system for high-power lithium ion battery by using porous metal foam saturated with phase change material, Int. J. Hydrogen Energy. 39 (2014) 3904–3913. doi:10.1016/j.ijhydene.2013.12.136.

[3]   T. Teratani, R. Mizutani, K. Yamamoto, T. Anegawa, Energy-saving technologies for automobiles, IEEJ Trans. Electr. Electron. Eng. 3 (2008) 162–175. doi:10.1002/tee.20252.

[4]   A. Ritchie, W. Howard, Recent developments and likely advances in lithium-ion batteries, J. Power Sources. 162 (2006) 809–812. doi:10.1016/j.jpowsour.2005.07.014.

[5]   T.M. Bandhauer, S. Garimella, T.F. Fuller, A Critical Review of Thermal Issues in Lithium-Ion Batteries, J. Electrochem. Soc. 158 (2011) R1. doi:10.1149/1.3515880.

[6]   N. Omar, M.A. Monem, Y. Firouz, J. Salminen, J. Smekens, O. Hegazy, H. Gaulous, G. Mulder, P. Van den Bossche, T. Coosemans, J. Van Mierlo, Lithium iron phosphate based battery - Assessment of the aging parameters and development of cycle life model, Appl. Energy. 113 (2014) 1575–1585. doi:10.1016/j.apenergy.2013.09.003.

[7]   A. Barré, B. Deguilhem, S. Grolleau, M. Gérard, F. Suard, D. Riu, A review on lithium-ion battery ageing mechanisms and estimations for automotive applications, J. Power Sources. 241 (2013) 680–689. doi:10.1016/j.jpowsour.2013.05.040 Review.

[8]   Q. Wang, P. Ping, X. Zhao, G. Chu, J. Sun, C. Chen, Thermal runaway caused fire and explosion of lithium ion battery, J. Power Sources. 208 (2012) 210–224. doi:10.1016/j.jpowsour.2012.02.038.

[9]   C.Y. Jhu, Y.W. Wang, C.M. Shu, J.C. Chang, H.C. Wu, Thermal explosion hazards on 18650 lithium ion batteries with a VSP2 adiabatic calorimeter, J. Hazard. Mater. 192 (2011) 99–107. doi:10.1016/j.jhazmat.2011.04.097.

[10]   M. Doyle, Modeling of Galvanostatic Charge and Discharge of the Lithium/Polymer/Insertion Cell, J. Electrochem. Soc. 140 (1993) 1526. doi:10.1149/1.2221597.

[11]   P.M. Gomadam, J.W. Weidner, R.A. Dougal, R.E. White, Mathematical modeling of lithium-ion and nickel battery systems, J. Power Sources. 110 (2002) 267–284. doi:10.1016/S0378-7753(02)00190-8.

[12]   V. Srinivasan, C.Y. Wang, Analysis of Electrochemical and Thermal Behavior of Li-Ion Cells, J. Electrochem. Soc. 150 (2003) A98. doi:10.1149/1.1526512.

[13]   A. Awarke, S. Pischinger, J. Ogrzewalla, Pseudo 3D Modeling and Analysis of the SEI Growth Distribution in Large Format Li-Ion Polymer Pouch Cells, J. Electrochem. Soc. 160 (2013) A172–A181. doi:10.1149/2.022302jes.

[14]   A. Eddahech, O. Briat, J.M. Vinassa, Thermal characterization of a high-power lithium-ion battery: Potentiometric and calorimetric measurement of entropy changes, Energy. 61 (2013) 432–439. doi:10.1016/j.energy.2013.09.028.

[15]   R.S. Patil, V.A. Juvekar, Analysis of multiparticle bipolar electrolysis using single particle cell model, Chem. Eng. Sci. 110 (2014) 72–82. doi:10.1016/j.ces.2013.12.003.

[16]   X. Hu, S. Li, H. Peng, A comparative study of equivalent circuit models for Li-ion batteries, J. Power Sources. 198 (2012) 359–367. doi:10.1016/j.jpowsour.2011.10.013.

[17]   L.H. Saw, Y. Ye, A.A.O. Tay, Electro-thermal characterization of Lithium Iron Phosphate cell with equivalent circuit modeling, Energy Convers. Manag. 87 (2014) 367–377. doi:10.1016/j.enconman.2014.07.011.

[18]   V. Ramadesigan, P.W.C. Northrop, S. De, S. Santhanagopalan, R.D. Braatz, V.R. Subramanian, Modeling and Simulation of Lithium-Ion Batteries from a Systems Engineering Perspective, J. Electrochem. Soc. 159 (2012) R31–R45. doi:10.1149/2.018203jes.

[19]   J. Jaguemont, L. Boulon, Y. Dubé, A comprehensive review of lithium-ion batteries used in hybrid and electric vehicles at cold temperatures, Appl. Energy. 164 (2016) 99–114. doi:10.1016/j.apenergy.2015.11.034.

[20]   A. Fotouhi, D.J. Auger, K. Propp, S. Longo, M. Wild, A review on electric vehicle battery modelling: From Lithium-ion toward Lithium-Sulphur, Renew. Sustain. Energy Rev. 56 (2016) 1008–1021. doi:10.1016/j.rser.2015.12.009.

[21]   Q. Wang, B. Jiang, B. Li, Y. Yan, A critical review of thermal management models and solutions of lithium-ion batteries for the development of pure electric vehicles, Renew. Sustain. Energy Rev. 64 (2016) 106–128. doi:10.1016/j.rser.2016.05.033.

[22]   R. Zhao, S. Zhang, J. Liu, J. Gu, A review of thermal performance improving methods of lithium ion battery: Electrode modification and thermal management system, J. Power Sources. 299 (2015) 557–577.

doi:10.1016/j.jpowsour.2015.09.001.

[23]   Z. Rao, S. Wang, M. Wu, Z. Lin, F. Li, Experimental investigation on thermal management of electric vehicle battery with heat pipe, Energy Convers. Manag. 65 (2013) 92–97. doi:10.1016/j.enconman.2012.08.014.

[24]   A. Greco, D. Cao, X. Jiang, H. Yang, A theoretical and computational study of lithium-ion battery thermal management for electric vehicles using heat pipes, J. Power Sources. 257 (2014) 344–355. doi:10.1016/j.jpowsour.2014.02.004.

[25]   S. Al-Hallaj, J.. Selman, Thermal modeling of secondary lithium batteries for electric vehicle/hybrid electric vehicle applications, J. Power Sources. 110 (2002) 341–348. doi:10.1016/S0378-7753(02)00196-9.

[26]   D. Bernardi, E. Pawlikowski, J. Newman, A General Energy Balance for Battery Systems, 132 (1970).

[27]   Z.H. Che Daud, D. Chrenko, E.-H. Aglzim, A. Keromnes, L. Le Moyne, Experimental Study of Lithium-Ion Battery Thermal Behaviour for Electric and Hybrid Electric Vehicles, 2014 IEEE Veh. Power Propuls. Conf. (2014) 1–6. doi:10.1109/VPPC.2014.7007069.

[28]   J. Jiang, H. Ruan, B. Sun, W. Zhang, W. Gao, L.Y. Wang, L. Zhang, A reduced low-temperature electro-thermal coupled model for lithium-ion batteries, Appl. Energy. 177 (2016) 804–816. doi:10.1016/j.apenergy.2016.05.153.

[29]   C.R. Pals, J. Newman, Thermal Modeling of the Lithium / Polymer Battery, 142 (1995).

[30]   C.R. Pals, J. Newman, Thermal Modeling of the Lithium / Polymer Battery - II. Temperature profiles in cell stack, J. Electrochem. Soc. 142 (1995) 3282–3288. doi:10.1149/1.2049975.

[31]   Y. Lai, S. Du, L. Ai, L. Ai, Y. Cheng, Y. Tang, M. Jia, Insight into heat generation of lithium ion batteries based on the electrochemical-thermal model at high discharge rates, Int. J. Hydrogen Energy. 40 (2015) 13039–13049. doi:10.1016/j.ijhydene.2015.07.079.

[32]   M. Xu, Z. Zhang, X. Wang, L. Jia, L. Yang, A pseudo three-dimensional electrochemical–thermal model of a prismatic LiFePO4 battery during discharge process, Energy. 80 (2015) 303–317. doi:10.1016/j.energy.2014.11.073.

[33]   E. Schuster, C. Ziebert, A. Melcher, M. Rohde, H.J. Seifert, Thermal behavior and electrochemical heat generation in a commercial 40 Ah lithium ion pouch cell, J. Power Sources. 286 (2015) 580–589. doi:10.1016/j.jpowsour.2015.03.170.

[34] A. Bejan, A.D. Kraus, Heat Transfer Handbook, JohnWiley & Sons, Inc., Hoboken, New Jersey, 2003.

[35] M. Doyle, Comparison of Modeling Predictions with Experimental Data from Plastic Lithium Ion Cells, J. Electrochem. Soc. 143 (1996) 1890. doi:10.1149/1.1836921.

[36] W. Fang, O.J. Kwon, C. Wang, Electrochemical – thermal modeling of automotive Li-ion batteries and experimental validation using a three-electrode cell, (2010) 107–115. doi:10.1002/er.

[37] K. Uddin, S. Perera, W. Widanage, L. Somerville, J. Marco, Characterising Lithium-Ion Battery Degradation through the Identification and Tracking of Electrochemical Battery Model Parameters, Batteries. 2 (2016) 13. doi:10.3390/batteries2020013.

[38] V.R. Subramanian, V. Boovaragavan, V. Ramadesigan, M. Arabandi, Mathematical Model Reformulation for Lithium-Ion Battery Simulations: Galvanostatic Boundary Conditions, J. Electrochem. Soc. 156 (2009) A260. doi:10.1149/1.3065083.

[39] W.B. Gu, C.Y. Wang, Thermal-Electrochemical Modeling of Battery Systems, J. Electrochem. Soc. 147 (2000) 2910. doi:10.1149/1.1393625.

[40] W. Huo, H. He, F. Sun, Electrochemical–thermal modeling for a ternary lithium ion battery during discharging and driving cycle testing, RSC Adv. 5 (2015) 57599–57607. doi:10.1039/C5RA09018K.

[41] S. Abada, G. Marlair, A. Lecocq, M. Petit, V. Sauvant-Moynot, F. Huet, Safety focused modeling of lithium-ion batteries: A review, J. Power Sources. 306 (2016) 178–192. doi:10.1016/j.jpowsour.2015.11.100.

[42] L.O. Valøen, J.N. Reimers, Transport Properties of LiPF[sub 6]-Based Li-Ion Battery Electrolytes, J. Electrochem. Soc. 152 (2005) A882. doi:10.1149/1.1872737.

[43] P. Peng, F. Jiang, Thermal behavior analyses of stacked prismatic LiCoO2 lithium-ion batteries during oven tests, Int. J. Heat Mass Transf. 88 (2015) 411–423. doi:10.1016/j.ijheatmasstransfer.2015.04.101.

[44] J. Li, Y. Cheng, M. Jia, Y. Tang, Y. Lin, Z. Zhang, Y. Liu, An electrochemical-thermal model based on dynamic responses for lithium iron phosphate battery, J. Power Sources. 255 (2014) 130–143. doi:10.1016/j.jpowsour.2014.01.007.

[45] Y. Tang, M. Jia, J. Li, Y. Lai, Y. Cheng, Y. Liu, Numerical Analysis of

Distribution and Evolution of Reaction Current Density in Discharge Process of Lithium-Ion Power Battery, J. Electrochem. Soc. 161 (2014) E3021–E3027. doi:10.1149/2.004408jes.

[46] R. Zhao, J. Gu, J. Liu, An investigation on the significance of reversible heat to the thermal behavior of lithium ion battery through simulations, J. Power Sources. 266 (2014) 422–432. doi:10.1016/j.jpowsour.2014.05.034.

[47] A. a. Pesaran, Battery thermal models for hybrid vehicle simulations, J. Power Sources. 110 (2002) 377–382. doi:10.1016/S0378-7753(02)00200-8.

[48] P. Taheri, A. Mansouri, M. Yazdanpour, M. Bahrami, Theoretical Analysis of Potential and Current Distributions in Planar Electrodes of Lithium-ion Batteries, Electrochim. Acta. 133 (2014) 197–208. doi:10.1016/j.electacta.2014.04.040.

[49] N. Javani, I. Dincer, G.F. Naterer, B.S. Yilbas, Heat transfer and thermal management with PCMs in a Li-ion battery cell for electric vehicles, Int. J. Heat Mass Transf. 72 (2014) 690–703. doi:10.1016/j.ijheatmasstransfer.2013.12.076.

[50] G. Karimi, X. Li, Thermal management of lithium-ion batteries for electric vehicles, (2013) 13–24. doi:10.1002/er.

[51] J. Xun, R. Liu, K. Jiao, Numerical and analytical modeling of lithium ion battery thermal behaviors with different cooling designs, J. Power Sources. 233 (2013) 47–61. doi:10.1016/j.jpowsour.2013.01.095.

[52] H. Park, A design of air flow configuration for cooling lithium ion battery in hybrid electric vehicles, J. Power Sources. 239 (2013) 30–36. doi:10.1016/j.jpowsour.2013.03.102.

Chapter 4 Electrochemical-thermal Modeling to Evaluate Active Thermal Management of a Lithium-ion Battery Module

4.1. Introduction

Lithium-ion (Li-ion) batteries are considered as suitable energy storage devices for the electric vehicles (HEV-EV) due to their high specific energy and power densities [1, 2] and low self-discharge rate [3]. The main challenges to the wide employment of Li-ion batteries in EV and HEV are safety and cost related to the battery lifespan [4]. These challenges are strongly coupled to the thermal behavior of batteries. One of the most catastrophic safety issues of a lithium-ion battery is cascading thermal runaway, where multiple cells in a battery fail due to an individual cell failure. The conductivity of the electrolyte increases with temperature, causing more current to be directed to hotter sections of a battery. This generates more heat in hotter region, raising the temperature and allowing even more current to pass through it. This positive feedback has the potential to lead to the battery thermal runaway [5]. Another concern is temperature non-uniformity in the battery module and pack. The temperature difference in a module causes electrical imbalance over time which leads to the state of charge (SOC) mismatch between the cells. Hence, it is critical to retain the li-ion batteries maximum temperature within the safe limits and reduce the temperature non-uniformity of the battery and the module.

There are two major strategies for thermal management in electric vehicles. An active method by using air or a liquid as coolant [6, 7] or a passive approach by employing phase change materials (PCM) [8, 9]. Air cooling can moderate the batteries temperature rise, but in aggressive driving cycles and/or at high operating temperatures it will result in a large non-uniform temperature distribution in the battery module [10]. Liquid cooling with water, oil or refrigerants as the heat transfer medium shows higher thermal efficiency due to the higher heat capacity of liquids compared to air [11].

A number of numerical investigations have been performed on the liquid cooling of Li-ion batteries. Karimi and Li [6] simulated the effects of various cooling scenarios on the temperature and voltage distribution using an empirical lumped battery thermal model. They showed that a cooling strategy based on distributed air or liquid convection can be an efficient and cost-effective method. Yeow et. al. [13,14] utilized uniform thermophysical properties and equivalent circuit heat generation model to compare single and dual cold plate cooling systems. Their studies showed that the dual cold plate design presents considerably higher cooling capacity than single cold plate design. Xun et. al. [15] developed numerical and analytical models based on an empirical lumped battery thermal model to study the effects of cooling channel and battery stack geometries on the battery thermal management system (BTMS). They suggested that a counter-flow arrangement of the cooling channels or periodic changing of the coolant flow direction

may improve the BTMS performance. Liu et. al. [16] compared the temperature distribution in a Li-ion battery stack with liquid and PCM thermal management. Simulations were performed on a 20Ah flat battery stack utilizing a lumped thermal model. The results indicated that the liquid cooling is generally more efficient than the PCM method, although PCM caused more uniform temperature distribution. Tong et. al. [7] numerically studied the effects of operating and design parameters of a liquid cooling system on the performance of a battery pack. They calculated the battery heat generation through a 2-dimensional coupled thermal-electrochemical model. The results indicated that the rise in the average temperature and the temperature distribution non-uniformity were intensified as the number of batteries in the pack increased. Furthermore, it has been shown that increasing the coolant velocity or the cooling plate thickness can reduce the battery pack average temperature and decrease the non-uniformity of local temperature distribution. Chen et. al. [17] compared four air and liquid cooling systems with different designs. They used a 1RC equivalent circuit model with lumped thermal properties to estimate battery thermal behavior under constant current discharge. The results showed that an indirect cooling system was more practical than direct approach large-format Li-ion battery cooling.

Thermal management investigations in the module and pack levels are mainly conducted either by lumped thermal models with heat generation data obtained from experiments and equivalent circuit models or by 2D electrochemical-thermal models. This is due to the significant computational cost required for 3D coupled electrochemical-thermal models. However, accurate assessment of battery electrical and thermal responses to different cooling scenarios needs 3D coupled electrochemical-thermal models. The numerical studies on the liquid BTMS are commonly performed during constant current discharge cycles. Nevertheless, electric and hybrid electric vehicles driving cycles, and consequently batteries charge/discharge cycles, show complex patterns that cannot be precisely modeled with constant current discharge rates.

In this study, a three dimensional coupled electrochemical-thermal model for an NCA Li-ion battery as well as experimental validation of the electrical and thermal results are presented. The effects of cooling system design parameters and coolant inlet velocity on the electrical and thermal behavior of a lithium ion battery module during a standard hybrid electric vehicle driving cycle are investigated comprehensively.

Nomenclature

c_s	concentration of lithium in the active material particles (mol m^{-3})
c_l	electrolyte concentration (mol m^{-3})
C_p	Specific heat capacity (J kg^{-1} K^{-1})
D_s	diffusion coefficient of lithium in the active material (m2 s^{-1})

D_l	diffusion coefficient of electrolyte (m2 s^{-1})
E_{aD}	diffusion activation energy (kJ mol^{-1})
E_{aR}	reaction activation energy (kJ mol^{-1})
$f_\pm$	average molar activity coefficient
F	Faraday's constant (C mol^{-1})
j_0	exchange current density (A m^{-2})
j_n	local charge transfer current density (A m^{-2})
k_0	reaction rate constant (m$^{2.5}$ mol$^{-0.5}$ s^{-1})
k	thermal conductivity (W m^{-1} K^{-1})
L	thickness of each battery component (m)
P	coolant pressure (Pa)
$\dot{Q}$	coolant volume flow rate (m^3 s^{-1})
R	gas constant, 8.314 (J mol^{-2} K^{-1})
r	radius distance variable of electrode particles (m)
r_0	radius of electrode particles (m)
S_a	specific surface area (m^{-1})
t	time (s)
t_+	transferring number of Li$^+$
T	temperature (K)
T_a	ambient temperature (K)
U_{eq}	open circuit potential of the electrode (V)
$U_{eq,ref}$	open circuit potential under the reference temperature (V)
V	coolant velocity (m s^{-1})
Greek letters	
α_a	anode transfer coefficient
α_c	cathode transfer coefficient
γ	Bruggeman tortuosity exponent
ε_s	active material volume fraction
ε_l	electrolyte volume fraction
δ	active material thickness (m)
η	local surface overpotential (V)
θ	dimensionless battery volume
ρ	density (kg m^{-3})
σ_s	electronic conductivity in solid phase material (S m^{-1})
σ_l	ionic conductivity of electrolyte (S m^{-1})
Φ_s	solid phase potential (V)
Φ_l	electrolyte phase potential (V)
ψ	dimensionless module volume

Subscripts and superscripts	
0	initial or equilibrated value
ave	average
eff	effective value
max	maximum
l	electrolyte phase
s	solid phase
w	water

4.2. Numerical Model

4.2.1 Battery Modeling

In the current work, a fast simulation pseudo three dimensional electrochemical-thermal model is used. The numerical results are compared with a commercial 4Ah Li-ion battery with graphite anode coated on a copper foil (as the negative current collector) and NCA cathode material coated on an aluminum foil. The battery consists of 20 parallel connected cells with double-side coated current collectors, and a highly porous polymeric separator. The cell dimensions are about 8×46×138 mm. The model is based on the coupling of mass, charge, and energy conservations, as well as electrochemical kinetics. Fig. 4-1 represents the 1D and 3D computational domains and how they are coupled to form the pseudo 3D model. The current model uses a 1D local electrochemical cell unit to find the reaction and polarization heat generations as well as the electrolyte concentration distribution in the active battery material. The values of concentration are inserted in a 3D electric current conservation solver to calculate the distributed Ohmic heat generation. Finally, the 3D energy conservation equation is solved to find the temperature distribution considering three heat generation contributions from anode, cathode and the electrolyte phases. This coupling approach between electrochemical and thermal solvers lowers the computational time required and leads to a streamlined pseudo 3D model suitable for the assessment of electric vehicles thermal management systems.
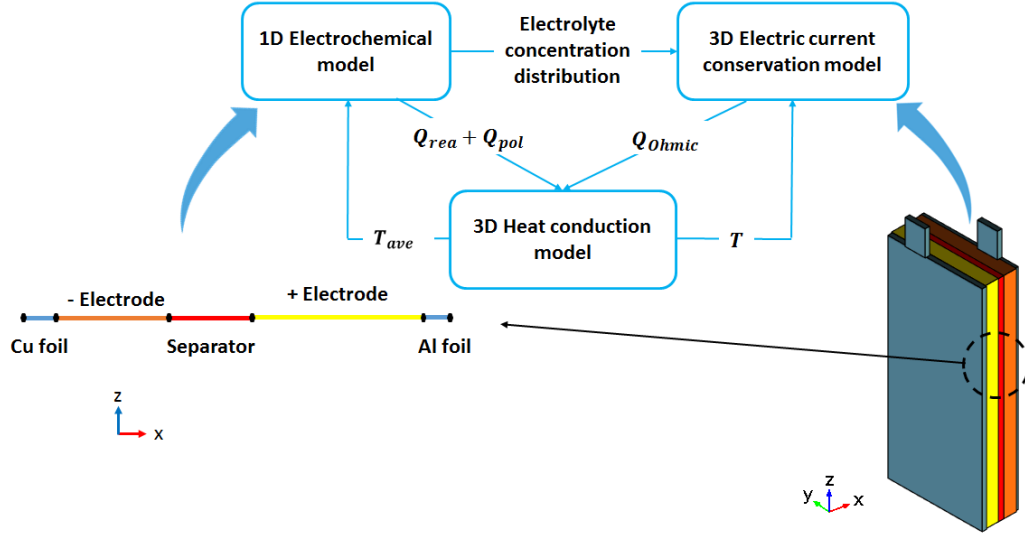
Figure 4-1. Schematic of the pseudo 3D model for a single cell

The 1D electrochemical model is based on the porous electrode theory, Ohm's law, mass transfer in the solid and electrolyte phase and concentrated solution theory for spherical active material particles [18]. Table 4-1 presents the governing equations and boundary conditions used to establish the coupled electrochemical-thermal model. The battery geometrical and design parameters, as well as kinetic, transport and thermal properties are listed in Table 4-2 [18-20]. The open circuit voltage (OCV) and voltage-temperature coefficient of porous electrodes are found from data plotted in Fig. 4-2 (a) and (b) [18-20].

Table 4-1. Governing equations and boundary conditions used in the battery electrochemical-thermal model [18, 19]

Physics	Governing Equation and Boundary Conditions
mass balance in liquid phase	$$\varepsilon_l \frac{\partial c_l}{\partial t} + \nabla \cdot (-D_l^{eff} \nabla c_l + \frac{i_l t_+}{F}) = \frac{S_a j_n}{F}$$ $$D_l^{eff} = D_l \varepsilon_l^{\gamma_l}$$
mass balance in solid phase for spherical active material	$$\frac{\partial c_s}{\partial t} - \frac{1}{r^2} \frac{\partial}{\partial r} \left(r^2 D_s \frac{\partial c_s}{\partial r} \right) = 0$$ $$\frac{\partial c_s}{\partial r} = 0 \ at \ r = 0$$
ionic transport in liquid phase	$$i_l = -\sigma_l^{eff} \nabla \Phi_l + \frac{2RT\sigma_l^{eff}}{F} \left(1 + \frac{\partial lnf_\pm}{\partial lnc_l} \right) \left(1 - t_+ \right) \nabla (lnc_l)$$ $$\sigma_l^{eff} = \sigma_l \varepsilon_l^{\gamma_l}$$ $$\frac{\partial c_l}{\partial x} = 0 \ at \ x = L_{NCC} \ and \ x = L_{NCC} + L_N + L_s + L_P$$

electron transport in solid phase	$\nabla.i_s + \nabla.i_l = 0$
	$\nabla.i_s = -S_a j_n$
	$i_s = -\sigma_s^{eff} \nabla\Phi_s$
	$\sigma_s^{eff} = \sigma_s \varepsilon_s^{\gamma_l}$
	$-\sigma_s^{eff}\nabla\Phi_s = 0$ at $x = L_{NCC} + L_N$ and $x = L_{NCC} + L_N + L_s$
Electrochemical kinetics	$j_n = j_0 \left\{ exp(\dfrac{\alpha_a F}{RT}\eta) - exp(-\dfrac{\alpha_c F}{RT}\eta) \right\}$
	$j_0 = F k_0 c_l^{\alpha_a} (c_{s,max} - c_{s,surf})^{\alpha_a} c_{s,surf}^{\alpha_c}$
	$\eta = \Phi_s - \Phi_l - U_{eq}$
	$U_{eq} = U_{eq,ref} + \dfrac{\partial U_{eq}}{\partial T}\left(T - T_{ref}\right), T_{ref} = 293.15\ K$

In order to demonstrate the validity of the electrical and thermal aspects of the pseudo 3D battery modeling procedure the calculated values of surface temperature and OCV are compared with experimentally measured ones. A photograph of the experimental setup is shown in Fig. 4-3. Thermal imaging is conducted to record the temperature distribution on the battery surface utilizing an infrared (IR) camera. The camera resolution is 640×480 pixels and exhibits an accuracy of ±0.01 K. The battery cover is made of polished Aluminum with an emissivity factor of 0.05 [21]. During the experiments, the battery is mounted inside a constant temperature chamber to ensure uniform natural convection heat transfer from all sides. Furthermore, an aluminum dummy with an identical geometry of the test battery is used to determine the natural convection heat transfer coefficient inside the chamber. An average value of h=6.5±0.1W/m2K is found for the convective heat transfer coefficient and is used in the numerical simulations in this section.
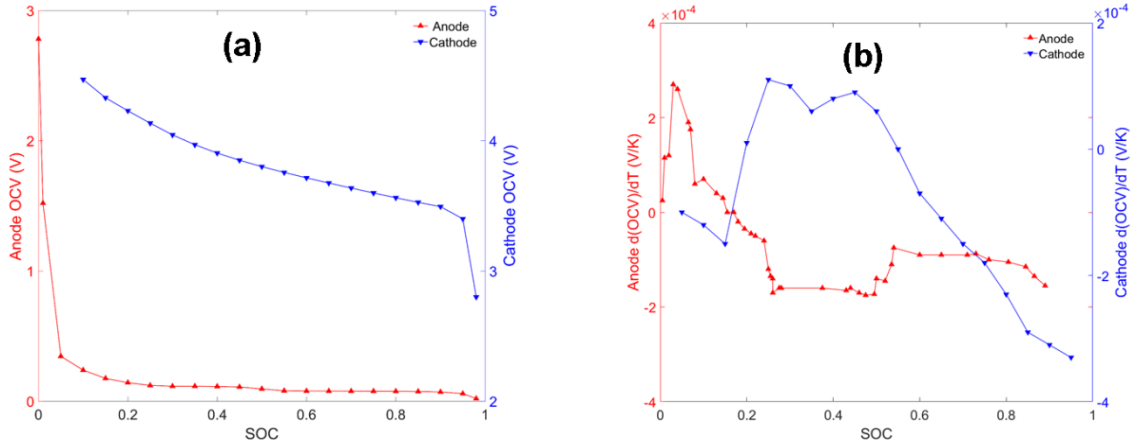
Figure 4-2. (a) Open circuit voltage, and (b) voltage-temperature coefficient variation of anode and cathode materials with SOC

Table 4-2. . Parameters used in the battery electrochemical-thermal model [18-20]

Parameter (unit)	Al CC	Cathode	Electrolyte	Anode	Cu CC
c_0 (mol/m^3)	-	33956	1000	31507	-
c_p (kJ$/$kgK)	900	1250	1518	1437	385
D (m^2/s)	-	1.5E-15	*	**	-
E_{aD} (kJ/mol)	-	18	-	4	-
E_{aR} (kJ/mol)	-	3	-	4	-
F (C/mol)	-	-	96487.332	-	-
k (W/mK)	160	1.38	0.099	1.04	400
k_0 (m$^{2.5}$mol$^{-0.5}$/s)	-	3.255E-11	-	1.764E-11	-
r_0 (μm)	-	1.2	-	14.75	-
t_+	-	-	0.363	-	-
α_a, α_c	-	0.5	-	0.5	-
δ(μm)	23	46	26	48	16
ε	-	0.423	0.4	0.56	-
ρ (kg/m^3)	2700	4740	1210	5031	8960
σ (S/m)	3.8E7	91	***	100	6.3E7

Figure 4-3. Photograph of the experimental setup to perform thermal imaging on the cell. The constant temperature chamber interior walls are covered with paper towel to avoid reflections.

4.2.2. Liquid cooling system model

Water is considered as the coolant and the flow is assumed to be laminar due to the low flow velocity and short characteristic lengths in this study. The temperature dependent properties of the coolant are listed in Table 4-3 [22].

Table 4-3. Temperature dependent properties of the coolant [24]

Thermophysical property	Value
Heat capacity (J/kg.K)	$12010.1471 - 80.4072879 \times T + 0.309866854 \times T^2$ $- 5.38186884e - 4 \times T^3 + 3.62536437e - 7 \times T^4$
Dynamic viscosity (Pa.s)	$1.3799566804 - 0.021224019151 \times T + 1.3604562827e - 4$ $\times T^2 - 4.6454090319e - 7 \times T^3$ $+ 8.9042735735e - 10 \times T^4 - 9.0790692686e$ $- 13 \times T^5 + 3.8457331488e - 16 \times T^6$
Density (kg/m^3)	$838.466135 + 1.40050603 \times T - 0.0030112376 \times T^2$ $+ 3.71822313e - 7 \times T^3$
Thermal conductivity (W/m.K)	$-0.869083936 + 0.00894880345 \times T - 1.58366345E - 5 \times T^2$ $+ 7.97543259E - 9 \times T^3$

4.2 3. Conservation Equations

The mass conservation equation of water in the cooling channel is:

$$\frac{\partial \rho_w}{\partial t} + \nabla . \left(\rho_w \vec{V} \right) = 0 \tag{4.1}$$

where ρ_w is the density of water and $\vec{V}$ is the velocity vector of water in the cooling channel. The momentum conservation equation of the coolant is as follow:

$$\rho_w \frac{\partial}{\partial t} \left(\vec{V} \right) + \rho_w \left(\vec{V} \nabla \right) \vec{V} + \nabla p - \mu \nabla^2 \vec{V} = 0 \tag{4.2}$$

where p is the static pressure. The energy conservation equation for water is:

$$\frac{\partial}{\partial t} \left(\rho_w C_{p_w} T_w \right) + \nabla . \left(\rho_w C_{p_w} \vec{V} T_w \right) - \nabla . (k_w \nabla T_w) = 0 \tag{4.3}$$

where T_w is the temperature of water, and k_w and C_{p_w} are the thermal conductivity and specific heat of water, respectively.

4.2.4. Initial and Boundary Conditions

The initial temperature for both batteries and water in all simulations is 293.15K. Velocity and pressure boundary conditions are used for the coolant at inlet and outlet

boundaries, respectively. In order to provide a framework for comparing various cooling scenarios, heat insulation boundary condition is defined at all external boundaries of the cooling channel(s) and batteries. This boundary condition is reasonable because in HEV the battery module is covered by protecting materials for safety, resulting in a considerable thermal resistance.

4.2.5. Numerical procedure
All equations are solved in COMSOL Multiphysics 5.2 using the Finite Elements Method (FEM). The accuracy of the calculation and computational time strongly depend on the mesh and solver due to the high nonlinearity of the governing equations and different geometrical scales in the model. A free triangular mesh is used at the boundaries along with the swept method. Several mesh densities are tested to ensure the mesh independency of the solutions. In order to save memory and time, the governing equations are coupled by using a segregated approach. At each time step, two segregated steps are considered: first, the temperature distribution is obtained by keeping the electrochemical variables of all 1D electrochemical cells constant; and second, the results of temperature distribution at each mesh node are utilized to update the local electrochemical and thermal parameters in 1D and 3D solvers. For each time step, the maximum relative tolerance for all variables is 0.00001. The computations are performed on a workstation with a 2.0 GHz eight core processor and 64 GB random access memory.

4.2.6. Battery Module Cooling System Configuration and Modeling
Many auto manufacturers limit the capacity of Li-ion batteries to 5Ah to extend their lifespan. For instance, Honda Insight Hybrid uses 4Ah batteries and Honda Accord and New NSX utilize 5Ah Li-ion batteries. In this section, the pseudo 3D model described above is adapted for a 5Ah NCA battery. The basic parameters of the battery used in the module simulations are listed in Table 4-4. The characteristics of this battery that are not presented in this table are identical to values listed in table 2. A 1.3kWh battery pack consisted of 12 modules is considered. Each module contains six 5Ah Li-ion batteries in parallel.

Table 4-4. Specifications of the battery used in the module simulations

Parameter	Value
Width (mm)	80
Height (mm)	110
Thickness (mm)	9
Capacity (Ah)	5
Tab dimensions (mm)	15×10×0.5 (w×h×t)

Liquid cooling methods can be divided into direct and indirect designs. In direct liquid cooling, the coolant flows through a gap between two adjacent batteries and contacts the

cell surfaces directly. In the indirect approach, battery heat generation conducts from its surfaces to the cooling plates. The cooling plates are in thermal contact with the cooling channel(s). Although direct cooling may present more heat dissipation, it needs a more complex coolant circulation system and is more likely to encounter the liquid leakage problem. Indirect cooling is widely implemented in the current HEV [22, 23] and is investigated in this study.

Fig. 4-4 indicates the schematic of two liquid cooling designs examined in this study. Both methods use thin aluminum cooling plates to enhance the temperature uniformity in the module. Fig. 4-4 (a) shows the indirect cooling from the bottom of the batteries. Cooling from the small surface at the bottom of the batteries results in temperature non-uniformities since the maximum temperature happens close to the tabs at the top of the batteries. However, the simplicity of this design offers advantages such as the small space requirements, simple coolant circulation and providing structural support to the batteries. Fig. 4-4 (b) indicates an alternative to cooling from the bottom by employing two cooling channels. The second channel adds some weight and volume to the battery module, however, the temperature non-uniformity in the batteries is expected to decrease since the coolant enters from the top of the module. In this approach, cooling plates are used between adjacent cells to improve heat conduction from the batteries to the coolant. Table 4-5 shows the design parameters of the cooling systems. In this study, both cooling designs are numerically modeled by a half of the module with symmetry boundaries on the outer side of one of the cooling plates.
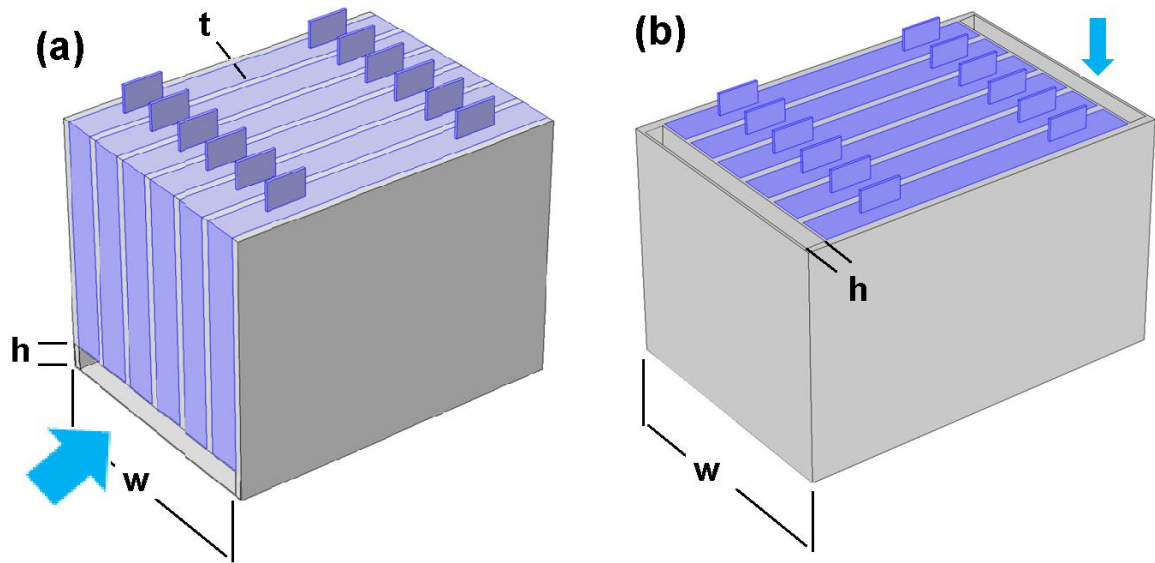
Figure 4-4. Schematic of (a) single channel, and (b) double channel cooling systems and coolant flow direction

Table 4-5. Geometrical design parameters of cooling systems

Parameter	Value
Cooling channel height (mm), h	6
Cooling plate thickness (mm), t	1, 2, 3, 4, 5
Cooling channel width (mm), w	485, 492, 499, 506, 513
Coolant inlet temperature (K)	293.15

4.3. Results and Discussion

4.3.1. Battery model results

The experimental and simulated results of open circuit voltage and temperature increase are shown in figures 4-5 and 4-6, respectively. Fig. 4-5 shows the battery open circuit voltage under 0.5C, 1C discharge rates. Generally, the simulation results agree well with the experimental data well. The normalized root mean square difference (RMDS) error for the experimental and numerical OCV is 3.4% and 3.6% for 0.5C and 1C discharge rates, respectively. The differences between numerical and experimental values are mainly due to the empirical data used in the simulations. The anode and cathode OCV data (shown in Fig. 4-2 (a)) are not measured values from the battery under study, but they are obtained from the literature [18-20]. The values of measured and calculated

average surface temperature rise are compared in Fig. 4-6 under 1C and 4C discharge rates. The discrepancy between measured and predicted values is more considerable at the end of 4C discharge rate due to higher Ohmic heat generation penetration from the contact resistance at tabs into the active battery material.
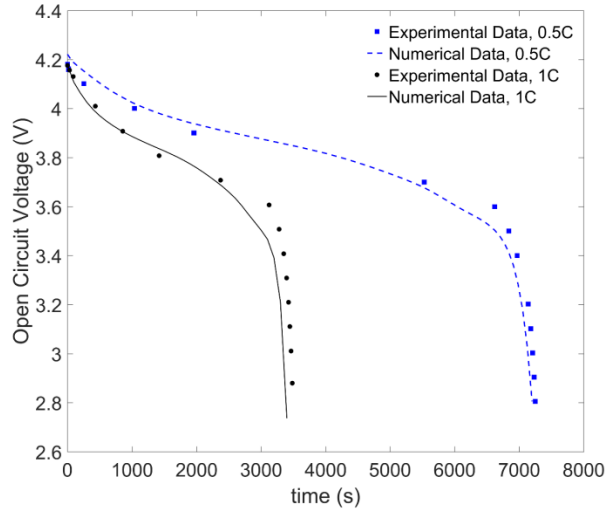
Figure 4-5. Open circuit voltage comparison of the simulation and experimental results
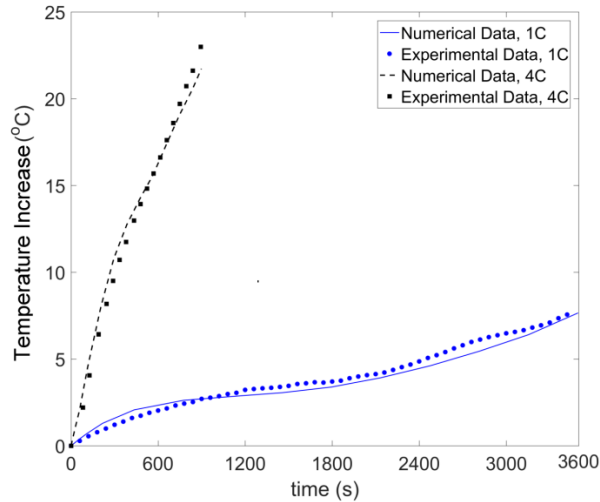
Figure 4-6. Comparison of simulated results of average surface temperature with experimental data

Fig. 4-7 compares the simulated temperature distribution and the results from infrared thermography under 4C discharge rate. As shown in this figure, the average surface temperature is slightly lower and it is more uniformly distributed in the simulations.

These differences between the IR imaging and numerical results can be explained by various factors. Although a silver epoxy has been used to minimize the resistance between the load cables and the battery tabs, a small electrical contact resistance is unavoidable. As a result, a part of the heat generated at the tabs conducts to the battery material resulting in a higher and more non-uniform temperature distribution. The simulations are based on an ideal battery with uniform active material distribution. However, it is difficult to attain an ideal distribution of active materials because of the manufacturing limits. Furthermore, a uniform electrochemical reaction assumption is used in the pseudo 3D model. This leads to an underestimation and overestimation of the total heat generation in low and high temperature regions, respectively. This is because the Ohmic heat generation increases with temperature in Li-ion batteries [25]. Based on the values presented in Fig. 4-5 and 4-6 the OCV, average temperature rise, and temperature distribution of the simulation are in good agreement with the experimental data, demonstrating that the model is capable to simulate the real battery under experiment.
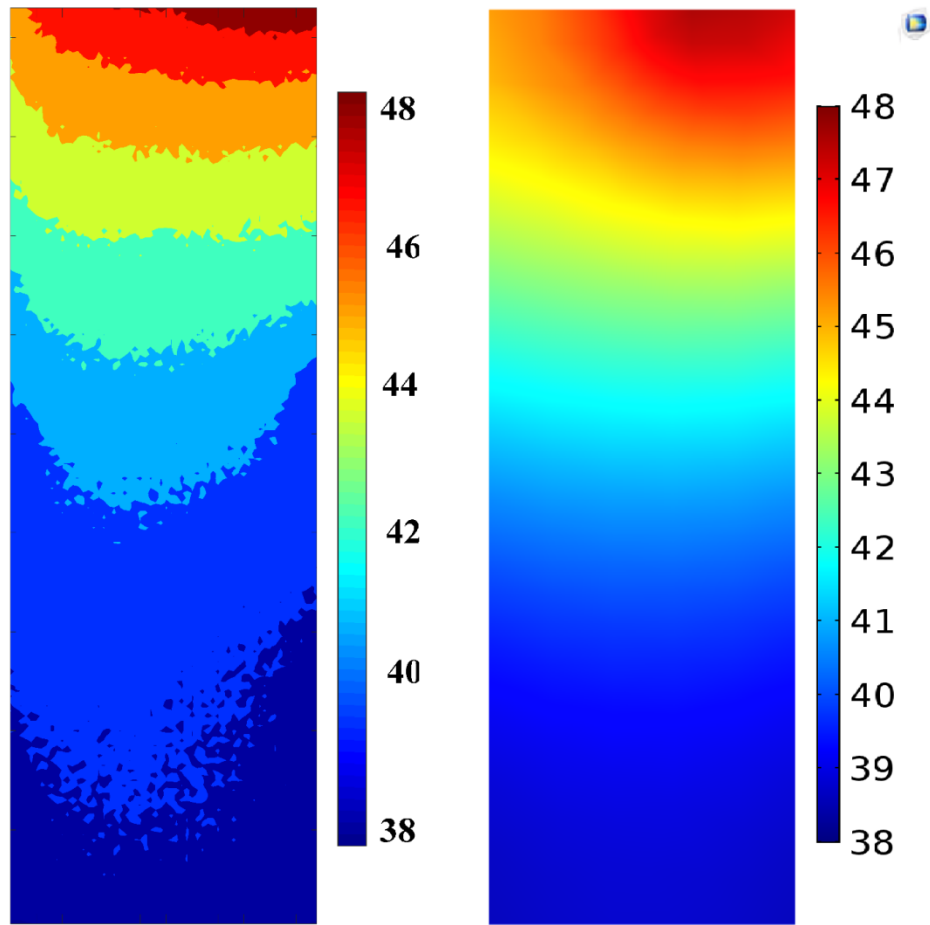
Figure 4-7. Comparison of experimental (left) and numerical (right) battery surface temperature distributions under 4C discharge rate at SOC=30%

4.3.2. Liquid cooling system

In this section, the simulations are carried out under HEV federal urban driving cycle (FUDC) [26]. The FUDC is implemented to the described battery pack to find the variation of batteries' C-rate with time. The pseudo 3D battery model is employed into each cooling system to evaluate their impact on the battery module performance under the driving cycle. In particular, the effects of the coolant inlet velocity and the thickness of cooling plates on the average and local module temperature are explored.

In this study, an initial value of SOC=70% is used in all simulations [26, 27]. Fig. 4-8 shows the variation of a battery loading current and OCV during the driving cycle. High charge and discharge currents, as shown in Fig. 4-8, generate a considerable amount of heat in the batteries.
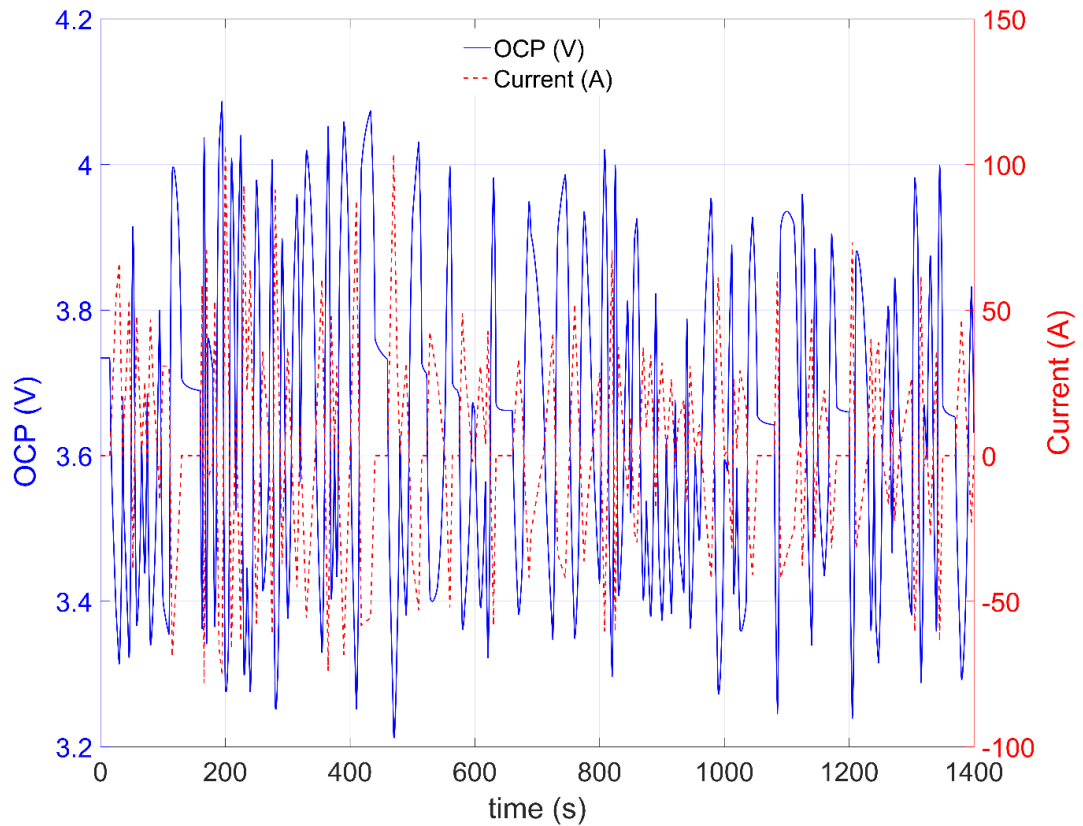
Figure 4-8. Variation of a battery loading current and OCV during the FUDC driving cycle

Fig. 4-9 represents the variation of instantaneous and cumulative heat generation of a battery in the module with time. As can be seen from this figure, Ohmic heat generation is the dominant heat generation mechanism during the driving cycle. The Ohmic heat

generation is quadratic dependent on current and hence, generates the major part of total heat generation under the high charge and discharge currents during the driving cycle.
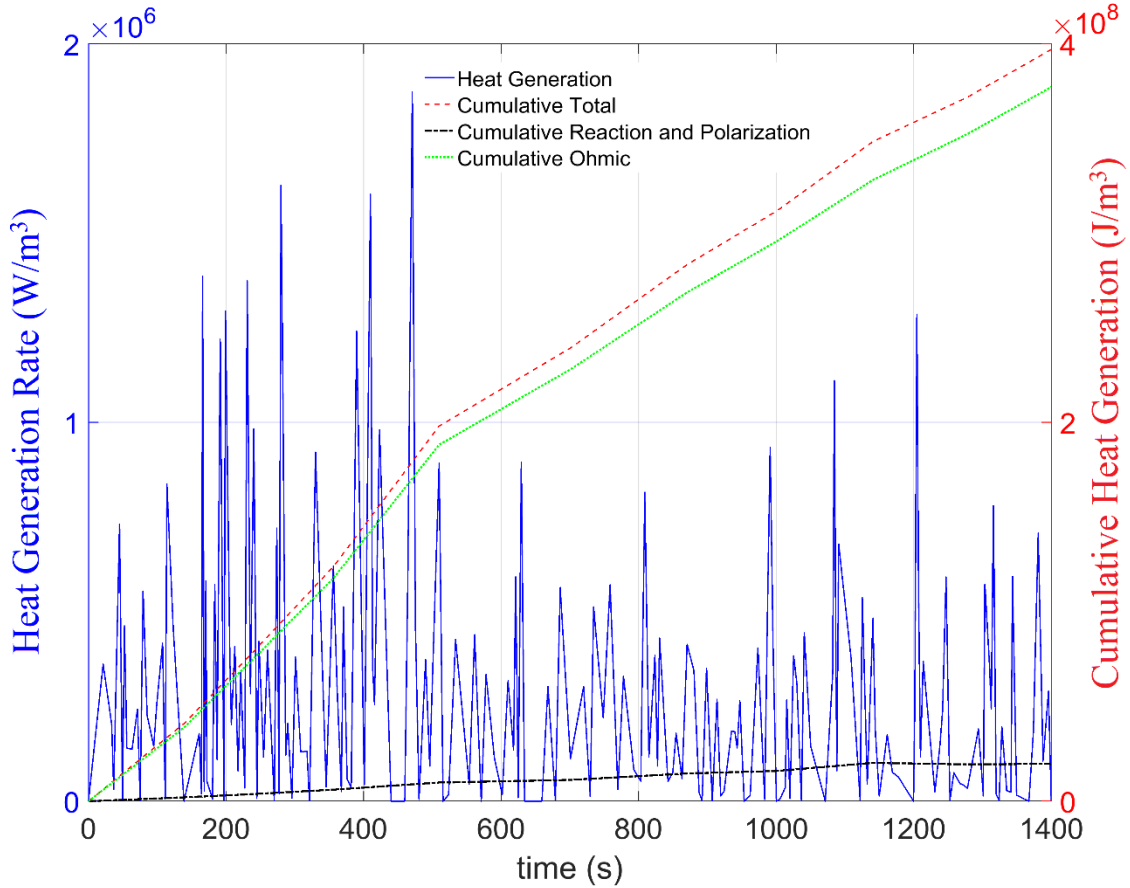
Figure 4-9. Variation of instantaneous and cumulative heat generations in a battery during the driving cycle

The capacity fading rate of Li-ion battery increases significantly when the operating temperature increments. For NCA batteries an upper limit of the average temperature of around 333K can be considered. Fig. 4-10 shows the battery average temperature variation with no heat removal, resembling an insulated battery module. As shown in Fig. 4-10, the battery temperature reaches the upper limit value of 333K after about 340 seconds which implies the necessity of a thermal management system to maintain the battery temperature within the safe limit.
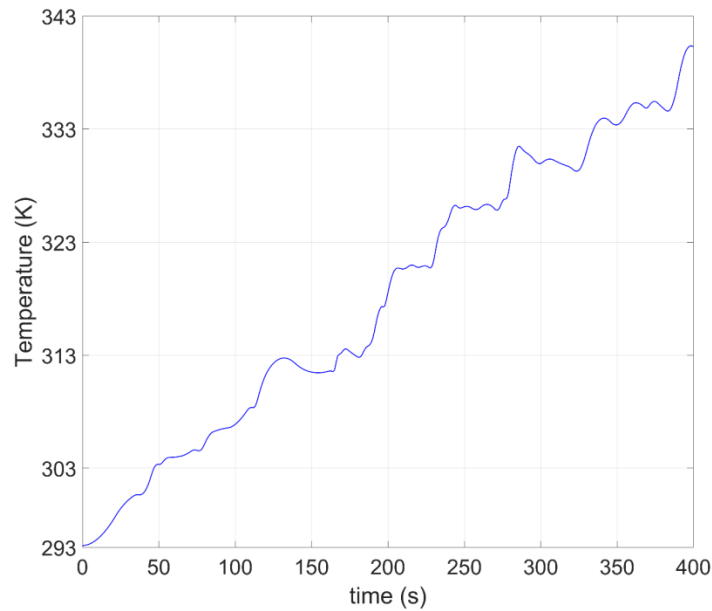
Figure 4-10. Battery average temperature variation with time under thermal insolation

4.3.3. Effects of Reynolds Number

A series of simulations is conducted to assess the effects of Reynolds number on the thermal performance of BTMS. The values of inlet flow velocity are set to keep the flow in the laminar region throughout the cooling channel(s) in all cases. The simulations have the same initial and inlet temperature (293.15k) and are conducted for a cooling plate thickness equal to 3mm.

Fig. 4-11 shows the variation of module average temperature (the average temperature of all three batteries) with time for both designs. As can be seen from this figure, the average temperature is higher in the single channel design for all Reynolds numbers investigated. Employing two cooling channels enhances the total heat dissipation from the module and reduces the average temperature by about 10K. The average temperature generally decreases with Reynolds number due to more heat removal by the coolant. However, the influence of Reynolds number is less significant at higher values. This is due to the dominant conductive thermal resistance between the cooling channel and cooling plates, as well as between the cooling plates and batteries.
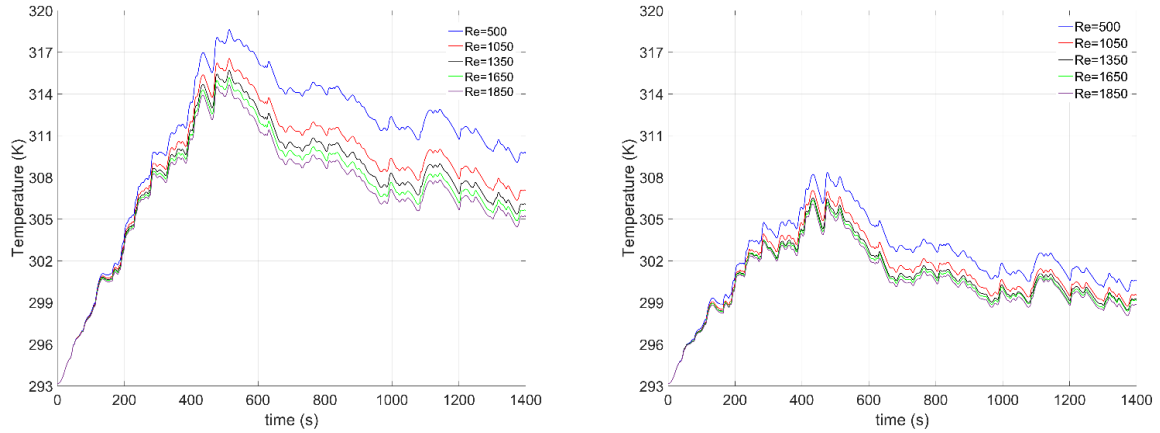
Figure 4-11. Variation of batteries average temperature under single channel (left) and double channel (right) cooling designs

Fig. 4-12 (a) and (b) depict the maximum temperature and the average temperature difference of the batteries at various Reynolds numbers. In Fig. 4-12, battery 1 represents the battery close to the module exterior wall and number 3 is the inner battery close to the symmetry boundary condition. The maximum temperature in figure 4-12 (a) is the highest battery temperature observed during the driving cycle. As Fig. 4-12 (a) shows, although both designs can keep the maximum temperature less than the upper limit of 333K, the maximum temperature in the double channel design is considerably lower as compared to single channel design due to more heat removal by the coolant.
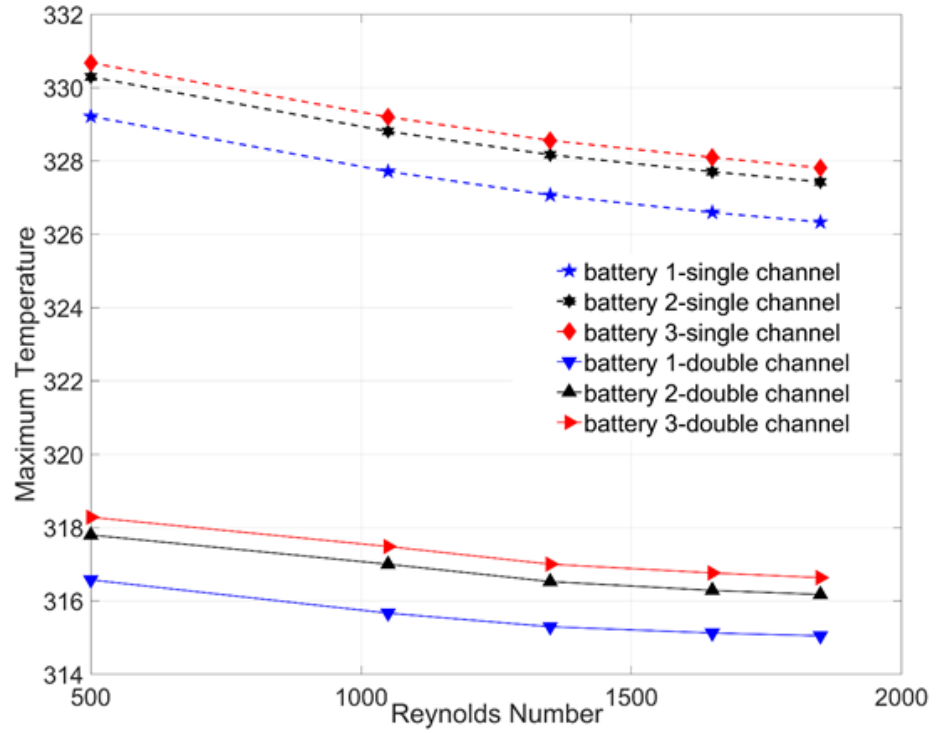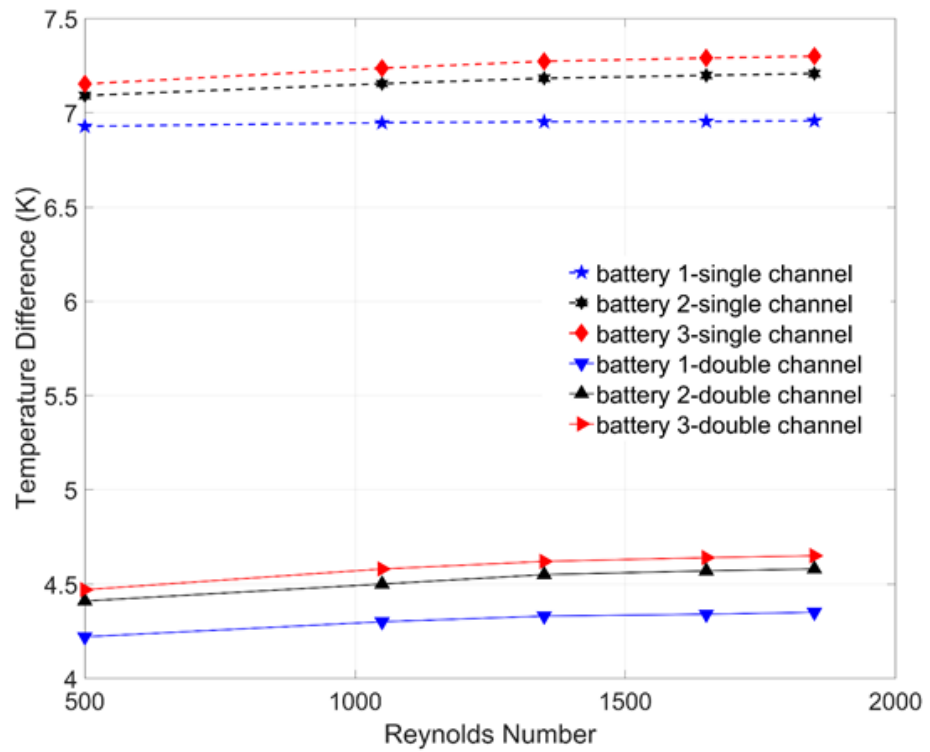
Figure 4-12. Variation of (a) batteries maximum temperature, and (b) average temperature difference with Reynolds number

Among the main factors influencing the aging of Li-ion batteries is the temperature gradient. The time average of the temperature difference is of interest because of multiple repetitions of the drive cycle in HEV. The average temperature difference shown in Fig. 4-12 (b) is the time average of the temperature difference in each battery as follow:

$$\Delta T_i = \frac{1}{t_{cycle}} \int_{t=0}^{t_{cycle}} \left(T_{max(t),i} - T_{ave(t),i} \right) dt \qquad 0 < t < 1400 \qquad (4.4)$$

where i=1, 2, 3 represents each battery in the simulated module, and t_{cycle} is the driving cycle duration (1400 s).

The difference between the maximum and average temperatures is an index for the heat accumulation in a battery. As Fig. 4-12 (b) suggests, the double channel design can maintain the temperature difference to values less than 5K for all batteries. In both designs, the temperature is more uniform in battery 1 compared to the other batteries in the module. The inner batteries are surrounded by two heat generation sources which result in more heat accumulation and consequently more temperature non-uniformity. The temperature difference slightly increases with Reynolds number in all cases. Increasing the Reynolds number enhances the heat transfer to the coolant and leads to low temperature regions close to the channel(s). However, the heat conduction from hot areas to the channel is not adequate due to the relatively low thermal conductivity of batteries. Therefore, the average temperature difference increases with the Reynolds number.

As shown in Fig. 4-12 (b) any attempt to enhance the thermal performance of BTMS by increasing Reynolds number may result in a more non-uniform temperature distribution. The main cause of temperature non-uniformity is the insufficient heat conduction in the module. Heat conduction can be improved by increasing the contact area between the cooling plates and the cooling channels. The effects of cooling plate thickness on the temperature distribution of module are discussed in the following section.

4.3.4. Effects of Cooling Plate Thickness
In addition to the coolant inlet velocity, another quantity of interest for evaluating the performance of the cooling systems is cooling plate thickness. Different values of cooling plate thickness between 0.001m to 0.005m are investigated. In this section, the Reynolds number in all cases is 1100. Any change in the thickness of plates will vary the cooling channel hydraulic diameter, and consequently, the Reynolds number. In order to evaluate the effect of cooling plate thickness, the inlet velocity is appropriately modified to keep the Reynolds number at constant value of 1100 in all cases.
Fig. 4-13 shows the variation of the module average temperature and coolant temperature rise with time for both designs. A trend similar to the effect of the Reynolds number is

observed. Increasing the coolant plate thickness decreases the average temperature. This is mainly due to the increased heat transfer area between the cooling channel and cooling plates which enhances heat rejection from batteries to the coolant. As can be seen from Fig. 4-13, the average temperature is higher in the single channel design compared to double channel design due to more heat removal in the latter case.
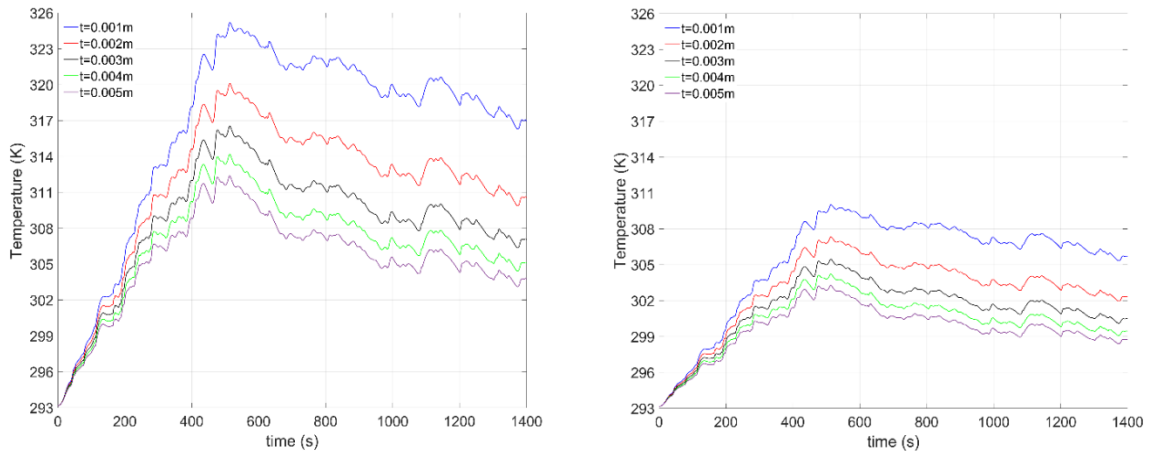
Figure 4-13. Variation of batteries average temperature under single channel (left) and double channel (right) cooling designs

Fig. 4-14 (a) and (b) depict the maximum temperature and the average temperature difference of the batteries at different cooling plate thicknesses. As can be seen from this figure, both maximum temperature and average temperature difference decrease with cooling plate thickness. This is due to more efficient heat conduction from the cooling plates to the coolant. As the thickness increases, the average temperature difference of single channel design appears to approach a limiting value. Conversely, in the case of double channel design, this parameter decreases almost linearly with thickness. As mentioned before, a thicker cooling plate enhances heat conduction in the module, however, utilizing a single cooling channel cannot provide an adequate cooling effect. Therefore, a further increase in cooling plate thickness does not efficiently reduce the temperature difference in the single channel design.
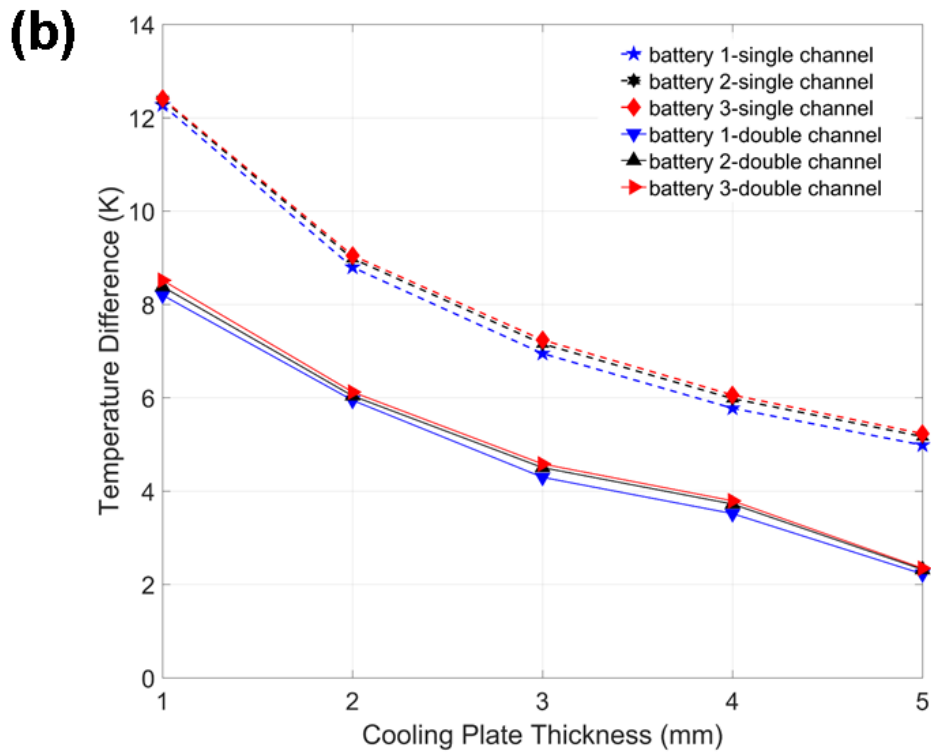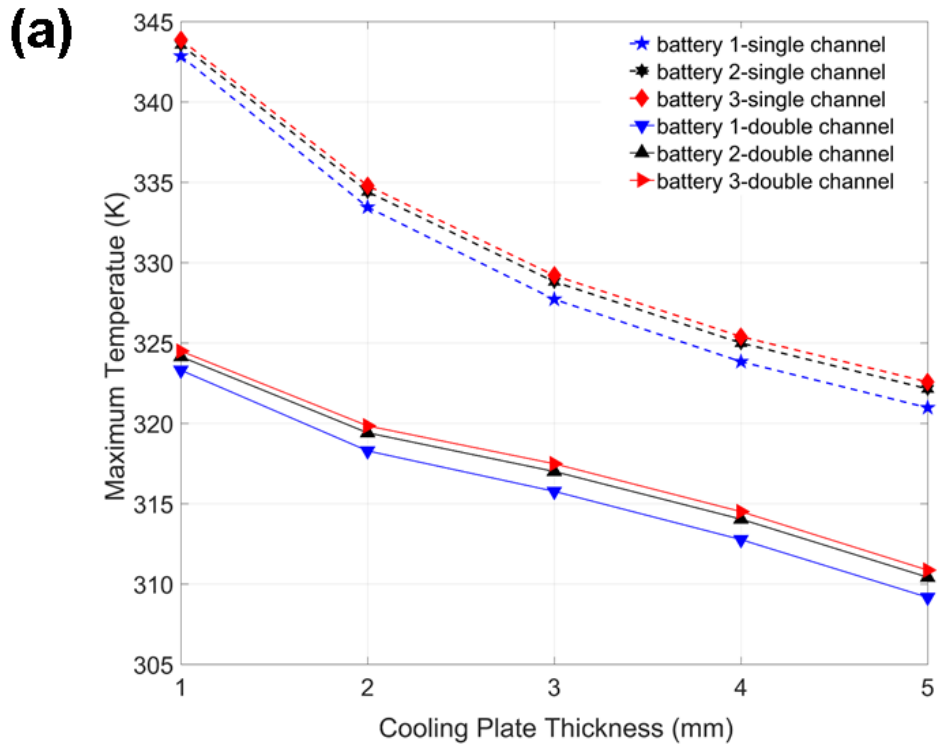
Figure 4-14. Variation of (a) batteries maximum temperature, and (b) of average temperature difference with cooling plates' thickness

The improved thermal performance of double channel design is only achievable at the expense of a higher volume required for the second cooling channel. In order to further investigate the effects of BTMS design parameters on the module temperature distribution, two dimensionless parameters are defined as follow:

$$\theta = \max(\frac{T_{max(t)} - T_{ave(t)}}{T_{ave(t)}})_i, \quad i = 1, 2, 3 \qquad 0 < t < 1400 \, s \tag{4.5}$$

$$\psi = \frac{\text{Volume of the module}}{\text{Volume of batteries in the module}} - 1 \tag{4.6}$$

θ represents the relative temperature non-uniformity caused by inadequate heat rejection form the batteries and Ψ indicates the module volume increase due to the utilization of the cooling system.

The 3D-surface plots in Fig. 4-15 exhibit the effects of Reynolds number and cooling system geometry on the dimensionless temperature difference, θ. As can be seen, the values of θ are generally smaller under the double channel design which suggests a more uniform temperature distribution. In both designs, the maximum θ occurs at the largest Reynolds number and smallest cooling plate thickness. As shown in Fig. 4-15, the temperature distribution is more sensitive on the thickness of the plates (Ψ). This implies that conduction in the BTMS is the dominant thermal resistance, and optimization attempts should mainly focus on enhancing conduction in the battery module. Furthermore, the volume increase in double channel design is slightly more than that in the single channel design (3~4%) due to a longer cooling channel and cooling plates required.
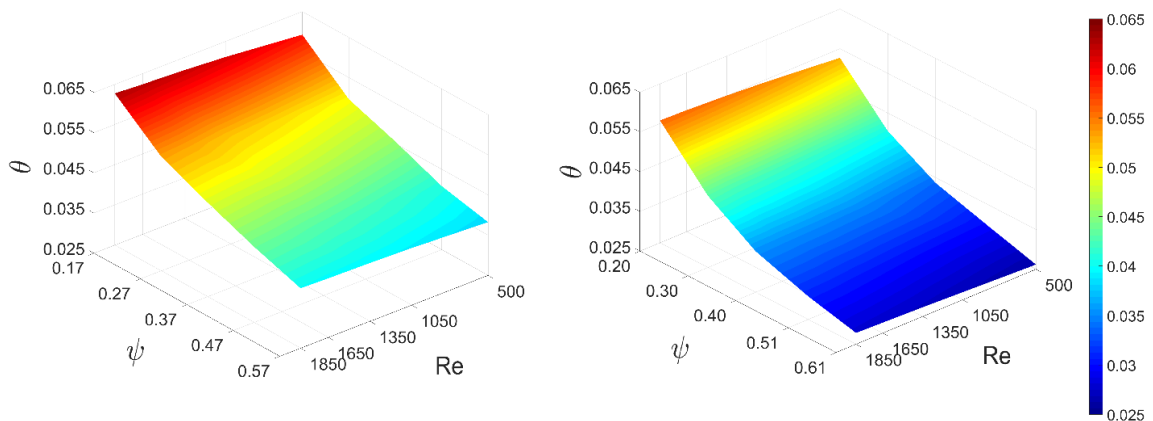
Figure 4-15. Dimensionless temperature difference (θ) in the module as a function of Re and Ψ under single channel (left) and double channel (right) designs

80

The pump energy consumption at different working conditions is presented in Table 4-6. In this table, the battery module energy generation is calculated as follow:

$$E = \sum_{i=1}^{i=n} \int_0^{t_{cycle}} I_i V_i dt \qquad (4.7)$$

where n is the number of batteries in the module (3 in the simulation model), and I_i and V_i represent the current and voltage of the ith battery in the module. The energy loss of the coolant through the cooling channel during a driving cycle is:

$$E_{loss} = \int_0^{t_{cycle}} (\Delta P \dot{Q}) dt \qquad (4.8)$$

where P_{drop} is the water pressure drop through the channel(s) and $\dot{Q}$ is the water volume flow rate.

Table 4-6. Pump energy consumption of as a fraction of total energy generation

Design	E_{loss}/E (minimum-maximum)
single channel	0.15%-0.8%
double channel	0.2%-1%

As can be seen from Table 4-6, coolant circuit pump consumes a very small fraction of total battery module energy generation which is consistent with values reported in references [17, 29]. Therefore pressure drop is not considered as a quantity of interest in this study and is not further investigated.

The module temperature distribution at the end of driving cycle is shown in Fig. 4-16. This figure illustrates the results of the limiting cases corresponding to the conditions where the values of θ are maximum and minimum (worst vs best case of temperature uniformity). The cooling plates and channels, as well as the battery tabs are not shown so that the temperature distribution along the battery thickness can be observed clearly.

In the single channel cooling, temperature increases from the bottom to the top and from the coolant inlet to the outlet. During the driving cycle more heat is generated in the aluminum tab (left tab in Fig. 4-16) because of its relatively smaller thermal and electrical conductivity compared to the negative tab which is made of copper. However,

81

the negative tab (right) is hotter due to coolant flow direction from left to right. The main drawback of single channel design, which is the high temperature gradient along the z-direction, can be observed in Fig. 4-16 (a) and (b). The batteries heat generation is maximum at the top due to a large current density at the areas close to the tabs as shown in Fig. 6. However, the heat generated is mainly removed from the bottom of the batteries resulting in a large temperature difference in the z-direction. Note that placing the top of cells in thermal contact with the cooling plate is not considered due to height tolerances caused by connecting cables and safety concerns. As shown in Fig. 16 (b), the temperature non-uniformity decreases due to the utilization of thicker plates which improves heat removal from the top of the batteries.
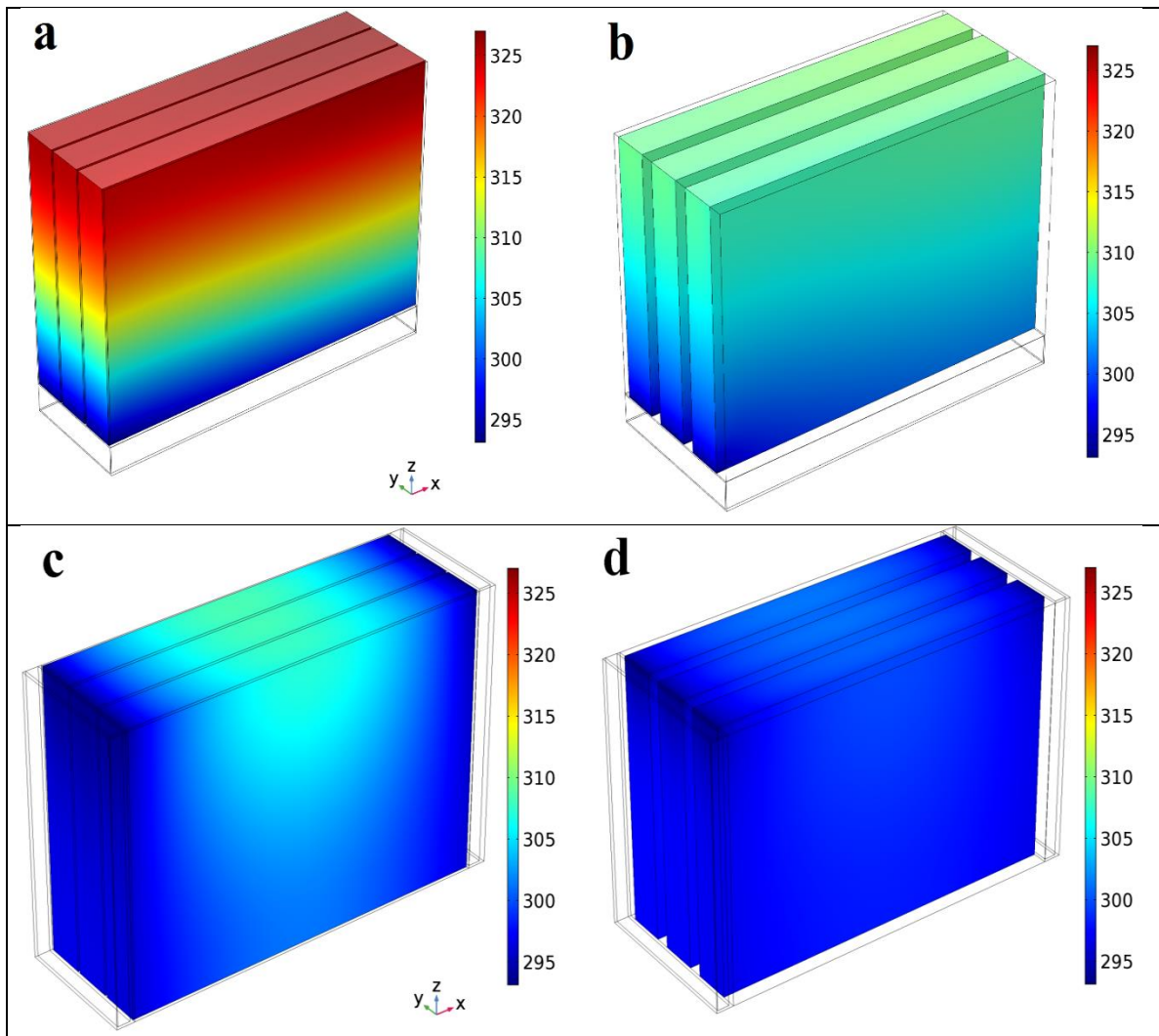
Figure 4-16. Temperature distribution of (a) single channel design at Re= 1850, plate thickness=1mm, (b) single channel design at Re=500, plate thickness=5mm, (c) double channel design at Re= 1850, plate thickness=1mm, (d) double channel design at Re=500, plate thickness=5mm

The batteries temperature distribution with double channel design is presented in Fig. 4-16 (c) and (d). The maximum temperature is shifted to the top center of batteries due to the presence of channels at the sides of batteries. The maximum temperature location is slightly to the left because of higher heat generation in the positive tab. As the cooling plate thickness increases to 5mm, the temperature becomes almost uniform due to excellent heat conduction in the battery module as shown in Fig. 4-16 (d).

Conclusions

In this work, a streamlined coupled electrochemical-thermal battery model for a prismatic battery was established using COMSOL Multiphysics, and its thermal performance was validated using infrared thermography. Two indirect cooling systems were examined for a module containing six 5Ah NCA lithium-ion batteries. All simulations were performed under the federal urban driving cycle. The average and maximum temperature of batteries, their temperature uniformity and added volume of both cooling systems were compared. The performance of each cooling system was investigated using a series of coupled heat transfer, electrochemical-thermal, and flow dynamics simulations. The average and maximum module temperature rise as well as batteries temperature uniformity were investigated by changing Reynolds number and cooling plate thickness. At identical Reynolds number and cooling plate thickness, the double channel cooling system leads to a lower maximum and average temperature, and more uniform temperature distribution. The smallest Reynolds number and thickest cooling plate yield the most homogeneous temperature distribution and adequate cooling effect under the driving cycle. A thicker cooling plate successfully decreases both average and gradient of temperature in the module. However, increasing Reynolds number results in a more non-uniform temperature distribution. The pseudo 3D electrochemical-thermal model presented in this study is a useful tool for Li-ion battery designers to evaluate the effects of cell design parameters (i. e. cathode thickness) on the thermal behavior of a battery in an HEV battery module under driving cycles. The results may be used along with an Li-ion battery aging model to investigate the effects of cooling systems on the long term performance of batteries after repeated driving cycles. Future work will investigate the performance and optimal design of the cooling systems at different coolant inlet temperatures and multiple repetitions of the driving cycle.

References

[1]   Z. Ling, Z. Zhang, G. Shi, X. Fang, L. Wang, X. Gao, Y. Fang, T. Xu, S. Wang, X. Liu, Review on thermal management systems using phase change materials for electronic components, Li-ion batteries and photovoltaic modules, Renew. Sustain. Energy Rev. 31 (2014) 427–438. doi:10.1016/j.rser.2013.12.017.

[2]   Z.G. Qu, W.Q. Li, W.Q. Tao, Numerical model of the passive thermal management system for high-power lithium ion battery by using porous metal foam saturated with phase

change material, Int. J. Hydrogen Energy. 39 (2014) 3904–3913. doi:10.1016/j.ijhydene.2013.12.136.

[3]   T. Teratani, R. Mizutani, K. Yamamoto, T. Anegawa, Energy-saving technologies for automobiles, IEEJ Trans. Electr. Electron. Eng. 3 (2008) 162–175. doi:10.1002/tee.20252.

[4]   T.M. Bandhauer, S. Garimella, T.F. Fuller, A Critical Review of Thermal Issues in Lithium-Ion Batteries, J. Electrochem. Soc. 158 (2011) R1. doi:10.1149/1.3515880.

[5]   Z. Rao, S. Wang, M. Wu, Z. Lin, F. Li, Experimental investigation on thermal management of electric vehicle battery with heat pipe, Energy Convers. Manag. 65 (2013) 92–97. doi:10.1016/j.enconman.2012.08.014.

[6]   G. Karimi, X. Li, Thermal management of lithium-ion batteries for electric vehicles, (2013) 13–24. doi:10.1002/er.

[7]   W. Tong, K. Somasundaram, E. Birgersson, A.S. Mujumdar, C. Yap, Numerical investigation of water cooling for a lithium-ion bipolar battery pack, Int. J. Therm. Sci. 94 (2015) 259–269. doi:10.1016/j.ijthermalsci.2015.03.005.

[8]   A. Alrashdan, A.T. Mayyas, S. Al-Hallaj, Thermo-mechanical behaviors of the expanded graphite-phase change material matrix used for thermal management of Li-ion battery packs, J. Mater. Process. Technol. 210 (2010) 174–179. doi:10.1016/j.jmatprotec.2009.07.011.

[9]   S. Wilke, B. Schweitzer, S. Khateeb, S. Al-Hallaj, Preventing thermal runaway propagation in lithium ion battery packs using a phase change composite material: An experimental study, J. Power Sources. 340 (2017) 51–59. doi:10.1016/j.jpowsour.2016.11.018.

[10]   M. Zolot, A. a. Pesaran, M. Mihalic, Thermal Evaluation of Toyota Prius Battery Pack, (2002). doi:10.4271/2002-01-1962.

[11]   Q. Wang, B. Jiang, B. Li, Y. Yan, A critical review of thermal management models and solutions of lithium-ion batteries for the development of pure electric vehicles, Renew. Sustain. Energy Rev. 64 (2016) 106–128. doi:10.1016/j.rser.2016.05.033.

[12]   Z. Rao, S. Wang, A review of power battery thermal energy management, Renew. Sustain. Energy Rev. 15 (2011) 4554–4571. doi:10.1016/j.rser.2011.07.096.

[13]   K. Yeow, H. Teng, M. Thelliez, E. Tan, 3D Thermal Analysis of Li-ion Battery Cells with Various Geometries and Cooling Conditions Using Abaqus, Imechanica.Org. (2012) 1–17. http://imechanica.org/files/Yeow_AVL_final_2202012.pdf.

[14]   K. Yeow, H. Teng, M. Thelliez, E. Tan, Thermal Analysis of a Li-ion Battery System with Indirect Liquid Cooling Using Finite Element Analysis Approach, (2012). doi:10.4271/2012-01-0331.

[15]   J. Xun, R. Liu, K. Jiao, Numerical and analytical modeling of lithium ion battery thermal behaviors with different cooling designs, J. Power Sources. 233 (2013) 47–61. doi:10.1016/j.jpowsour.2013.01.095.

[16]   R. Liu, J. Chen, J. Xun, K. Jiao, Q. Du, Numerical investigation of thermal behaviors in lithium-ion battery stack discharge, Appl. Energy. 132 (2014) 288–297. doi:10.1016/j.apenergy.2014.07.024.

[17]   D. Chen, J. Jiang, G.H. Kim, C. Yang, A. Pesaran, Comparison of different cooling methods for lithium ion battery cells, Appl. Therm. Eng. 94 (2016) 846–854. doi:10.1016/j.applthermaleng.2015.10.015.

[18]   Y. Tang, M. Jia, J. Li, Y. Lai, Y. Cheng, Y. Liu, Numerical Analysis of Distribution and Evolution of Reaction Current Density in Discharge Process of Lithium-Ion Power Battery, J. Electrochem. Soc. 161 (2014) E3021–E3027. doi:10.1149/2.004408jes.

[19]   C.R. Pals, J. Newman, Thermal Modeling of the Lithium / Polymer Battery - II. Temperature profiles in cell stack, J. Electrochem. Soc. 142 (1995) 3282–3288. doi:10.1149/1.2049975.

[20]   A. Eddahech, O. Briat, J.M. Vinassa, Thermal characterization of a high-power lithium-ion battery: Potentiometric and calorimetric measurement of entropy changes, Energy. 61 (2013) 432–439. doi:10.1016/j.energy.2013.09.028.

[21]   D.Y. Goswami, Principles of Solar Engineering, Third Edition, 2015. doi:10.1017/CBO9781107415324.004.

[22]   J. Pátek, J. Hrub, J. Klomfar, M. Součková, A.H. Harvey, Reference correlations for thermophysical properties of liquid water at 0.1 MPa, J. Phys. Chem. Ref. Data. 38 (2009) 21–29. doi:10.1063/1.3043575.

[23]   T. Ian, P. Washington, Battery Cooling Structure, U.S. Patent US20130146249A1, 2013.

[24]   J. Smith, M. Hinterberger, P. Hable, J. Koehler, Simulative method for determining the optimal operating conditions for a cooling plate for lithium-ion battery cell modules, J. Power Sources. 267 (2014) 784–792. doi:10.1016/j.jpowsour.2014.06.001.

[25]   J. Jaguemont, L. Boulon, Y. Dubé, A comprehensive review of lithium-ion batteries used in hybrid and electric vehicles at cold temperatures, Appl. Energy. 164 (2016) 99–114. doi:10.1016/j.apenergy.2015.11.034.

[26]   H. Care, S. Net, E. Marion, E. Lewin, S. Altman, C. Market, M. Care, F. Viability, S.N. Providers, M. Isbn, T. Pdf, N.A. Press, N. Academy, National Research Council. Review of the Research Program of the Partnership for a New Generation of Vehicles, fourth report, National Research Council, Washington, DC, 2000.

[27]   A. Santucci, A. Sorniotti, C. Lekakou, Power split strategies for hybrid energy storage systems for vehicular applications, J. Power Sources. 258 (2014) 395–407. doi:10.1016/j.jpowsour.2014.01.118.

[28]   K. Gokce, A. Ozdemir, A Rule Based Power Split Strategy for Battery / Ultracapacitor Energy Storage Systems in Hybrid Electric Vehicles, Int. J. Electrochem. Sci. 11 (2016) 1228–1246.

[29]   J. Smith, M. Hinterberger, P. Hable, J. Koehler, Simulative method for determining the optimal operating conditions for a cooling plate for lithium-ion battery cell modules, J. Power Sources. 267 (2014) 784–792. doi:10.1016/j.jpowsour.2014.06.001.

Chapter 5 Experimental and numerical investigation on the performance of carbon-based nanoenhanced phase change materials for thermal management applications

5.1. Introduction

Paraffin-based phase change materials (PCM) are considered as a promising energy storage mechanism through solid–liquid phase change at the melting point temperature. This energy storage could have significant applications in the solar energy storage [1–3] and passive cooling of portable electronics [4–6]. However, the performance of paraffin-based PCM is restricted by their low thermal conductivity. The amount of phase change during a heating or cooling process depends on the effective thermal penetration into the PCM. Also, in the thermal management of temperature sensitive electric devices (e.g. passive cooling of lithium-ion batteries), it is crucial to control the contact temperature between the PCM and the device. The amount of heat penetration and the contact temperature of two bodies in thermal contact are functions of the PCM thermal conductivity. Thus, it is essential to enhance the thermal conductivity of PCM for increasing the amount of thermal energy storage or to control the contact temperature.

A number of methods were reported to enhance the effective thermal conductivity of paraffin-based PCM [7–10]. The addition of highly conductive carbon-based nanoparticles was proposed as an effective approach to increase the thermal conductivity of PCM due to their low densities and intrinsic high thermal conductivities within the range of 1000–6000 W/mK. Table 5-1 shows a summary of some recent works on the thermal conductivity enhancement of PCM utilizing different types of nano-sized carbon fillers. It is observed that there is a considerable discrepancy between the thermal conductivity enhancement results, indicating the preparation method is significantly important in improving the thermal properties of nano-enhanced PCM (NePCM).

Table 5-1. Studies on the thermal conductivity enhancement of carbon-based NePCM

Nanoparticle type(s)	Nanoparticle thickness/diameter (nm)	Max. Concentration,%	Max. Thermal Conductivity Enhancement (k_{NePCM}/k_{PCM}),%	Reference
CNF	9000	10 wt	507.8	[25]
CNF+ indium	10000	21 vol	4100	[30]
SWCNT	30	2 wt	180	[31]
graphene	2	0.3 wt	1100	[32]
graphene MWCNT	15 65	20 vol	2800 832	[33]
CNF CNT	200 30	10 wt	145 124	[26]
S-MWCNT L-MWCNT	815 3050	5 wt	131 123	[34]

CNF	150-200			115	
GNP	420			273	
MWCNT	-	5 wt		200	[10]
graphene	-			1	
graphite	-			1292	
GNP	1000/10	5 vol		204	[35]
	15000/10	4 vol		966	

In contrast to the intensive research on thermophysical properties of NePCM, less work presented on the phase change heat transfer characteristics of these materials in cylindrical geometry. The heat transfer characteristics by treating the NePCM as homogeneous materials with equivalent thermophysical properties were numerically studied in both solid and liquid phases. The solid phase heat transfer was conduction-dominated and the observed enhancement in heat diffusion was attributed to the increased thermal conductivity of NePCM, which was verified by experiments [11–13].

Table 5-2. Studies on NePCM melting in cylindrical containers

PCM	Nanofiller/Max concentration	Container geometry	Boundary condition	k/μ prediction method	Most significant findings	Reference
1-dodecanol	GNP/1 vol%	spherical	Isothermal heating	Experimental	50% increase in k, 60 times increase in μ, NePCM decelerated melting due to the effects of increased μ	[18]
Water	Cu/10 vol%	Rectangular	Isothermal heating and cooling	Mixture model	NePCM enhanced the melting process and quickened the heat transfer and movement of melting front	[14]
Paraffin	Al_2O_3/5 wt%	Rectangular	Source and sink on the sidewalls	Mixture model	The fastest melting rate occurred at 2 wt% while nanoparticles	[15]

					showed no effect at 5 wt%	
1-dodecanol	CNT/2 wt%	Cylindrical	Isothermal heating from bottom	Experimental	Increased viscosity at 2 wt% concentration resulted in melting degradation compared to pure PCM	[36]
1-tetradecon al	GNP/3 wt%	Cylindrical	Isothermal heating from bottom	Experimental	The melting at high temperatures suppressed at 3 wt% loading due to 10 fold increase in μ	[21]
Water	Cu/4 wt%	Cylindrical	Isothermal heating and cooling	Mixture model	Nanoparticle s enhanced the melting rate at all concentration s	[16]
Paraffin	Cu/12 vol%	Cylindrical	Convection at the outer surface	Mixture model	Higher concentration s enhanced the melting and solidification	[17]

In contrast to the intensive research on thermophysical properties of NePCM, less work presented on the phase change heat transfer characteristics of these materials in cylindrical geometry. The heat transfer characteristics by treating the NePCM as homogeneous materials with equivalent thermophysical properties were numerically studied in both solid and liquid phases. The solid phase heat transfer was conduction-dominated and the observed enhancement in heat diffusion was attributed to the increased thermal conductivity of NePCM, which was verified by experiments [11–13].

However, the presence of nanoparticles may negatively affect the heat transfer in the liquid phase, because the natural convection in a melted PCM usually dominates. A summary of the recent studies focusing on the phase change heat transfer of NePCM in different geometries is provided in Table 5-2. Numerical studies show an acceleration of

melting in NePCM in cylindrical vessel compared to the pure phase change material due to the higher thermal conductivity of NePCM in solid and liquid phases [14–17]. Some of these numerical results are however questionable due to the considerable uncertainties associated with the thermal conductivity and viscosity data used for the NePCM. The experimental measurements indicate that the thermal conductivity of the liquid phase PCM increases slightly even when fully percolating concentrations are used. Thus, both solid phase and liquid phase properties are significantly important for the accurate modeling of melting of NPCM. Using a single thermal conductivity equation, as commonly utilized in the literature, may not result in sufficiently precise predictions. The presence of the nanoparticles also increases the viscosity of the melted PCM and leads to the degradation of natural convection. For instance, measurements done by Fan [18] showed that the thermal conductivity of the NePCM was enhanced by 50% at 1 wt% concentration, while the undesirable dynamic viscosity was increased more than 60 times for the same nanoparticle concentration.

Although this dramatic growth in viscosity highly deteriorates the natural convection, higher nano-filler concentration NePCM are of interest due to their so called form-stability. However, there is no data on the heat transfer characteristics of form-stable NePCM available in the literature. Such a data is valuable in the design of electric devices passive thermal management systems where the form-stability is favorable in order to minimize the risk of melted PCM leakage.

The purpose of this work is to assess and compare the thermophysical properties, and the heat transfer enhancement of the phase change nanocomposites using different carbon additives. In this paper, three paraffin based nanocomposites are prepared by using different carbon additives, namely, carbon nano-fiber (CNF), graphene nano-platelets (GNP), and graphite nano-powder (GrP). The temperature dependent thermophysical properties of these nanocomposites are first measured and analyzed by a scanning electron microscopy (SEM) and a differential scanning calorimeter (DSC). The thermal conductivity of the samples is measured by a C-therm thermal analyzer. The thermal responses of the NePCM composites during the phase change are investigated both experimentally and numerically.

Nomenclature

C_p	specific heat (J kg^{-1} K^{-1})
$\boldsymbol{g}$	gravity acceleration vector (m s^{-2})
h	convection heat transfer coefficient (W m^{-2} K^{-1})
H	container height (m)
$\boldsymbol{I}$	identity matrix
k	thermal conductivity (W m^{-1} K^{-1})

L	latent heat (J kg^{-1})
$\boldsymbol{n}$	normal vector
p	static pressure (Pa)
q''	heat flux (W m^{-2})
R	container radius (m)
t	time (s)
T	temperature (K)
T_∞	ambient temperature (K)
$\boldsymbol{u}$	velocity vector (m s^{-1})
Greek letters	
μ	dynamic viscosity (Pa.s)
ρ	density (kg m^{-3})
ϕ	mass fraction
Subscripts and superscripts	
ini	initial
max	maximum
np	nanoparticle

5.2. Preparation of nanocomposites

A paraffin wax with a nominal melting point (T_m) of 333.15K is adopted as the base PCM. The carbon-based nanoparticles are purchased from MK Impex Corp., Ontario, Canada. The materials are used as received without further purification in all experiments. The preparation process of phase change composites made of nanoparticles and organic PCM was previously reported in the literature [19], and a similar method is used in this work to manufacture the CNF-, GNP- and GrP-based nanocomposites. The nanoparticles at desired weights are added to the melted PCM at 90°C and intensively stirred for 30 minutes to provide a homogeneous mixture. A temperature higher than the PCM melting point is preferred as a relatively low viscosity of the molten PCM facilitates the dispersion of the nanoparticles. A very small amount of PolyVinylPyrrolidone-40 (Sigma-Aldrich, Oakville, Canada) is added to the mixture as a dispersing additive to assure a good dispersion of the nanoparticles in the liquid PCM. Finally, the liquid composite is rigorously sonicated at about 90°C for 2 hours prior to the solvent evaporation. For each nanoparticle, four samples with different weight fractions of carbon additive (2.5%, 5%, 7.5% and 10%) are prepared. The thermophysical properties of the materials used in this study are listed in Table 5-3.

Table 5-3. Thermophysical properties of the materials used in this study

Property	Paraffin wax	CNF	GNP	Graphite nanopowder	Aluminum

Melting point, K	333.15	-	-	-	-
Thermal conductivity, $Wm^{-1}K^{-1}$	Solid: 0.25 Liquid: 0.16	-	-	-	205
Specific heat, $Jkg^{-1}K^{-1}$	Solid: 1180 Liquid: 2056	-	-	-	920
Density, kgm^{-3}	910	2100	100	2200	2700
Dynamic viscosity, mPa.s	5.5	-	-	-	
Latent heat, $kJkg^{-1}$	119.3	-	-	-	-
Characteristic length	-	OD: 400nm Length: 50μm	Thickness: 7nm APS: 15μm	APS: 50nm	-

5.3. Thermophysical characterization of nanocomposites

5.3.1. Thermal conductivity measurement

The thermal conductivity of NePCM composites are measured with a C-Therm TCi thermal conductivity analyzer (accuracy better than 5% of the reading) using modified transient plane source (MTPS) technique.

In each measurement, the solid nanocomposite is initially heated to a temperature higher than its melting temperature inside a chamber. The liquid sample is then allowed to solidify onto the sensor surface to assure a uniform thermal contact between the sample and the sensor surface. The thermal effusivity and thermal conductivity of NePCM samples are directly measured by the thermal analyzer.

5.3.2. Differential scanning calorimetry (DSC)

The heat capacity, latent heat of fusion, and melting temperature of the nanocomposite are determined using a differential scanning calorimeter (Mettler-Toledo DSC822). A sample size of around 15-20mg (using a balance with a resolution of 0.001 mg) is loaded to the DSC cell and the data is collected for the 2nd run at a rate of 3K/min. The nitrogen is used as the purge gas in all tests.

5.3.3. Viscosity measurement

The dynamic viscosity of the liquid NePCM samples is measured using a rotational viscometer (Brookfield LVT, Cooksville, Canada) with an accuracy of 1% at elevated temperatures from about 333K to 363K at an increment of 10K. Temperature control during viscosity measurements is performed using a constant temperature bath.

5.4. Heat transfer characterization

Fig. 5-1 shows the schematic diagram of latent heat temperature control test system. The experimental test rig mainly consists of a cartridge heater (OD=1cm), adjustable power supply, data acquisition system, and four k-type thermocouples. The NePCM nanocomposite is filled in a small aluminum cylindrical test cell (ID=5cm). Four thermocouples record the NePCM temperature variation with time at the installing positions presented in Table 5-2. The thermocouples are located in various angular positions to minimize the effects of their presence on the nanocomposite temperature distribution. The bottom of the test cell is filled with a 10mm thick insulating glue which serves as an insulator, and a support of thermocouples and the tip of the heater which is carefully fixed at the center of the cell. The outer bottom surface of the test cell jacketed with a 50mm thermal insulation layer to minimize the heat losses from the bottom. The experimental rig is placed inside a constant temperature chamber to ensure uniform natural convection heat transfer from the outer surfaces. The locations of thermocouples are given in Table 5-4. In an effort to assure the repeatability of the results, the tests are performed 3 times for each NePCM sample and the average values of temperature are reported.
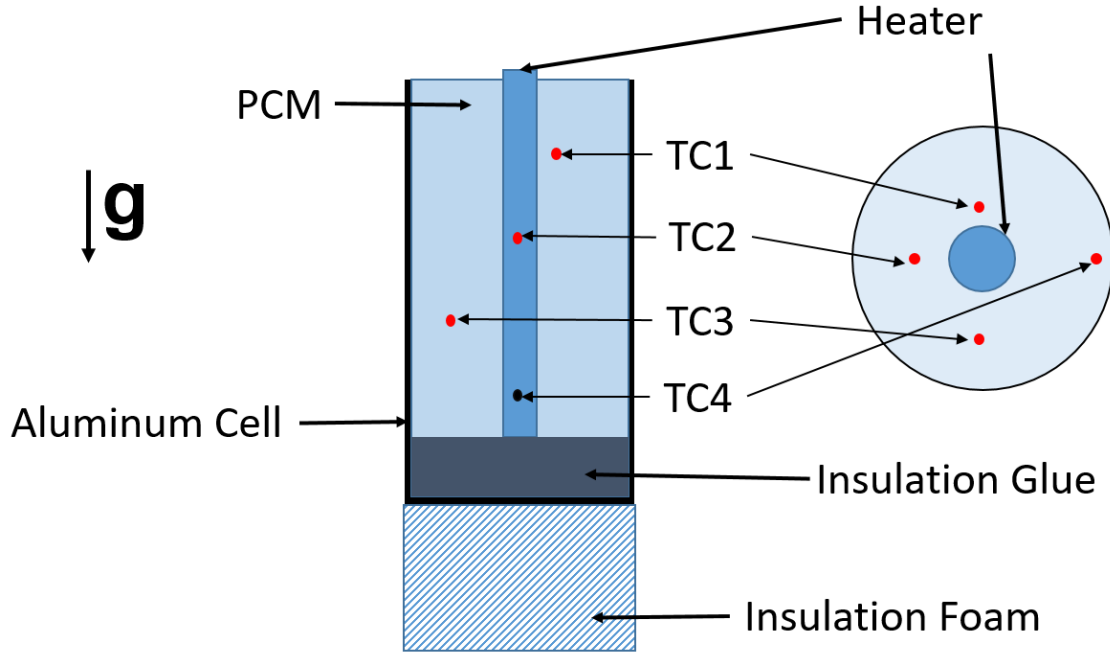
Figure 5-1. Schematic diagram of experimental setup

5.5. Numerical modeling

The numerical domain is considered as 2-D cylinders with a vertical symmetry axis at the center of the heater. The flow of liquid PCM and NePCM is assumed to be unsteady, laminar, Newtonian, and weakly compressible [20]. It is also assumed that the melted NePCM behaves as a continuous medium with thermodynamic equilibrium and no slip velocity between the base PCM and solid particles.

Table 5-4. Position of thermocouples in the test cell

Thermocouple	1	2	3	4
Radius, mm	9	13	17	21
Angular position, degrees	0	90	270	360
Height, mm	40	30	20	10

All temperature-dependent thermophysical properties of the nanocomposites are used as measured in this study. The samples' density variation is calculated as follow [21]:

$$\rho_{NePCM} = (1 - \phi)\rho_{PCM} + \phi\rho_{np} \qquad (5.1)$$

where ρ_{np} is the density of the nanoparticles, and ϕ is the mass fraction.

The governing equations used in the 2-D transient laminar natural convection flow are as follow:

Continuity:

$$\frac{\partial \rho_{NePCM}}{\partial t} + \nabla.(\rho_{NePCM}\boldsymbol{u}) = 0 \tag{5.2}$$

Momentum:

$$\rho_{NePCM}\frac{\partial \boldsymbol{u}}{\partial t} + \rho_{NePCM}(\boldsymbol{u}.\nabla)\boldsymbol{u} \tag{5.3}$$

$$= \nabla.\left[-p\boldsymbol{I} + \mu(\nabla\boldsymbol{u} + (\nabla\boldsymbol{u})^T) - \frac{2}{3}\mu(\nabla.\boldsymbol{u})\boldsymbol{I}\right] + \rho_{NePCM}\boldsymbol{g}$$

Energy:

$$(\rho C_p)_{NePCM}\frac{\partial T}{\partial t} + (\rho C_p)_{NePCM}\boldsymbol{u}.\nabla T + \nabla.(-k_{NePCM}\nabla T) = 0 \tag{5.4}$$

The boundary and initial conditions are as follow:

$$u = w = 0 \quad at \; r = R \; and \; z = 0, t \geq 0$$

$$p = 0 \quad at \; z = H, t \geq 0$$

$$q'' = -k_{NePCM}\frac{\partial T}{\partial r} \quad at \; r = R, t \geq 0$$

$$\frac{\partial T}{\partial z} = 0 \quad at \; z = 0, t \geq 0$$

$$\boldsymbol{n}.(k_{NePCM}\nabla T) = h(T - T_\infty) \quad at \; r = R \; and \; z = H, t \geq 0$$

$$T_{(x,z)} = T_{ini} \quad at \; t = 0$$

The simultaneous governing equations are solved using COMSOL Multiphysics v5.2 based on the finite element method. The specific heat of nanocomposites are defined as functions of temperature based on values obtained from the DSC measurements and the thermal conductivity in the mushy phase are estimated using a linear interpolation function. The mesh independency is checked to ensure the reliability of the simulation results and to determine whether changing the mesh size influences the results or not. A free quadrilateral mesh is used in the 2D domain and the number of the elements is varied from about 8,000 to 40,000. The mesh independency study shows that the results are mesh independent when the number of total elements is more than 26,878. Therefore, this mesh design is used in the simulations.

5.6. Results and discussion

5.6.1. Thermal conductivity analysis of NePCM composites

Fig. 5-2(a)-(c) depicts the thermal conductivity of the pure paraffin and nanocomposites as a function of temperature and concentration. The thermal conductivity of samples at temperatures close to the melting point (about $60^{\circ}C$) are not shown due to the non-equilibrium state of the materials at this temperature which may lead to imprecise measurements [22]. This figure shows that the thermal conductivity of each solid phase NePCM sample is increased by adding the nanoparticles and it does not vary with temperature. The right-hand side of Fig. 5-2(a)-(c) ($T>60^{\circ}C$) presents the thermal conductivity of the liquid phase NePCM composites. In the liquid phase, the thermal conductivity grows insignificantly with increasing both mass fraction and temperature. Therefore, the thermal conductivity of the NePCM nanocomposites cannot be considered a strong function of temperature or concentration in the liquid phase.

These results suggest that the enhancement in the solid state is much higher than the liquid state upon the addition of nanoparticles. During the solidification process, nanoparticles may trap in the wax micron to millimeter size crystalline structures [23]. The growth of these structures increases the stress on the nanoparticles and enhances the effective contact area between nanoparticles, and between the nanoparticle-wax intersections which leads to an increase in the solid phase NePCM. The internal stress on the nanoparticles is released during the melting process and decreases the inter-particle contact area that is observed as a reduction in thermal conductivity enhancement in the liquid phase. The reduction in thermal conductivity observed in the liquid phase is a concern for temperature control applications due to the natural convection repression in the presence of nanoparticles. The effects of nanoparticles on the thermal behavior of NePCM will be discussed in section 5.6.4.
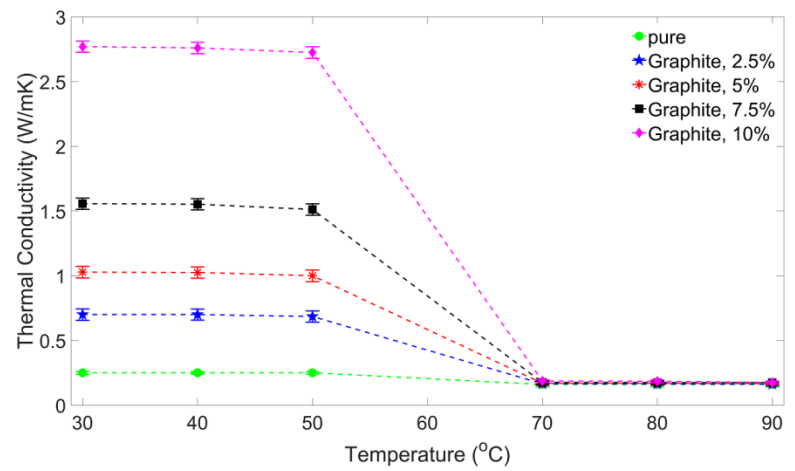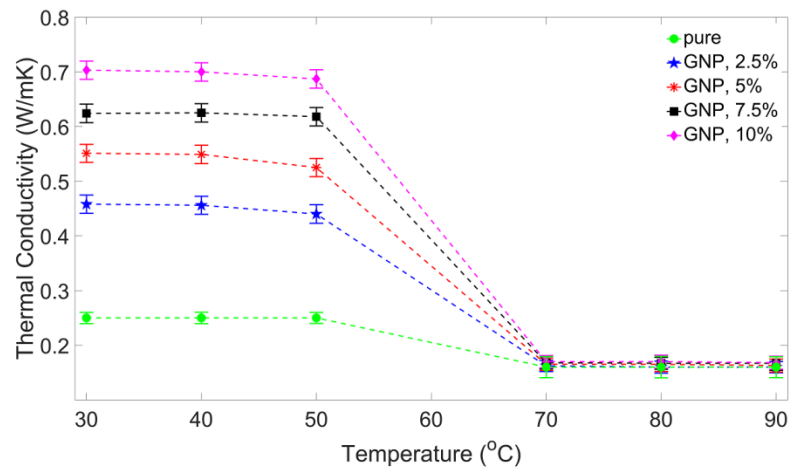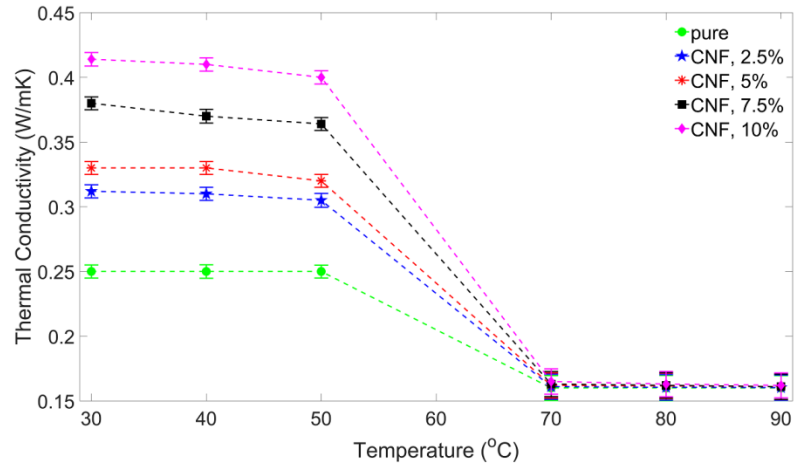
Figure 5-2. The thermal conductivity of (a) CNF-based, (b) GNP-based, and (c) Graphite-based nanocomposites

Fig. 5-3 shows the ratio of the thermal conductivity of the solid NePCM to the thermal conductivity of solid pure wax at 40°C, as a function of the mass fraction. The different thermal conductivity enhancement obtained from various nano-additives may be due to the dissimilar structure and size of these nanoparticles which affect the thermal resistance in the composites. The thermal contact resistance is a major factor that limits the thermal conductivity enhancement of carbon-based nanocomposites [24]. A low thermal contact resistance at the interface between the PCM and nanoparticles, as well as a relatively smaller number of contact points, can improve the thermal conductivity of the nanocomposite.
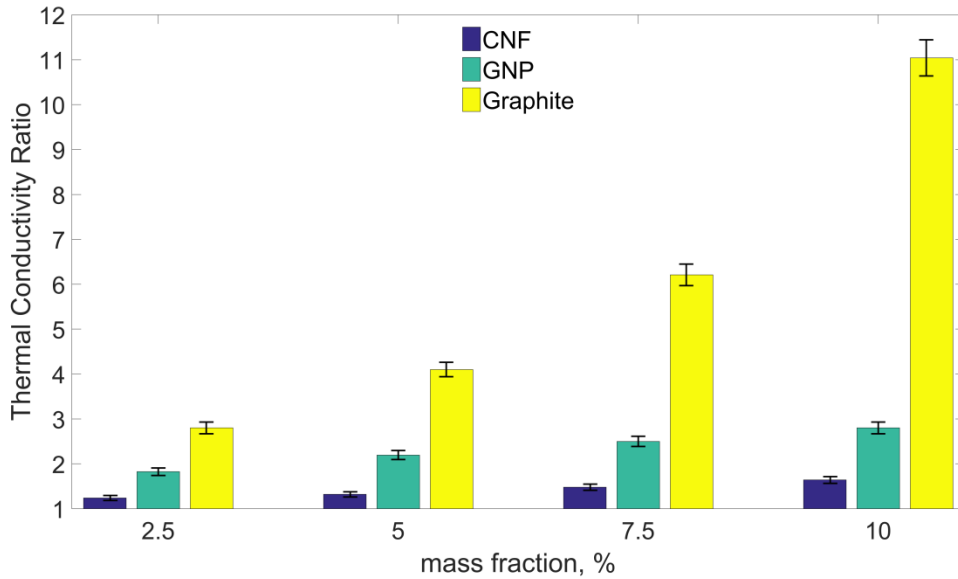
Figure 5-3. Thermal conductivity ratio ($\frac{k_{NePCM}}{k_{PCM}}$) of solid phase nanocomposites as a function of mass fraction at 40°C.

5.6.2. DSC analysis of NePCM composites

In order to investigate the effects of the different additives on the thermal properties of the paraffin wax, the melting point, freezing point and latent heat of these nanocomposite samples are measured and compared using the DSC analysis. Fig. 5-4(a)-(c) shows the results of the DSC analysis of NePCM samples with different carbon additives at various concentrations. The melting and freezing processes of the composites are illustrated by the upper and under curves, respectively. It appears that the melting point of paraffin wax does not change considerably by adding different nanoparticles.
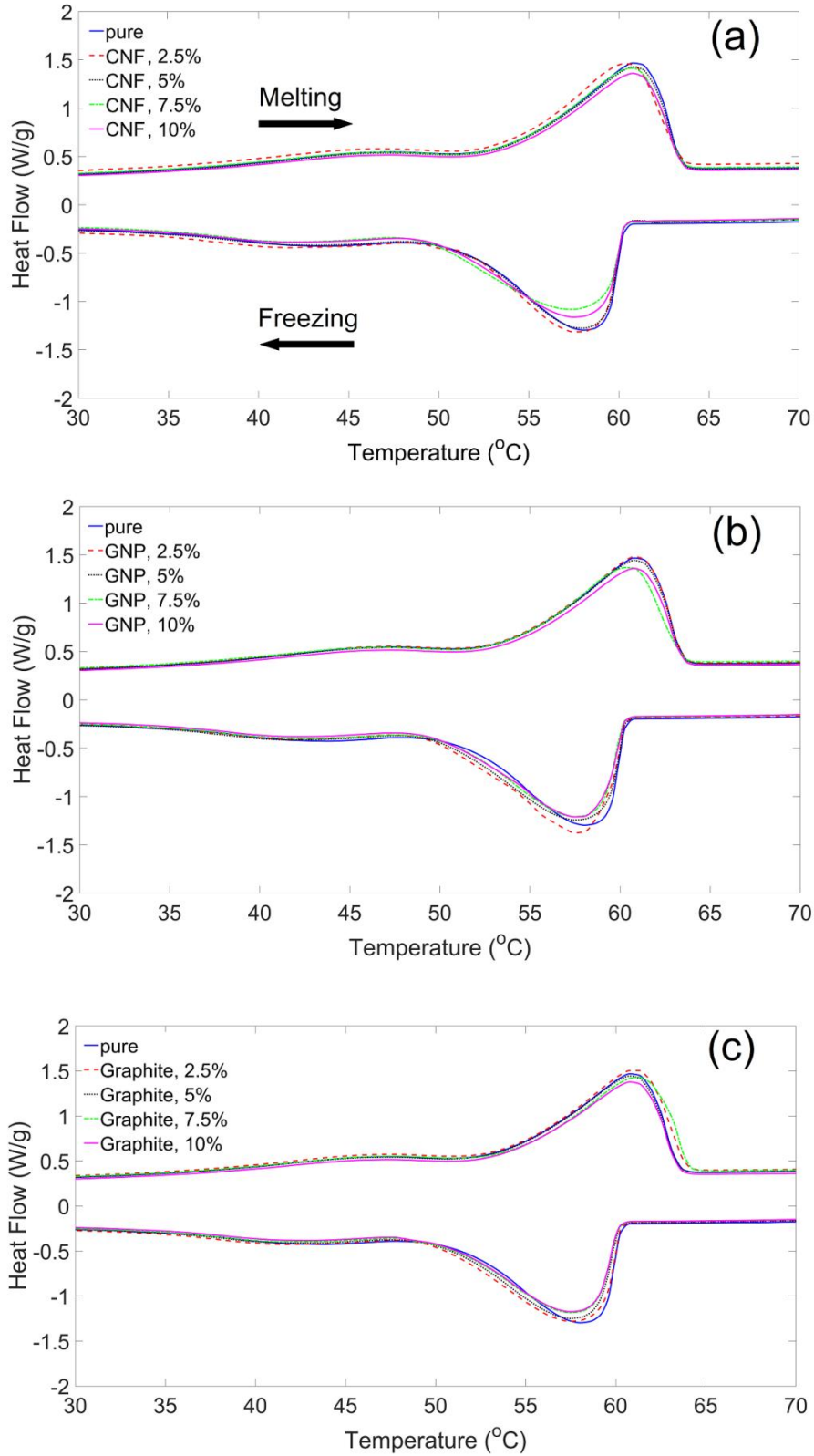
Figure 5-4. Differential scanning calorimetry measurements of nanocomposites as a function of mass fraction of (a) CNF, (b) GNP, (c) Graphite nanoparticles

The relevant enthalpies were calculated by integration the peaks above the baseline given by the DSC software and are compared in Fig. 5-5(a). As shown in this figure, the melting and crystallization enthalpies for paraffin nanocomposites at 2.5% mass fraction is slightly increased compared to the pure wax. This latent heat increment is attributed to the Van der Waals forces between nanoparticles and the wax [28]. The heat absorption during the change from solid to liquid is used to overcome the weak intermolecular forces of the PCM. The presence of nanoparticles can alter these forces in a way that the interaction potential between the paraffin wax and nanoparticles is larger than that between the wax molecules themselves if the concentration of the particles is high enough.

(a)

(b)
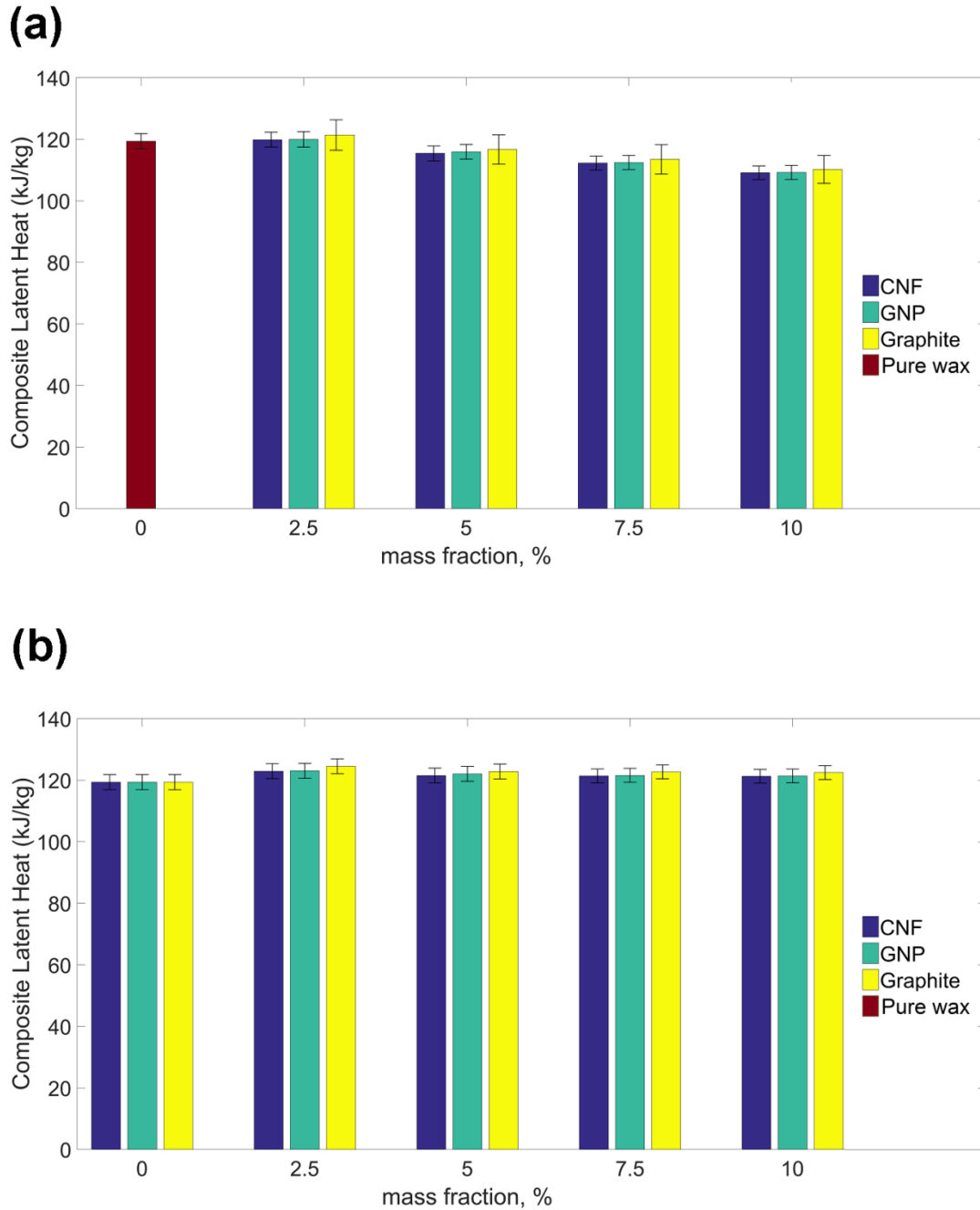
Figure 5-5. Phase change enthalpy of (a) nanocomposites and (b) paraffin alone in the nanocomposites with different nanoadditives

As seen in Fig. 5-5(a), a small concentration of the nanoparticles can enhance the molecular interaction and increase the latent heat of the nanocomposites due to the extremely large surface to volume ratio of the nanoparticles. At higher concentrations, the NePCM latent heats of fusion are degraded because of the accumulative replacement of

the paraffin wax with nanoadditives. In order to further assess the effects of nanoparticles on the latent heat of paraffin wax, a compensated latent heat can be defined as follow:

$$L_{PCM} = \frac{L_{NePCM}}{1 - \phi} \qquad (5.5)$$

where L_{PCM} is the latent heat of the paraffin wax alone in the nanocomposites and ϕ is the weight concentration of nanoparticles.

As shown in Fig. 5-5(b), the values of latent heat of the paraffin wax alone increases in the presence of nanoparticles compared to the pure wax. The mass fraction of nanoparticles has no considerable effect on the latent heat as depicted in this figure.

5.6.3. Viscosity of NePCM composites

The measured viscosities of the various NePCM samples are presented in Fig. 5-6(a)-(c). As shown in this figure, the values of viscosity increase drastically with nanoparticles concentration. The measured values of viscosity decrease with temperature and the reduction becomes more noticeable at both higher temperatures and concentrations.
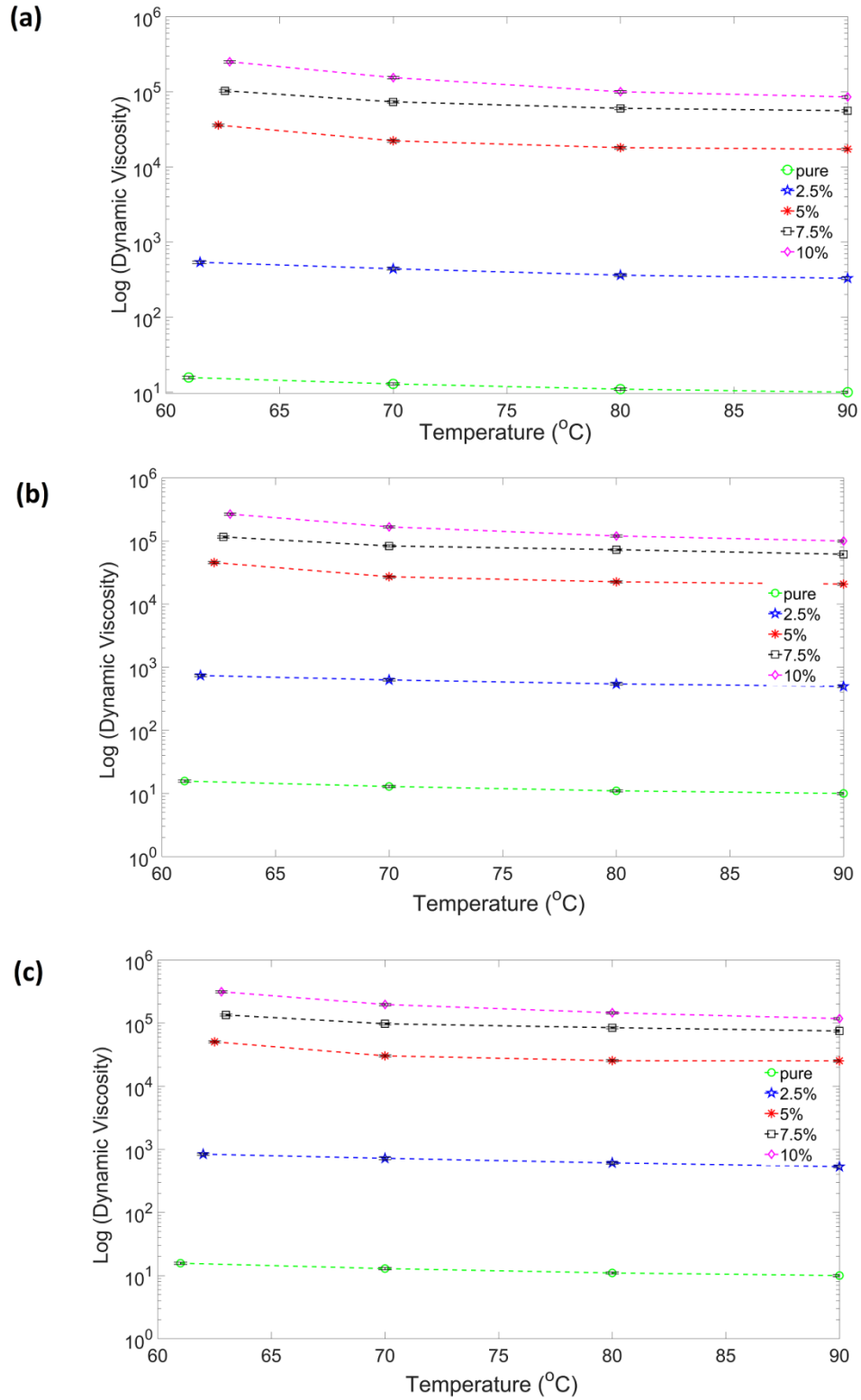
Figure 5-6. The dynamic viscosity of nanocomposites a function of mass fraction and temperature with (a) CNF, (b) GNP and (c) Graphite additives

The Brinkman's correlation for suspensions [29] is widely used for viscosity prediction in the numerical heat transfer modeling of NePCM composites [14–17], as follow:

$$\mu_{NePCM} = \mu_{PCM} \frac{1}{(1-\phi)^{2.5}} \tag{5.6}$$

where μ_{PCM} is the viscosity of melted pure paraffin.

Fig. 5-7 compares the measured values of viscosity with the ones predicted by Brinkman's correlation for different nanoparticles at 70°C. This figure shows that this correlation greatly underestimates the viscosity increase of nanocomposites which may result in an imprecise assessment of natural convection heat transfer during the melting process.
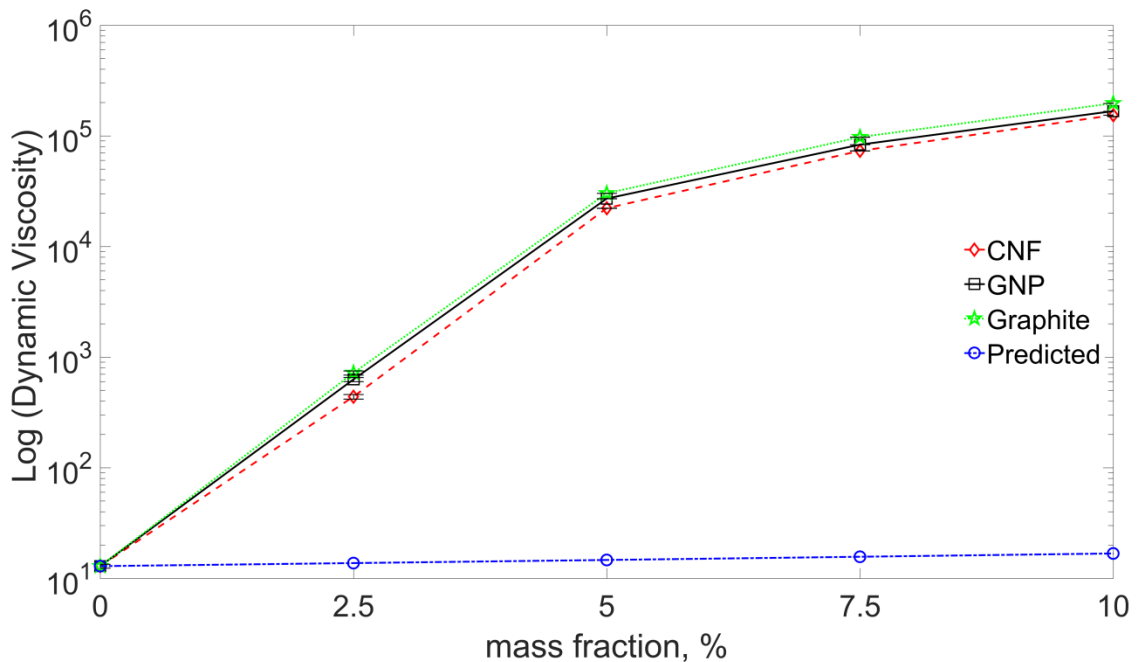
Figure 5-7. The measured and predicted dynamic viscosities of various nanocomposites as a function of mass fraction at 70°C

5.6.4. Heat Transfer Characterization of NePCM
In this section, the melting process of the pure wax and nanocomposites are experimentally and numerically investigated to assess the effects of the nanoparticles on the thermal behavior of NePCM samples. All tests are performed at a constant total heat

flux for duration of 1000 seconds to provide a framework for comparing the performance of nanocomposites.

The obtained values of pure wax and nanocomposites' temperature at mass fractions of 2.5% and 10% are shown in Fig. 5-8(a-h). Figure 5-8(a) shows the temperature variation recorded by thermocouple #1 (TC1 as shown in Fig. 5-1) for 2.5% composites. Clearly, the final temperature of CNF and GNP samples is higher than pure wax. A critical point with a rapid change in the slope of the nanocomposites curves can be seen around the local temperature of 337.5K as shown by red dashed line. Based on the DSC curves (Fig. 5-4), this temperature corresponds to the end of melting. This rapid increment is mainly attributed to the significant suppression of natural convection within the nanoparticles network. The minor increase in the thermal conductivity of the liquid phase CNF and GNP samples cannot compensate for the annihilation of the natural convection.
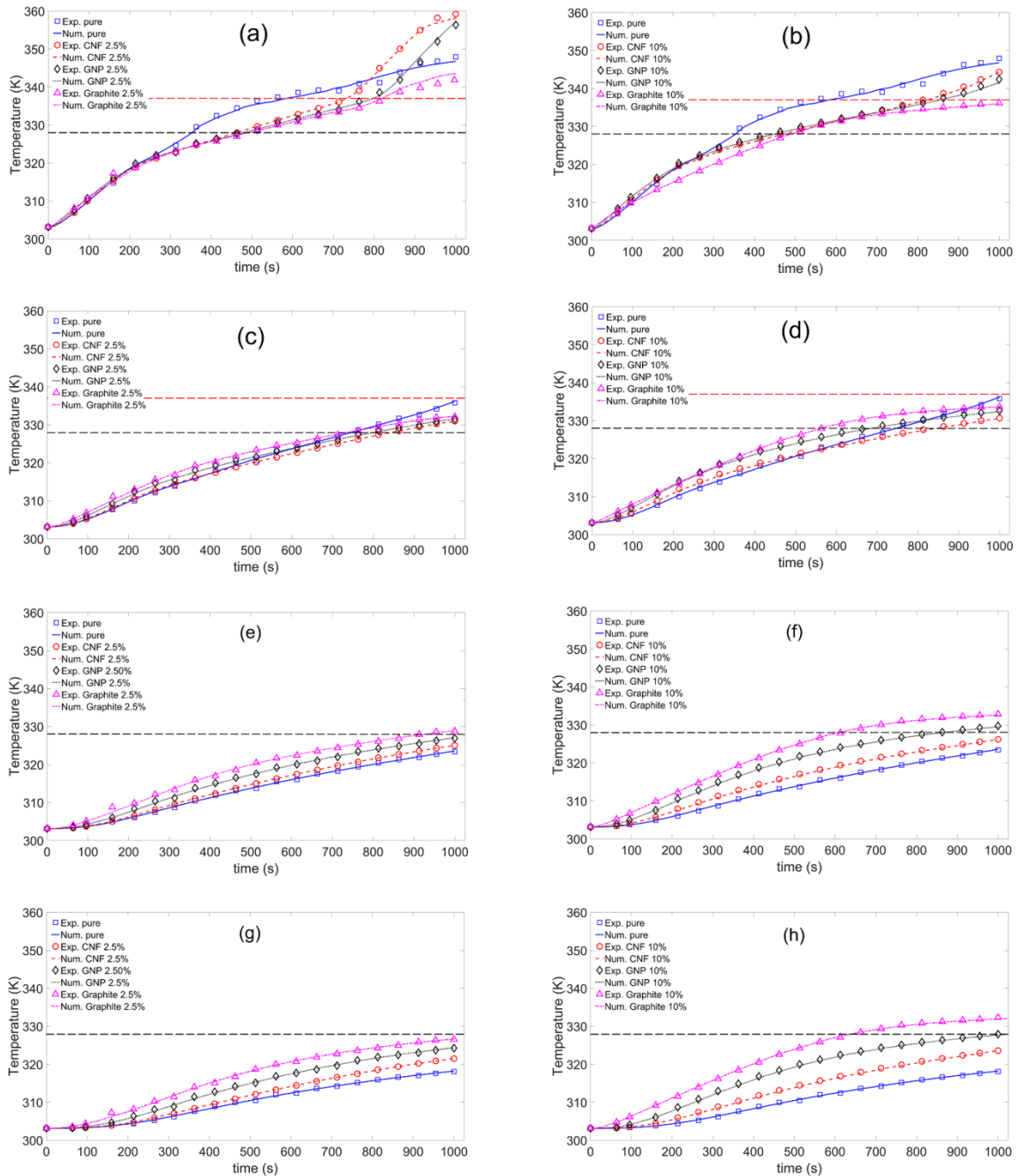
Figure 5-8. Measured and predicted temperature variation recorded with (a, b) TC1, (c, d) TC2, (e, f) TC3, (g, h) TC4

As shown in Fig. 5-8(b), when the mass fraction of composites increases to 10% the final temperature drops by about 15K compared to 2.5% samples due to more effective heat conduction. However, the transmission from the conduction-dominant to convection-dominant heat transfer is still observed in CNF and GNP curves in the form of a sharp

temperature increment after the end of melting (red dashed line). The graphite-based composite curve is in the shape of pure conduction because of its higher viscosity and thermal conductivity compared to other samples.

The temperature variations of TC2 in the pure wax, 2.5% and 10% composites are shown in Fig. 5-8(c) and (d). In all cases, the graphite-based sample shows the highest temperature in the solid phase (T<327) due to its higher thermal conductivity. As can be seen in Fig. 5-8(c), the pure wax temperature is higher at the beginning of the melting process (t≈740s). This shows the strong effect of natural convection on enhancing the heat transfer in the melted pure wax. The higher loading of nanoparticles (Fig. 5-8(d)) has a negligible effect on the thermal performance of CNF-based composites. However, a higher mass fraction of GNP and graphite additives reduces the amount of time that it takes for these samples to start melting by about 110 and 200 seconds, respectively. Increasing mass fraction of nanoparticles from 2.5% to 10% causes about 56% and 298% increment in the thermal conductivity of GNP and graphite nanocomposite, respectively. However, the thermal conductivity enhancement of CNF composite is only 31% which explains why adding more CNF to the pure wax does not improve the melting process considerably.

The transient temperature profiles in figures 5-8(e-h) depict a similar trend and shows the temperatures measured by TC3 and TC4 are higher when using the 10% nanocomposites. Furthermore, the graphite-based nanocomposite shows the highest temperature while the pure wax has the lowest temperature during the tests. A higher temperature enhances the heat rejection to ambient which can improve the thermal management of the heat source.

The numerical results follow the experimental data very closely as shown in Fig. 5-8. The normalized root mean square difference between the data is smaller than 2.9% in all cases. In the rest of this section, the thermal characteristics of the samples are discussed based on the results of the simulations.

The temperature distribution of the heater, pure wax and nanocomposites at t=1000s is shown in Fig. 5-9. The curvature in the temperature profiles of 2.5% nanocomposites and pure wax shows the effects of the natural convection heat transfer. During the melting process, the hot melted liquid PCM close to the heater moves toward the top of the container where it releases its energy to the ambient. This results in a higher melting rate in the upper part of the test cell compared to the lower part, causing a noticeable curvature of the melting interface. At greater mass fractions, the high viscosity of nanocomposite suppresses the natural convection which vanishes the curvature of temperature profiles.
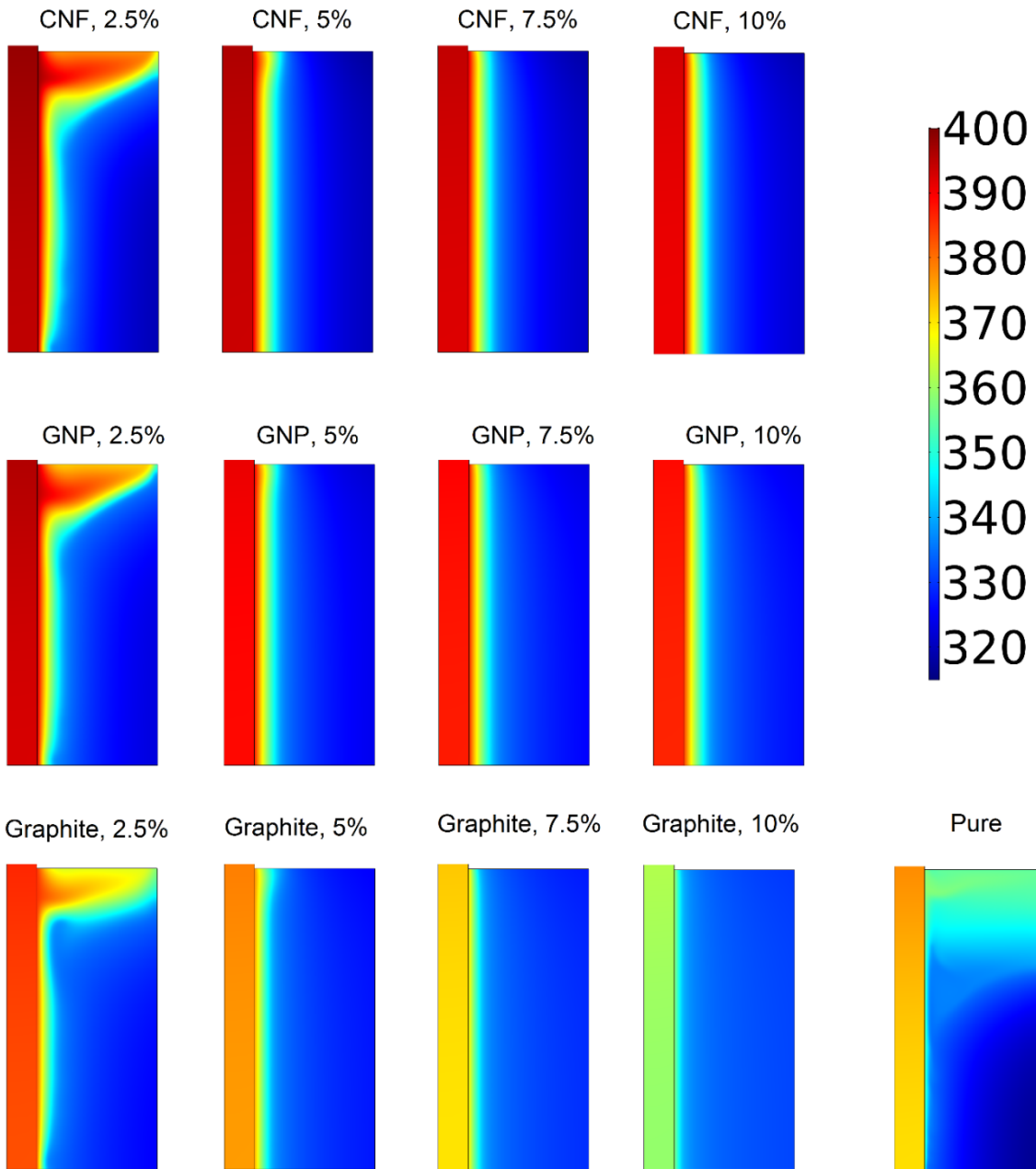
Figure 5-9. Comparison of temperature distribution in the pure paraffin and nanocomposites at t=1000s

The heater final temperature decreases with higher concentration of nanoparticles. This is more evident in graphite-based composites because of higher thermal conductivity of these samples compared to CNF and GNP composites. When quantitatively assessing the results, as presented in Table 5-5, it becomes evident that adding the CNF and GNP particles leads to an increased heater final temperature which is a serious concern in

thermal management applications. The reason may be attributed to the thermal conductivity enhancement of NePCM samples in the solid phase on one hand, and the annihilation of natural convection along with thermal conductivity drop in the melted nanocomposites on the other hand. It seems that in CNF, GNP, 2.5% and 5% graphite nanocomposites the suppression of natural convection has a stronger effect on the heat transfer in NePCM samples compared to the effects of their solid phase thermal conductivity enhancement. In the case of graphite-based composites, only higher mass fractions i.e. 7.5% and 10% can successfully lower the average heater temperature.

Table 5-5. Heater final temperature

PCM	Heater final temperature, (K)
Pure paraffin	371.7
CNF-based composite	
2.5 wt.%	395.9
5 wt.%	394.7
7.5 wt.%	393.5
10 wt.%	392.2
GNP-based composite	
2.5 wt.%	393.9
5 wt.%	389.7
7.5 wt.%	390.2
10 wt.%	388.5
Graphite-based composite	
2.5 wt.%	384.2
5 wt.%	377.5
7.5 wt.%	370.5
10 wt.%	359.9

In order to further study the effects of different nanoparticles on the average heater temperature, Fig 5-10 shows the heater average temperature variation with time. The heater temperature profiles are all similar except when the heater is in direct contact with pure wax. In this case, the heater temperature increases rapidly and exceeds the PCM melting temperature after about 110s. The maximum temperature (372.4K) occurs at about 575s and then slightly decreases to 371.7K at the end of the test. As the melting progresses, the temperature of the melted wax adjacent to the heater increases and buoyancy-driven convection is strengthened which enhances the heat rejection from the heater. The minor fluctuations of heater temperature after 500s implies the effects of strengthened natural convection heat transfer on the heater temperature as shown in Fig.

5-10. The results clearly show that the type and mass fraction of nanoadditives should be selected with great care because an insufficient thermal conductivity enhancement can worsen the heat source temperature control due to the strong degradation of natural convection in the presence of the networks of nanoparticles.
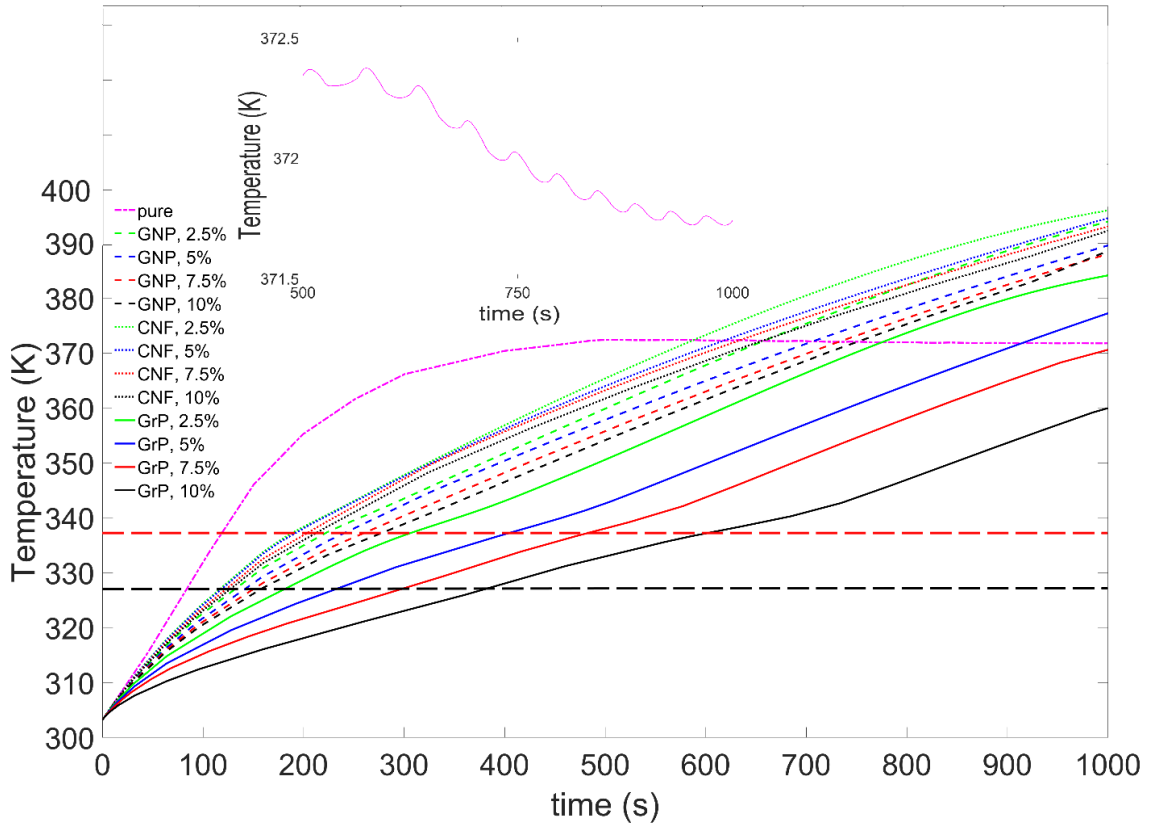
Figure 5-10. Heater average temperature variation with time

Another important aspect of a PCM-based thermal management system is the time it takes for the PCM to completely melt. This time is a measure of how long the thermal management system is capable of limiting the temperature at the desired levels. Fig. 5-11 depicts the un-melted portion of pure wax, 7.5% and 10% graphite-based nanocomposites at t=1000s. The melted PCM in this figure is considered as that part of the material at a temperature higher than the melting end temperature obtained from DSC curves. Quantitative analysis shows that at this moment 48% of pure wax is melted. The melted fraction of 7.5% and 10% graphite-based composites are 33% and 30%, respectively. Therefore, these samples employ a smaller fraction of the based paraffin latent heat capacity compared to the pure paraffin wax. In a thermal management system, this is advantage because may lead to a prolonged temperature control capability. The 10%

graphite-based composite shows the lowest melted fraction due to its higher thermal conductivity which results in both more sensible heat storage and more heat rejection to the ambient.

Thus, the current work experimentally and numerically demonstrates that the graphite powder nanoparticles contribute significantly to thermophysical modifications of the based paraffin, and also employing a 10% mass fraction of these nanoadditives results in the most effective temperature control.
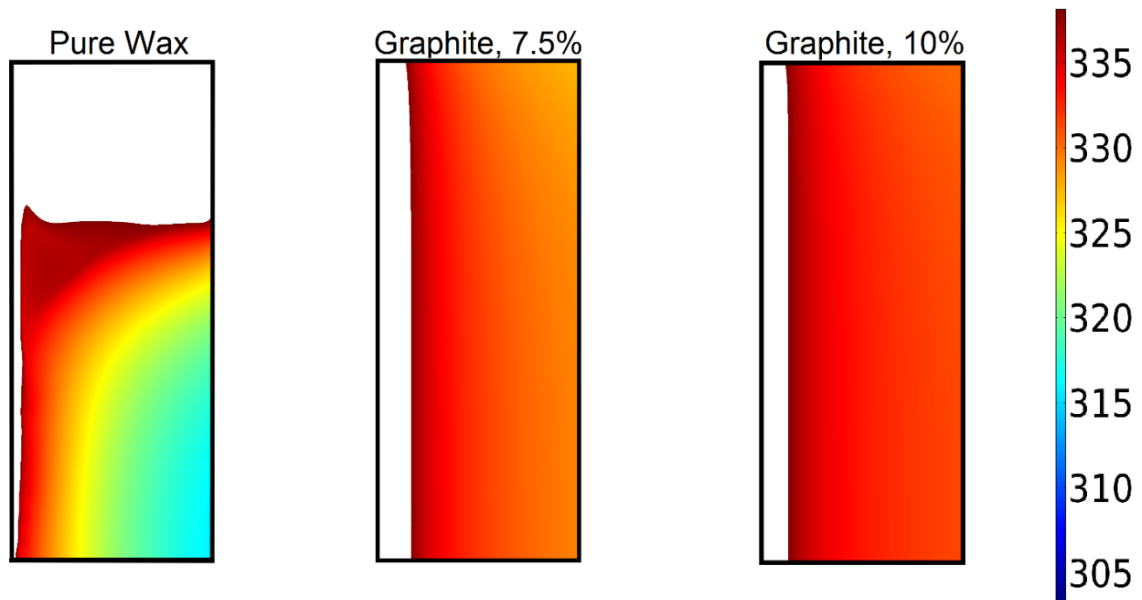
Figure 5-11. Temperature distribution in the un-melted portion of different PCM samples at t=1000s

5.7. Conclusion

Three paraffin based nanocomposites are prepared and examined for thermal management applications by three different carbon-based nanoparticles (carbon nanofiber, graphene nanoplatelets and graphite nanopowder) with mass fractions from 2.5% to 10%. An identical preparation method is used for all nanocomposites and their thermal conductivity, specific and latent heats as well as dynamic viscosity are measured. The SEM analysis is performed to observe the distribution of nanoparticles in the based PCM and it is revealed that the graphite particles effectively establish a relatively continues network in the based paraffin wax. The maximum solid state thermal conductivity enhancement of 11-folds is obtained by using 10% mass fraction of graphite powder while the DSC analysis shows that nanoparticles studied have a slight effect on

the melting temperature of nanocomposites. It is shown that adding a small fraction of nanoadditives results in a drastic increase of viscosity even in temperatures considerably higher than the nanocomposite melting point.

The experimental and numerical investigation of the thermal behavior of nanocomposites during the melting process indicates that the nanoparticles severely degrade natural convection heat transfer in the liquid phase. The average heat source temperature variation during melting process demonstrates that the suppression of natural convection in the presence of nanoparticles network as well as the thermal conductivity drop during the phase change of NePCM may lead to a weaker temperature control compared to the pure paraffin. Among the 12 nanocomposites studied only the graphite-based NePCM with 7.5% and 10% mass fractions enhance the thermal performance of the latent heat thermal management system. These results suggest that there is a trade-off between the degradation of natural convection and increase in thermal conductivity caused by nanoparticles that should be considered in PCM-based thermal management system design. Moreover, monitoring the temperature distribution in the nanocomposites reveals that the NePCM samples can provide a better temperature control with utilizing 18% less latent heat capacity of the system as compared to pure wax. The results of this study can provide a baseline for the optimal design of PCM-based thermal management of lithium-ion battery modules or photovoltaic cells where an effective temperature control is essential to enhance the safety and efficiency of systems.

References

[1]   A. Saraswat, R. Bhattacharjee, A. Verma, M.K. Das, S. Khandekar, Investigation of diffusional transport of heat and its enhancement in phase-change thermal energy storage systems, Appl. Therm. Eng. 111 (2017) 1611–1621. doi:10.1016/j.applthermaleng.2016.06.178.

[2]   D.K. Rabha, P. Muthukumar, Performance studies on a forced convection solar dryer integrated with a paraffin wax–based latent heat storage system, Sol. Energy. 149 (2017) 214–226. doi:10.1016/j.solener.2017.04.012.

[3]   A. Reyes, L. Henr?quez-Vargas, J. Rivera, F. Sep?lveda, Theoretical and experimental study of aluminum foils and paraffin wax mixtures as thermal energy storage material, Renew. Energy. 101 (2017) 225–235. doi:10.1016/j.renene.2016.08.057.

[4]   J. Renau, F. Sánchez, A. Lozano, J. Barroso, F. Barreras, Analysis of the performance of a passive hybrid powerplant to power a lightweight unmanned aerial vehicle for a high altitude mission, J. Power Sources. 356 (2017) 124–132. doi:10.1016/j.jpowsour.2017.04.090.

[5]   S. Wilke, B. Schweitzer, S. Khateeb, S. Al-Hallaj, Preventing thermal runaway propagation in lithium ion battery packs using a phase change composite material:

An experimental study, J. Power Sources. 340 (2017) 51–59. doi:10.1016/j.jpowsour.2016.11.018.

[6]   W. Wu, X. Yang, G. Zhang, K. Chen, S. Wang, Experimental investigation on the thermal performance of heat pipe-assisted phase change material based battery thermal management system, Energy Convers. Manag. 138 (2017) 486–492. doi:10.1016/j.enconman.2017.02.022.

[7]   L. Fan, J.M. Khodadadi, Thermal conductivity enhancement of phase change materials for thermal energy storage: A review, Renew. Sustain. Energy Rev. 15 (2011) 24–46. doi:10.1016/j.rser.2010.08.007.

[8]   J.M. Khodadadi, L. Fan, H. Babaei, Thermal conductivity enhancement of nanostructure-based colloidal suspensions utilized as phase change materials for thermal energy storage: A review, Renew. Sustain. Energy Rev. 24 (2013) 418–444. doi:10.1016/j.rser.2013.03.031.

[9]   N.H.S. Tay, M. Liu, M. Belusko, F. Bruno, Review on transportable phase change material in thermal energy storage systems, Renew. Sustain. Energy Rev. 75 (2017) 264–277. doi:10.1016/j.rser.2016.10.069.

[10]   T. Li, J.-H. Lee, R. Wang, Y.T. Kang, Heat transfer characteristics of phase change nanocomposite materials for thermal energy storage application, Int. J. Heat Mass Transf. 75 (2014) 1–11. doi:10.1016/j.ijheatmasstransfer.2014.03.054.

[11]   L. Fan, J.M. Khodadadi, An experimental investigation of enhanced thermal conductivity and expedited unidirectional freezing of cyclohexane-based nanoparticle suspensions utilized as nano-enhanced phase change materials (NePCM), Int. J. Therm. Sci. 62 (2012) 120–126. doi:10.1016/j.ijthermalsci.2011.11.005.

[12]   L. Fan, J.M. Khodadadi, A Theoretical and Experimental Investigation of Unidirectional Freezing of Nanoparticle-Enhanced Phase Change Materials, J. Heat Transfer. 134 (2012) 92301. doi:10.1115/1.4006305.

[13]   V. Kumaresan, R. Velraj, S.K. Das, The effect of carbon nanotubes in enhancing the thermal transport properties of PCM during solidification, Heat Mass Transf. Und Stoffuebertragung. 48 (2012) 1345–1355. doi:10.1007/s00231-012-0980-3.

[14]   Y. Feng, H. Li, L. Li, L. Bu, T. Wang, Numerical investigation on the melting of nanoparticle-enhanced phase change materials (NEPCM) in a bottom-heated rectangular cavity using lattice Boltzmann method, Int. J. Heat Mass Transf. 81 (2015) 415–425. doi:10.1016/j.ijheatmasstransfer.2014.10.048.

[15]   A. Ebrahimi, A. Dadvand, Simulation of melting of a nano-enhanced phase change material (NePCM) in a square cavity with two heat source-sink pairs, Alexandria Eng. J. 54 (2015) 1003–1017. doi:10.1016/j.aej.2015.09.007.

[16]   M. Jourabian, M. Farhadi, Melting of nanoparticles-enhanced phase change material (NEPCM) in vertical semicircle enclosure: numerical study, J. Mech. Sci. Technol. 29 (2015) 3819–3830. doi:10.1007/s12206-015-0828-0.

[17] M. Bechiri, K. Mansouri, Analytical solution of heat transfer in a shell-and-tube latent thermal energy storage system, Renew. Energy. 74 (2015) 825–838. doi:10.1016/j.renene.2014.09.010.

[18] L.W. Fan, Z.Q. Zhu, Y. Zeng, Q. Ding, M.J. Liu, Unconstrained melting heat transfer in a spherical container revisited in the presence of nano-enhanced phase change materials (NePCM), Int. J. Heat Mass Transf. 95 (2016) 1057–1069. doi:10.1016/j.ijheatmasstransfer.2016.01.013.

[19] M. Li, M. Chen, Z. Wu, J. Liu, Carbon nanotube grafted with polyalcohol and its influence on the thermal conductivity of phase change material, Energy Convers. Manag. 83 (2014) 325–329. doi:10.1016/j.enconman.2014.04.002.

[20] N.S. Dhaidan, J.M. Khodadadi, T.A. Al-Hattab, S.M. Al-Mashat, Experimental and numerical study of constrained melting of n-octadecane with CuO nanoparticle dispersions in a horizontal cylindrical capsule subjected to a constant heat flux, Int. J. Heat Mass Transf. 67 (2013) 523–534. doi:10.1016/j.ijheatmasstransfer.2013.08.001.

[21] L.W. Fan, Z.Q. Zhu, Y. Zeng, Q. Lu, Z.T. Yu, Heat transfer during melting of graphene-based composite phase change materials heated from below, Int. J. Heat Mass Transf. 79 (2014) 94–104. doi:10.1016/j.ijheatmasstransfer.2014.08.001.

[22] R.M. Al Ghossein, M.S. Hossain, J.M. Khodadadi, Experimental determination of temperature-dependent thermal conductivity of solid eicosane-based silver nanostructure-enhanced phase change materials for thermal energy storage, Int. J. Heat Mass Transf. 107 (2017) 697–711. doi:10.1016/j.ijheatmasstransfer.2016.11.059.

[23] S.N.. H. Schiffres Sivasankaran; Maruyama, Shigeo; Shiomi, Junichiro; Malen, Jonathan A., Tunable Electrical and Thermal Transport in Ice-Templated Multi layer Graphene Nanocomposites through Freezing Rate Control, ACS Nano. 7 (2013) 11183–11189. doi:10.1021/nn404935m.

[24] H. Wu, L.T. Drzal, High Thermally Conductive Graphite Nanoplatelet/ Polyetherimide Composite by Precoating: Effect of Percolation and Particle Size, Polym. Compos. (2013) 2148–2153. doi:10.1002/pc.22624.

[25] Q. Zhang, Z. Luo, Q. Guo, G. Wu, Preparation and thermal properties of short carbon fibers/erythritol phase change materials, Energy Convers. Manag. 136 (2017) 220–228. doi:10.1016/j.enconman.2017.01.023.

[26] Y. Cui, C. Liu, S. Hu, X. Yu, The experimental exploration of carbon nanofiber and carbon nanotube additives on thermal behavior of phase change materials, Sol. Energy Mater. Sol. Cells. 95 (2011) 1208–1212. doi:10.1016/j.solmat.2011.01.021.

[27] L.W. Fan, X. Fang, X. Wang, Y. Zeng, Y.Q. Xiao, Z.T. Yu, X. Xu, Y.C. Hu, K.F. Cen, Effects of various carbon nanofillers on the thermal conductivity and energy storage properties of paraffin-based nanocomposite phase change materials, Appl. Energy. 110 (2013) 163–172. doi:10.1016/j.apenergy.2013.04.043.

[28] S. Shaikh, K. Lafdi, K. Hallinan, Carbon nanoadditives to enhance latent energy storage of phase change materials, J. Appl. Phys. 103 (2008). doi:10.1063/1.2903538.

[29] H.C. Brinkman, The Viscosity of Concentrated Suspensions and Solutions, J. Chem. Phys. 20 (1952) 571. doi:10.1063/1.1700493.

[30] T. Nomura, C. Zhu, S. Nan, K. Tabuchi, S. Wang, T. Akiyama, High thermal conductivity phase change composite with a metal-stabilized carbon-fiber network, Appl. Energy. 179 (2016) 1–6. doi:10.1016/j.apenergy.2016.04.070.

[31] T. Qian, J. Li, W. Feng, H. Nian, Enhanced thermal conductivity of form-stable phase change composite with single-walled carbon nanotubes for thermal energy storage, Sci. Rep. 7 (2017) 44710. doi:10.1038/srep44710.

[32] M. Amin, N. Putra, E.A. Kosasih, E. Prawiro, R.A. Luanto, T.M.I. Mahlia, Thermal properties of beeswax/graphene phase change material as energy storage for building applications, Appl. Therm. Eng. 112 (2017) 273–280. doi:10.1016/j.applthermaleng.2016.10.085.

[33] R.J. Warzoha, A.S. Fleischer, Improved heat recovery from paraffin-based phase change materials due to the presence of percolating graphene networks, Int. J. Heat Mass Transf. 79 (2014) 314–323. doi:10.1016/j.ijheatmasstransfer.2014.08.009.

[34] L.W. Fan, X. Fang, X. Wang, Y. Zeng, Y.Q. Xiao, Z.T. Yu, X. Xu, Y.C. Hu, K.F. Cen, Effects of various carbon nanofillers on the thermal conductivity and energy storage properties of paraffin-based nanocomposite phase change materials, Appl. Energy. 110 (2013) 163–172. doi:10.1016/j.apenergy.2013.04.043.

[35] J. Xiang, L.T. Drzal, Investigation of exfoliated graphite nanoplatelets (xGnP) in improving thermal conductivity of paraffin wax-based phase change material, Sol. Energy Mater. Sol. Cells. 95 (2011) 1811–1818. doi:10.1016/j.solmat.2011.01.048.

[36] Y. Zeng, L.W. Fan, Y.Q. Xiao, Z.T. Yu, K.F. Cen, An experimental investigation of melting of nanoparticle-enhanced phase change materials (NePCMs) in a bottom-heated vertical cylindrical cavity, Int. J. Heat Mass Transf. 66 (2013) 111–117. doi:10.1016/j.ijheatmasstransfer.2013.07.022.

Chapter 6 An integrated thermal management system for lithium-ion battery modules with nano-enhanced phase change materials and highly oriented pyrolytic graphite

6.1. Introduction

Electric and hybrid electric vehicles (EV and HEV) are considered as the best near-term candidates to reduce the greenhouse gases emission in the transportation sector. Rechargeable lithium-ion (Li-ion) batteries have high specific energy and energy density relative to other cell chemistries which makes them well-suited for electrification of vehicles. The main barriers to the use of Li-ion batteries in electrical/hybrid vehicles are safety, cost related to cycle and calendar life, and low temperature performance [1]. These challenges are strongly coupled to the thermal effects in the battery. Furthermore, in case of overcharging, a Li-ion battery may undergo thermal runaway and explode due to the decomposition of battery components that generate flammable gaseous species. In addition, heating the battery outside a specific range can accelerate the battery aging and sever capacity fading. Therefore, the goal of battery thermal management system (BTMS) is to increase the lifetime of Li-ion cells by moderating the operating temperature of the cell.

There are two major strategies for thermal management in electric vehicles. An active method by using air or a liquid as coolant [2,3], or a passive approach by employing phase change materials (PCM) [4,5]. Air cooling can moderate the batteries temperature rise, but in aggressive driving cycles and/or at high operating temperatures it will result in a large non-uniform temperature distribution in the battery module [6–8]. This leads to different capacity fading rates for each cell, and as a result the cycle life of the whole pack reduces. Efforts into optimizing the flow channels to improve the temperature uniformity increase the system complexity and cost [9,10]. Liquid cooling with water, oil or refrigerants as the heat transfer medium shows higher thermal efficiency due to the higher heat capacity of liquids compared to air [11]. Various liquid cooling BTMS has been investigated in many studies [3,13–15]. However, these systems require a sophisticated flow pattern and consume more energy and space due to the presence of condenser, evaporator and pumps.

The PCM cooling for BTMS was first introduced by Al-Hallaj and Selman [16] in which the PCM absorbs the heat generated by Li-ion batteries and keep the temperature of the batteries within its melting range. It has been showed that PCM cooling systems benefit from many advantages such as high compactness, low cost, no need for circulatory network, better performance in case of thermal run away and more uniform temperature distribution [17–19]. Despite these, there are some drawbacks in this method such as low

thermal conductivity of PCM, insufficient heat rejection during aggressive operation, and unfavorable thermal inertia.

A serious concern in PCM-based BTMS is the limited latent heat storage of these materials. In extreme conditions such as high battery heat generation and/or high ambient temperature the PCM may run out of available latent heat and fail to control the battery module temperature [20]. Furthermore, the lack of efficient heat rejection from the module may also result in thermal management system failure due to the high thermal inertia of PCM.

These challenges may tackle through two main approaches i.e. enhancing the thermal conductivity of the based-PCM, or increasing the external heat release by utilizing fins or forced convection.

Various methods are proposed to enhance the thermal conductivity of the PCM [21]. The addition of highly conductive carbon-based nanoparticles is considered as an effective approach to increase the thermal conductivity of PCM due to their low densities and intrinsic high thermal conductivities [22]. Enhancing the PCM thermal conductivity will result in a more uniform temperature distribution which can improve the heat rejection from the module to the ambient.

Employing forced air convection to improve the performance of a passive BTMS has been rarely reported in the literature. Fathabadi [23] numerically modeled a battery pack consisting of 20 battery units with 19 distributed ducts and layers of paraffin/expanded graphite as the PCM. This hybrid system with varied convective heat transfer coefficients showed better performance than a similar air cooled system at various ambient temperatures. Ling et al. [24] reported an investigation on a power battery cooling system by using an organic PCM/expanded graphite and forced air cooling system. The results revealed that the forced air cooling system is important to maintain the batteries temperature within the safe limit.

Thermal management investigations in the module and pack levels mentioned above performed by using lumped battery thermal models with heat generation data obtained from experiments. This is due to the significant computational cost required for 3D coupled electrochemical-thermal models. However, accurate assessment of batteries thermal responses to cooling scenarios needs 3D coupled electrochemical-thermal models. The numerical studies on the integrated BTMS are commonly conducted during constant current discharge or discharge. Nevertheless, electric and hybrid electric vehicles driving cycles, and consequently batteries charge/discharge cycles, present complex patterns that cannot be precisely modeled with constant current discharge rates.

In the current work, a paraffin/graphite nanopowder composite is synthesized and its temperature dependent thermophysical properties are characterized experimentally. The nanocomposites as well as highly oriented pyrolytic graphite (HOPG) plates are employed in an Li-ion battery module to provide a novel integrated thermal management system. The numerical model uses a three dimensional coupled electrochemical-thermal simulation approach to assess the batteries thermal behavior during a standard hybrid electric vehicle driving cycle. The performance of the proposed thermal management system is evaluated under various cooling system design parameters, air inlet temperature, and nanocomposite formulations.

Nomenclature

C_p	specific heat ($J\,kg^{-1}\,K^{-1}$)
$\boldsymbol{g}$	gravity acceleration vector ($m\,s^{-2}$)
h	convection heat transfer coefficient ($W\,m^{-2}\,K^{-1}$)
H	container height (m)
$\boldsymbol{I}$	identity matrix
k	thermal conductivity ($W\,m^{-1}\,K^{-1}$)
L	latent heat ($J\,kg^{-1}$)
$\boldsymbol{n}$	normal vector
p	static pressure (Pa)
q''	heat flux ($W\,m^{-2}$)
R	container radius (m)
t	time (s)
T	temperature (K)
T_∞	ambient temperature (K)
$\boldsymbol{u}$	velocity vector ($m\,s^{-1}$)
Greek letters	
μ	dynamic viscosity (Pa.s)
ρ	density ($kg\,m^{-3}$)
ϕ	mass fraction
Subscripts and superscripts	
a	air
ini	initial
max	maximum
np	nanoparticle

6.2. Experiments

6.2.1. Preparation of nanocomposites

An industrial grade paraffin wax with a nominal melting point (Tm) of 333.15K is adopted as the base PCM. The graphite nano-powder is purchased from MK Impex Corp., Ontario, Canada. The materials are used as received without further purification in

all experiments. The nanoparticles at desired weights are added to the melted PCM at 90°C and intensively stirred for 30 minutes to provide a homogeneous mixture. A temperature higher than the PCM melting point is preferred as a relatively low viscosity of the molten PCM facilitates the dispersion of the nanoparticles. A very small amount of PolyVinylPyrrolidone-40 (Sigma-Aldrich, Oakville, Canada) is added to the mixture as a dispersing additive to assure a good dispersion of the nanoparticles in the liquid PCM. Finally, the liquid composite is rigorously sonicated at about 90°C for 2 hours prior to the solvent evaporation. Two samples with different weight fractions of 5% and 10% are prepared. The thermophysical properties of the materials used in this study are listed in Table 6-1.

Table 6-1. Thermophysical properties of the materials used in this study

Property	Paraffin wax	CNF	GNP	Graphite nanopowder
Melting point, K	333.15	-	-	-
Thermal conductivity, Wm^{-1}K^{-1}	Solid: 0.25 Liquid:0.16	-	-	-
Specific heat, Jkg^{-1}K^{-1}	Solid: 1180 Liquid: 2056	-	-	-
Density, kgm^{-3}	910	2100	100	2200
Dynamic viscosity, mPa.s	5.5	-	-	-
Latent heat, kJkg^{-1}	119.3	-	-	-
Characteristic length	-	OD: 400nm Length: 50μm	Thickness:7nm APS: 15μm	APS: 50nm

6.2.2. Thermophysical characterization of nanocomposites

The thermal conductivity of NePCM composites are measured with a C-Therm TCi thermal conductivity analyzer (accuracy better than 5%) using modified transient plane source (MTPS) technique. In each measurement, the solid sample is initially heated to a temperature higher than its melting temperature inside a chamber. The liquid sample is then allowed to solidify onto the sensor surface to assure a uniform thermal contact between the sample and the sensor surface.

The heat capacity, latent heat of fusion, and melting temperature of the NePCM are determined using a differential scanning calorimeter (Mettler-Toledo DSC822). A sample size of around 15-20mg is loaded to the DSC cell and the data is collected for the 2nd run at a rate of 3K/min.

The dynamic viscosity of the liquid nanocomposite samples is measured using a rotational viscometer (Brookfield LVT, Cooksville, Canada) with an accuracy of 1% at

elevated temperatures from about 333K to 363K at an increment of 10K. Temperature control during viscosity measurements is performed using a constant temperature bath.

6.3. Numerical modeling

6.3.1. Battery module cooling system configuration

A 1.3kWh battery pack consisted of 12 modules is considered. Each module contains six 5Ah NCA Li-ion batteries in parallel. Fig. 6-1 shows the schematic of the proposed hybrid battery cooling system with two air cooling channels. Two PCM layers are used between adjacent cells to improve the temperature uniformity of the batteries by absorbing their heat generation at a relatively constant temperature as shown in Fig. 6-1. A thin sheet of HOPG is inserted in PCM layers to improve the heat conduction to the cooling channels and enhance temperature uniformity in the module. The performance of the proposed cooling system is tested under federal urban driving cycle (FUDC) for hybrid electric vehicles.

In this study, the cooling systems are numerically modeled by a half of the module with symmetry boundaries on the outer side of one of the PCM layers.
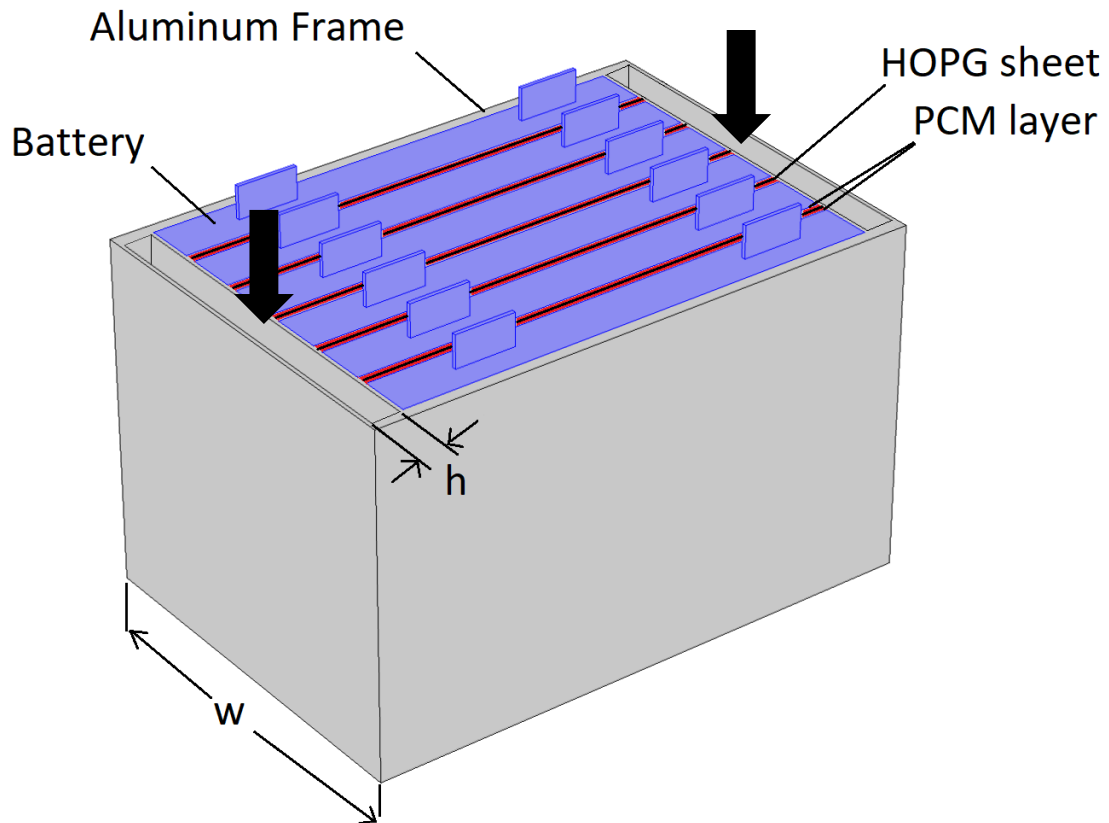
Figure 6-1. Schematic of hybrid cooling system

6.3.2. Battery electrochemical-thermal model

A fast simulation pseudo three dimensional electrochemical-thermal model suitable for thermal analysis has been presented and demonstrated by this research group [25] and is used in this study. The model is based on the coupling of mass, charge, and energy conservations, as well as electrochemical kinetics. The current numerical approach uses a 1D local electrochemical cell unit to find the reaction and polarization heat generations as well as the electrolyte concentration distribution in the active battery material. The values of concentration are inserted in a 3D electric current conservation solver to calculate the distributed Ohmic heat generation. Finally, the 3D energy conservation equation is solved to find the temperature distribution considering three heat generation contributions from anode, cathode and the electrolyte phases.

The pseudo 3D model described above is adapted for a 5Ah NCA battery. The basic parameters of the battery and the module in simulations are listed in Table 6-2 [26–28] and Table 6-3.

Table 6-2. Parameters used in the battery electrochemical-thermal model [26-28]

Parameter (unit)	Al CC	Cathode	Electrolyte	Anode	Cu CC
c_0 (mol/m^3)	-	33956	1000	31507	-
c_p (kJ/kgK)	900	1250	1518	1437	385
D (m^2/s)	-	1.5E-15	*	**	-
E_{aD} (kJ/mol)	-	18	-	4	-
E_{aR} (kJ/mol)	-	3	-	4	-
F (C/mol)	-	-	96487.332	-	-
k (W/mK)	160	1.38	0.099	1.04	400
k_0 (m$^{2.5}$mol$^{-0.5}$/s)	-	3.255E-11	-	1.764E-11	-
r_0 (μm)	-	1.2	-	14.75	-
t_+	-	-	0.363	-	-
α_a, α_c	-	0.5	-	0.5	-
δ(μm)	23	46	26	48	16
ε	-	0.423	0.4	0.56	-
ρ (kg/m^3)	2700	4740	1210	5031	8960
σ (S/m)	3.8E7	91	***	100	6.3E7

$$* \log(D_l) = -\left(4.43 + \frac{54}{T-229-0.005 \times c_l} + 0.0022 \times c_l\right)$$

$$** D_s = \left[3.9 \times 10^{-14}(1.5 - SOC)^{3.5}\right] exp\left[\frac{E_{aD}}{R}\left(\frac{1}{T_{ref}} - \frac{1}{T}\right)\right]$$

$$*** \sigma_l(c_l, T) = 1.2544 \times 10^{-4} c_l \times \left(0.22002 \times 10^{-6} c_l^2 + 0.26235 \times 10^{-3} c_l - \right.$$
$$0.1765 \times 10^{-9} c_l^2 T + 0.93063 \times 10^{-5} c_l T + 0.8069 \times 10^{-9} c_l T^2 - 0.2987 \times 10^{-5} T^2 - $$
$$\left. 8.2488\right)$$

Table 6-3. Specifications of the battery and module used in simulations

Parameter	Value
Battery width (mm)	80
Battery height (mm)	110
Battery thickness (mm)	9
Battery capacity (Ah)	5
Battery tab dimensions (mm)	15×10×0.5 (w×h×t)
Cooling channel height (mm), h	6
PCM layer thickness (mm), t	1, 2, 3
HOPG sheet thickness (mm)	1
Cooling channel width (mm), w	505, 515, 525
Coolant inlet temperature (K)	293.15

6.3.3. Air Flow

Air is considered as the coolant and the flow is assumed to be laminar in all cases due to the low flow velocity and short characteristic lengths in this work. The mass conservation equation of air in the cooling channel is:

$$\nabla \boldsymbol{u} = 0 \tag{6.1}$$

The momentum conservation equation of the coolant is as follow:

$$\rho_a \frac{\partial \boldsymbol{u}}{\partial t} + \rho_a (\boldsymbol{u}.\nabla)\boldsymbol{u} = \nabla.\left[-p\boldsymbol{I} + \mu(\nabla\boldsymbol{u} + (\nabla\boldsymbol{u})^T)\right] \tag{6.2}$$

where ρ_a is the density of air and $\boldsymbol{u}$ is the velocity vector of air in the cooling channel.

The energy conservation equation for air is:

$$\frac{\partial}{\partial t}\left(\rho_a C_{p_a} T_a\right) + \nabla.\left(\rho_a C_{p_a} \boldsymbol{u} T_a\right) - \nabla.(k_a \nabla T_a) = 0 \tag{6.3}$$

where T_a is the temperature of air, and k_a and C_{p_a} are the thermal conductivity and specific heat of air, respectively.

Three initial temperatures of 20, 30 and 40°C are used. The initial temperature of batteries is equal to air inlet temperature which implies that air at ambient temperature is utilized in BTMS. Velocity and pressure boundary conditions are used for the coolant at inlet and outlet boundaries, reactively. A no-slip boundary condition is used on all

internal cooling channel walls. Heat insulation boundary condition is defined at all external boundaries of the battery module.

6.3.4. Heat Transfer in NePCM

The flow of liquid NePCM is assumed unsteady, laminar, Newtonian, and incompressible [29]. It is also assumed that the melted nanocomposite behaves as a continuous medium with thermodynamic equilibrium and no slip velocity between the base PCM and solid nanoparticles. The thermophysical properties of the melted NePCM are assumed constant except the density variation in the buoyancy term which is modeled by the Boussinesq approximation [30]. In the simulations the specific heat of PCM samples are defined based on the DSC curves.

The NePCM samples densities are calculated as follow [31]:

$$\rho_{NePCM} = (1 - \phi)\rho_{PCM} + \phi\rho_{np} \tag{6.4}$$

where ρ_{np} is the density of the nanoparticles, and ϕ is the mass fraction.

The governing equations used in the transient laminar natural convection flow are as follow:

Continuity:

$$\nabla . \boldsymbol{u} = 0 \tag{6.5}$$

Momentum:

$$\rho_{NePCM} \frac{\partial \boldsymbol{u}}{\partial t} + \rho_{NePCM}(\boldsymbol{u}.\nabla)\boldsymbol{u} = \nabla . [-p\boldsymbol{I} + \mu(\nabla\boldsymbol{u} + (\nabla\boldsymbol{u})^T)] + \boldsymbol{g}\beta(T - T_{ref}) \tag{6.6}$$

where β is the thermal expansion coefficient of PCM samples which is calculated based on the density variation.

Energy:

$$(\rho C_p)_{NePCM} \frac{\partial T}{\partial t} + (\rho C_p)_{NePCM}\boldsymbol{u}.\nabla T + \nabla . (-k_{NePCM}\nabla T) = 0 \tag{6.7}$$

The boundary and initial conditions are as follow:

$u = w = z = 0 \quad at\ walls$

$$q'' = -k_{NePCM} \frac{\partial T}{\partial n} \quad at \; battety \; surfaces$$

$$\frac{\partial T}{\partial z} = 0 \quad at \; module \; top \; and \; bottom \; surafces$$

$$T_{(x,y,z)} = T_{ini} \quad at \; t = 0$$

The simultaneous governing equations are solved using COMSOL Multiphysics v5.2 based on the finite element method. The specific heat of nanocomposites in the solid and mushy phases are defined as functions of temperature based on values obtained from the DSC measurements and the thermal conductivity in the mushy phase is estimated using a linear interpolation function.

The mesh independency is checked to ensure reliability of the simulation results. In all module designs, free quadrilateral mesh is used at the boundaries with the swept method along the battery thickness direction. The number of elements has been varied from about 750,000 to 1,400,000. The mesh independency study shows that the module temperature distribution is mesh independent when the number of total elements is more than about 1,050,000. Therefore, this mesh design is used in the simulations. A two-way approach is used to couple the electrochemical and thermal solvers. The heat generation contributions are first calculated based on the derived values from electrochemical solver at a constant temperature. Then, the thermal solver uses the battery heat generation to find the temperature distribution in the module. The average of temperature will be used in the battery electrochemical solver in the next time step.

6.4. Results and discussion

6.4.1. Nanocomposite thermophysical properties

Fig. 6-2 shows the thermal conductivity of the pure paraffin and nanocomposites as functions of temperature and concentration. The thermal conductivity of samples at temperatures close to the melting point (60℃) are not shown due to the non-equilibrium state of the materials at this temperature which may result in inaccurate measurements [32]. This figure shows that the thermal conductivity increases with the nanoparticle concentration and it drops during the melting. As can be seen from this figure, the thermal conductivity of the melted nanocomposites (T>60℃) cannot be considered a strong function of temperature or concentration in the liquid phase. During the solidification process, nanoparticles may trap in the wax crystalline structures which increases the stress on the nanoparticles and enhances the effective contact area between the nanoparticle-wax intersections. The internal stress on the nanoparticles is released during the melting and reduces the inter-particle contact area that is observed as a reduction in thermal conductivity enhancement in the liquid phase.
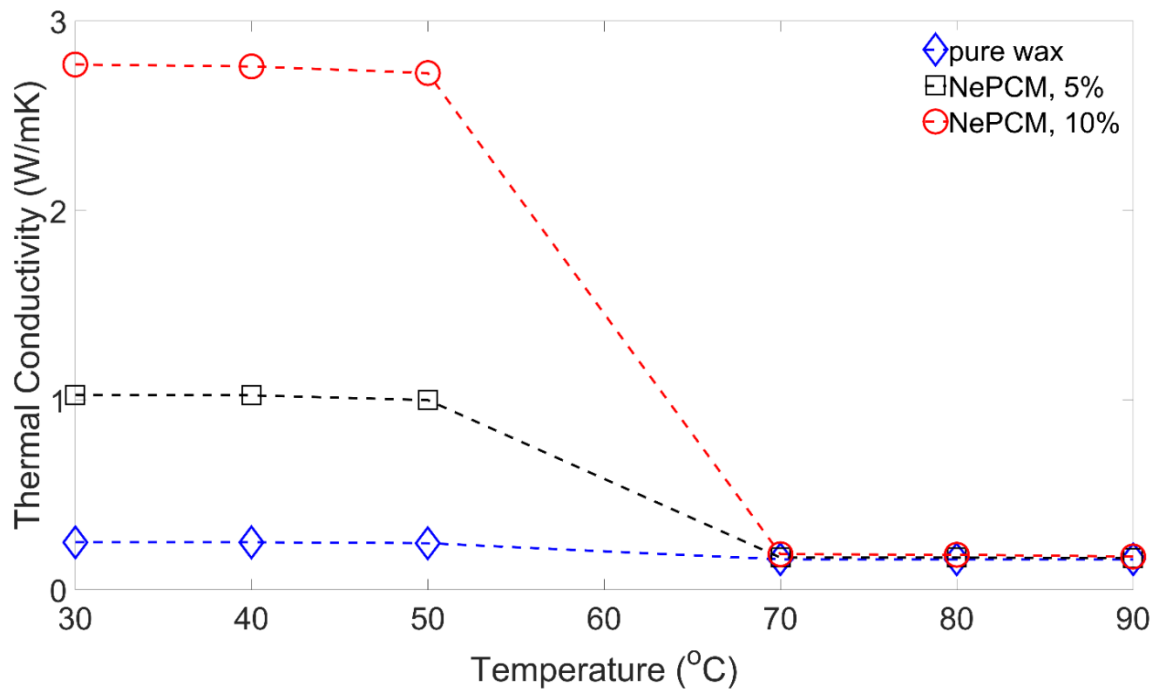
Figure 6-2. Thermal conductivity of PCM samples as a function of mass fraction of nanoparticles and temperature

The average solid and liquid phase thermal conductivity of samples are presented in Table 6-4.

Table 6-4. Average thermal conductivity of pure paraffin and nanocomposites

Sample	Thermal conductivity, Solid/ Liquid (W/mK)
Paraffin wax	0.25/0.16
5 wt% nanocomposite	1.02/0.17
10 wt% nanocomposite	2.75/0.18

Fig. 6-3(a) shows the results of the DSC analysis of NePCM samples at various mass concentrations. The melting and freezing processes of the composites are demonstrated by the upper and under curves, respectively. It seems that the melting point of paraffin wax does not change considerably by adding different nanoparticles.

The enthalpies are calculated by integration the peaks above the baseline by the DSC software and are compared in Fig. 6-3(b). The NePCM latent heats of fusion are degraded

compared to pure wax because of the accumulative replacement of the paraffin wax with nanoadditives.
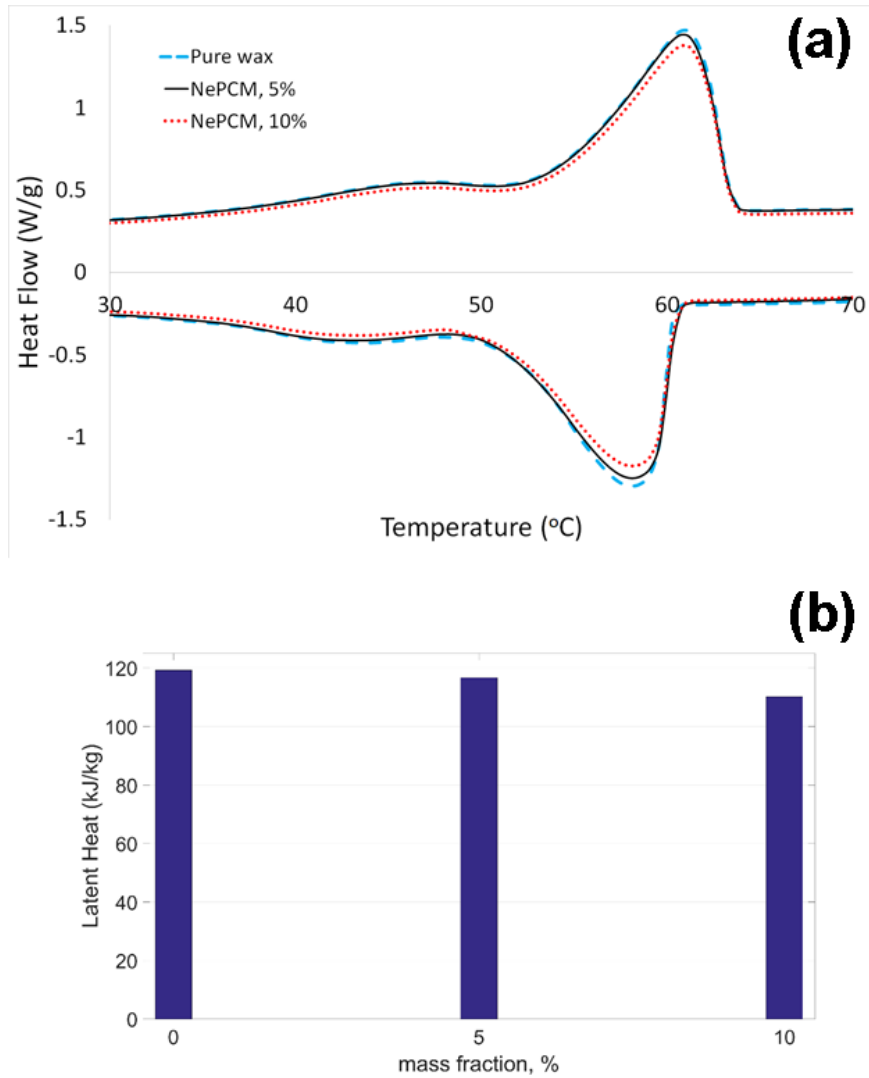
Figure 6-3. (a) DSC heating and cooling curves of various PCM samples, (b) Phase change enthalpy PCM samples as a function of mass fraction of nanoparticles

The measured viscosities of the various nanocomposites are presented in Fig. 6-4. As shown in this figure, the values of viscosity increase drastically with nanoparticles concentration. The measured values of viscosity decrease with temperature and the reduction becomes more noticeable at both higher temperatures and concentrations.
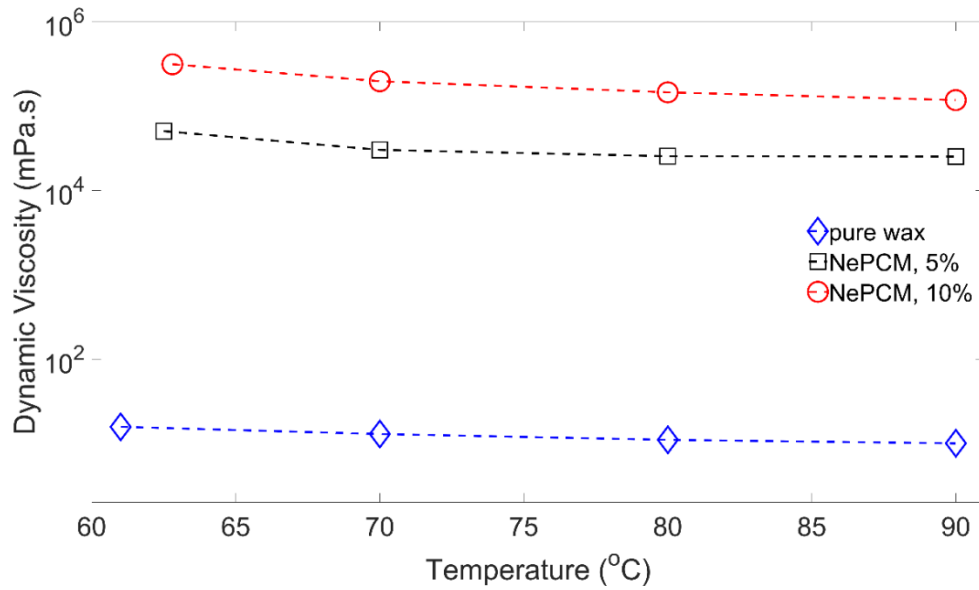
Figure 6-4. Dynamic viscosity of PCM samples as a function of mass fraction and temperature

6.4.2. PCM-based cooling system

In this section, the simulations are performed under HEV federal urban driving cycle (FUDC) [33]. The FUDC is applied to the described battery pack to evaluate the variation of batteries C-rate with time. The pseudo 3D battery model is employed into each cooling system to assess their impact on the battery module performance under the driving cycle. In particular, the effects of the air inlet temperature, nanoparticles mass fraction and thickness of PCM layer on average and local module temperatures are explored.

In this study, an initial value of SOC=70% is used in all simulations [34,35]. Fig. 6-5 shows the variation of a battery C-rate and volumetric heat generation during the driving cycle. In this figure, the positive and negative values of C-rate correspond with discharge and charge of the battery, respectively. High charge and discharge currents, as shown in Fig. 6-5, generate a considerable amount of heat in the batteries which shows the necessity of an effective cooling strategy.
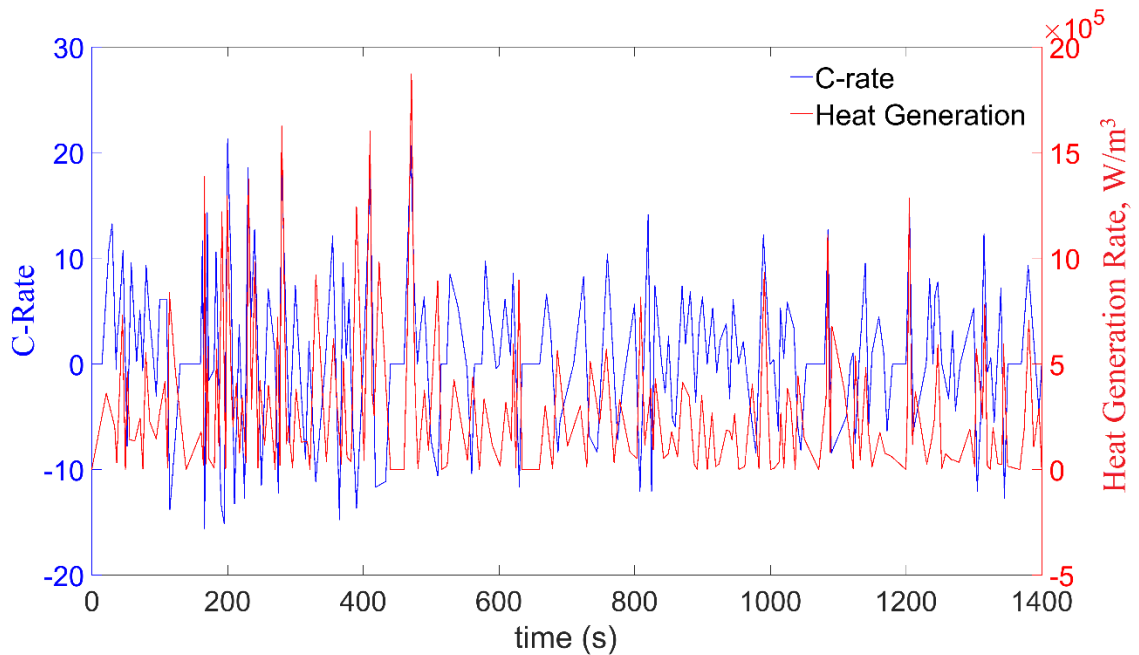
Figure 6-5. Variation of batteries C-rate and heat generation during the driving cycle

The module temperature distribution with different PCM at the end of driving cycle is shown in Fig. 6-6. The cooling plates and channels, as well as the battery tabs are not shown so that the temperature distribution along the battery thickness can be observed clearly. In all cases, the maximum temperature occurs at the center of the module because the inner battery is surrounded by two heat generation sources which result in more heat accumulation and consequently more temperature non-uniformity. Table 6-5 presents the maximum and average temperatures during the driving cycle. In this table, battery 1 represents the battery close to the module exterior wall and number 3 is the inner battery close to the symmetry boundary condition. Utilizing a higher nanoparticle mass fraction reduces both maximum and average battery temperatures due to higher heat conduction from the batteries to the air. However, this cooling system configuration cannot provide a relatively uniform temperature in the module. Adding nanoparticles has two main effects on the base PCM: it increases the solid phase thermal conductivity and decreases the latent heat. The improved temperature distribution at higher mass fraction implies that the main reason of large temperature non-uniformity in the module is the low heat conduction. Therefore, attempts to improve the current design should focus on enhancing the effective thermal conductivity in the module.
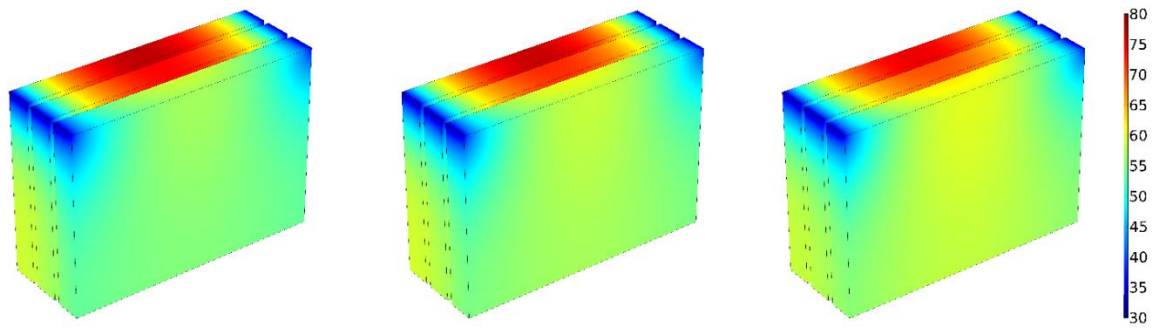
Figure 6-6. Temperature distribution in the module without HOPG sheet using pure wax (left), 5% NePCM (center) and 10% NePCM (right) at the end of driving cycle

Table 6-5. The maximum and average battery temperatures

PCM	Maximum/Average Temperature (^{o}C)		
	Battery 1	Battery 2	Battery 3
Pure wax	64.6/50.2	81.6/56.1	83.9/57.4
Nanocomposite, 5%	65.5/51.1	79.6/55.6	82.4/57.2
Nanocomposite, 10%	66.8/52	78.3/55.0	81.7/69.0

6.4.3. PCM/HOPG-based cooling system

In order to enhance the heat conduction in the battery module, a highly oriented pyrolytic graphite (HOPG) sheet with extremely high thermal conductivity is adopted as a heat spreader. HOPG sheets covered in two layers of PCM (Fig. 6-1) are used to transport heat out of the module through conduction, and then to reject it to the cooling air. HOPG sheets are highly conductive, flexible, chemically inert and non-corrosive which make them promising materials for effective thermal management of compact electric devices. The thermophysical properties of the commercial HOPG used in this study are shown in Table 6-6.

Table 6-6. Thermophysical properties of HOPG

Property	Value
Density (kg/m^3)	2300
Specific heat (J/kgK)	730

Thermal conductivity (W/mK)	In-plane: 1600
	Out-of-plane: 8

6.4.3.1. Effects of PCM layer thickness

A series of simulations is conducted to evaluate the effects of PCM layer thickness on the thermal performance of the proposed BTMS. All simulations have the same initial and air inlet temperature (30°C) and are conducted for a HOPG sheet thickness equal to 1mm. Three values of PCM layer thickness namely 1, 2 and 3mm are investigated. Any change in the thickness of plates will change the cooling channel hydraulic diameter, and consequently, the Reynolds number. In order to evaluate the effect of cooling plate thickness, the inlet velocity is appropriately modified to keep the Reynolds number at a constant value of 1000 in all cases.

Fig. 6-7 shows the variation of module average temperature rise (the average temperature of all three batteries) with time for three PCM samples at various thicknesses. As can be seen from this figure, for each sample the average temperature decreases with the thickness of PCM layer. When a thicker layer is used both latent heat capacity and heat transfer area between the PCM and the cooling channels increase which lead to a lower average battery temperature.
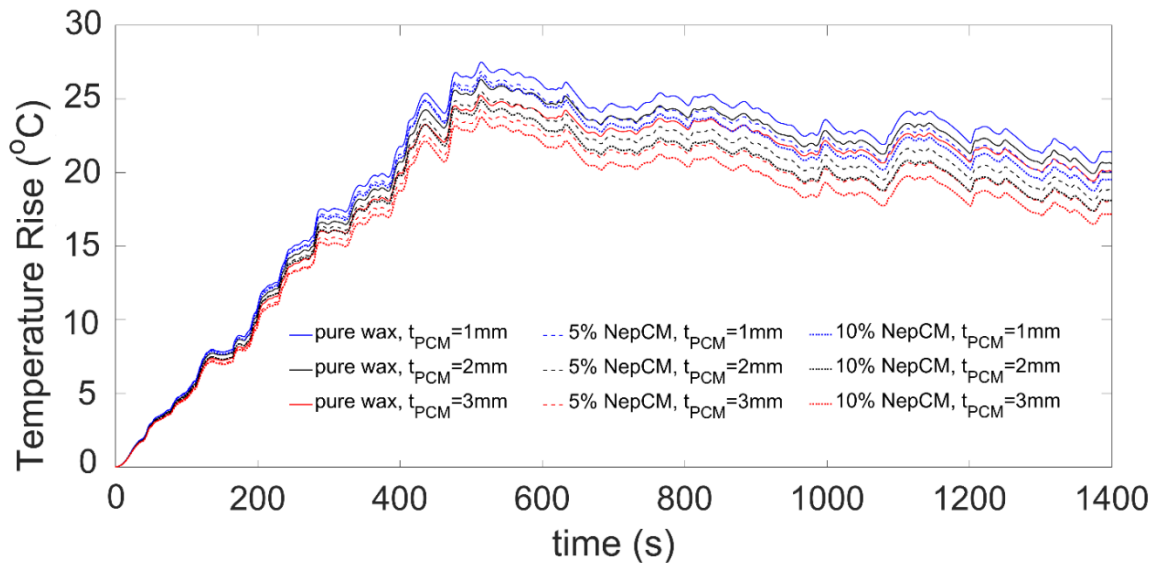
Figure 6-7. Variation of batteries average temperature under various PCM layer thicknesses

For a constant PCM layer thickness, utilizing the nanoparticles can reduce the batteries temperature due to more heat conduction to the cooling channels. Quantitative analysis shows that using a 2mm thick layer of 5% and 10% NePCM samples can maintain batteries temperature about 1.2°C and 1.9°C lower compared to the pure wax.

Among the main factors influencing the performance and capacity fading of Li-ion batteries are the average and gradient of temperature. The time average of the batteries temperature difference is of interest because of multiple repetitions of the drive cycle in HEV which can be defined as follow:

$$\Delta T = \max[\frac{1}{t_{cycle}} \int_{t=0}^{t_{cycle}} \left(T_{max(t),i} - T_{ave(t),i}\right) dt] \qquad 0 < t < 1400 \qquad (6.8)$$

where $i=1, 2, 3$ represents each battery in the simulated module, and t_{cycle} is the driving cycle duration (1400 s).

Fig. 6-8 shows the effects of PCM layer thickness on the batteries average temperature and average temperature difference. As mentioned before, the average temperature decreases with increasing the thickness of all PCM samples studied. However, figure 8 depicts that the average temperature difference slightly increases with PCM layer thickness in all cases. Increasing the thickness causes more heat accumulation in the PCM which forms higher temperature spots in the module. The results suggest that there is a trade-off between the average rise and uniformity of temperature which should be considered in the BTMS design.
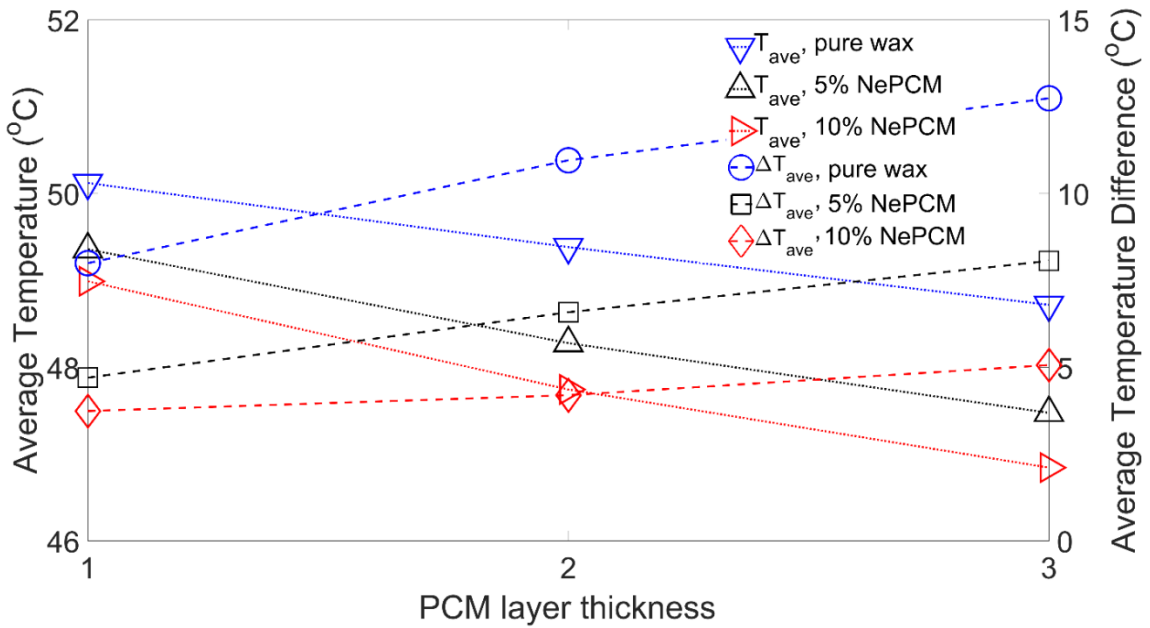
Figure 6-8. Variation of average temperature and average temperature difference in the module with PCM layer thickness

Fig. 6-9 shows the module temperature distribution at the end of driving cycle in two limiting cases studied in this section i.e. 3mm thick pure wax and 1mm thick 10% NePCM. In the pure wax system, the inner batteries temperature is obviously higher compared to the outer battery. A thick layer of pure paraffin with low thermal conductivity tends to store the batteries heat generation with no effective heat rejection to air, and therefore, fails to keep the battery temperature lower than its melting point. As shown in Fig. 6-9, using a 1mm layer of 10% NePCM can successfully generate a moderate and relatively uniform temperature distribution in the module.
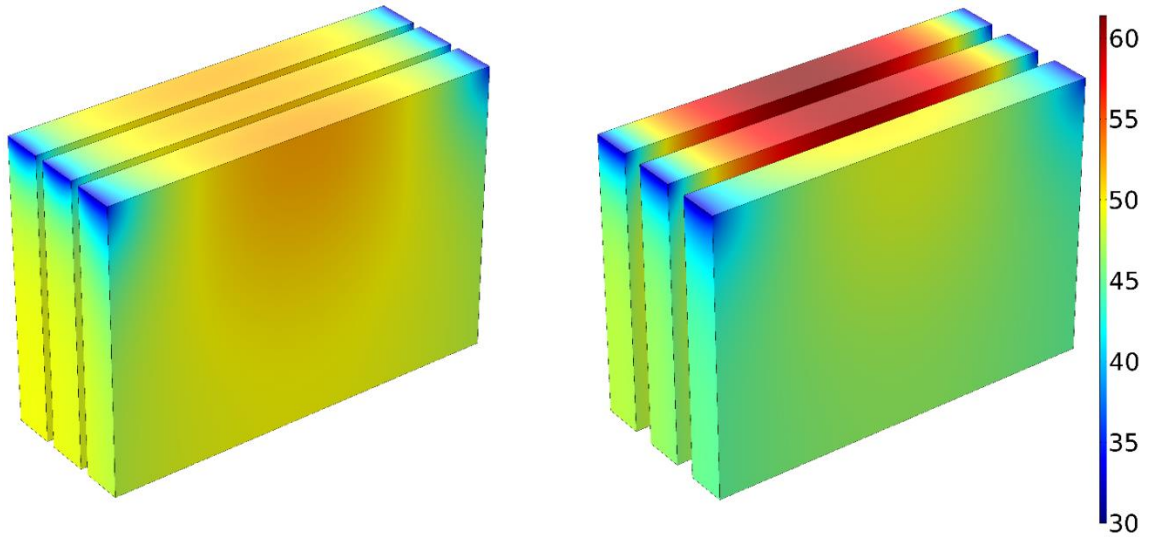
Figure 6-9. Temperature distribution in the module with 1mm thick 10% NePCM (left) and 3mm thick pure wax at the end of driving cycle (right)

6.4.3.2. Effects of air inlet temperature

In addition to the PCM layer thickness, another quantity of interest for assessing the performance of the BTMS is the air inlet velocity. Three values of air temperature namely 20, 30 and 40°C are examined. In the simulations, the initial temperature of batteries is equal to the air inlet temperature which implies the application of air at ambient temperature.

Fig. 6-10 shows the effects of air inlet temperature on the average batteries temperature rise using different PCM samples. A trend similar to the effect of the PCM layer thickness is observed. Higher air inlet temperatures increase the average temperature due to less heat rejection capacity from the batteries to the air. As can be seen from Fig. 6-10, the average temperature is higher in the pure wax design compared to NePCM systems because of its lower thermal conductivity.
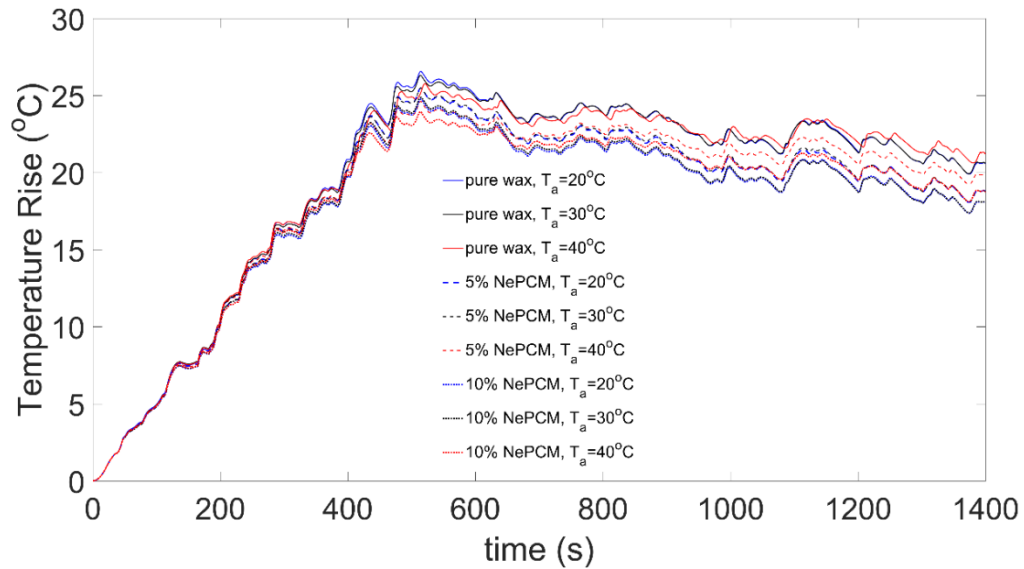
Figure 6-10. Variation of batteries average temperature under various PCM samples and air temperatures

Table 6-7 shows the maximum temperature of batteries under various PCM samples and air temperatures. This table shows that the module thermal performance is a strong function of air temperature and utilizing 5% and 10% mass fraction of nanoparticles can lower the maximum temperature by about 1.0 and 1.7**°**C, respectively.

Table 6-7. Maximum temperature in the module at various air temperatures

PCM sample	$T_a = 20^0C$	$T_a = 30^0C$	$T_a = 40^0C$
Pure wax	46.6	56.3	65.8
NePCM, 5wt%	45.5	55.5	64.6
NePCM, 10wt%	44.7	54.9	64.0

Fig. 6-11 shows the effects of air inlet temperature on the thermal behavior of the battery module. As depicted in this figure, the average temperature increases linearly with the air temperature. However, the average temperature difference increments faster after $T_a = 30^0C$ which shows the effects of PCM layer on enhancing the temperature uniformity in the module at lower air temperatures. At $T_a = 40^0C$ the batteries average is close to the PCM samples melting point (60**°**C) which implies that a thin layer of melted PCM forms close to the batteries. As shown in Fig. 6-2, the thermal conductivity of all PCM samples drops during the melting process which represses the heat conduction from

the batteries and leads to high temperature regions in the module. Therefore, only the solid and mushy phase PCM can absorb heat generation from the batteries surface and improve their temperature uniformity. This suggests that the operation and geometrical parameters should be selected with great care to keep the PCM at temperatures lower than the end of melting temperature.
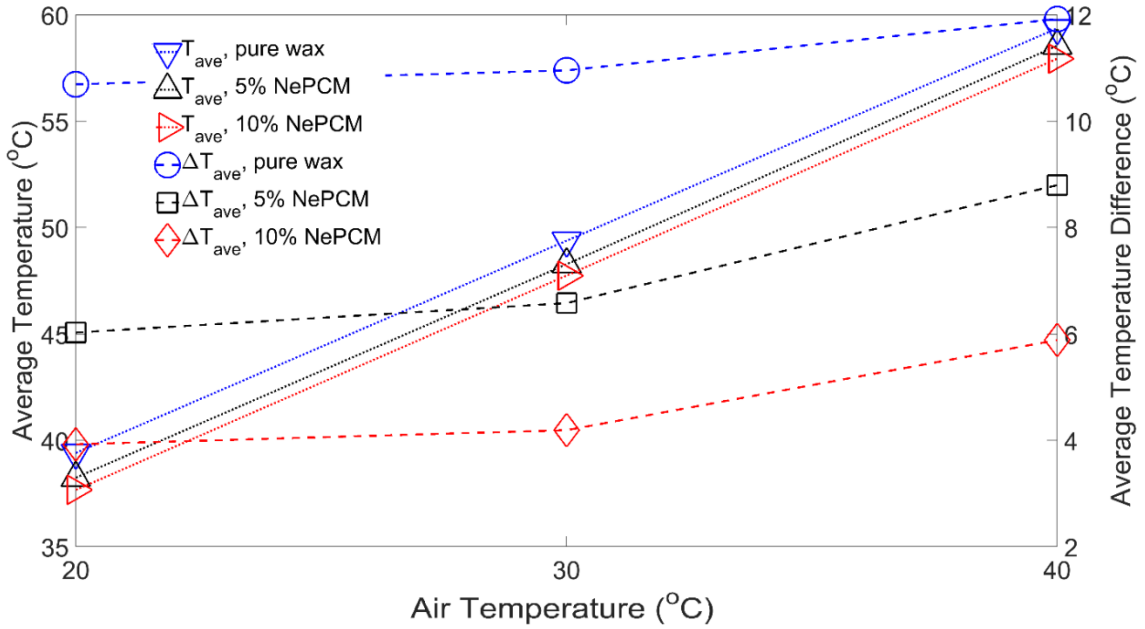
Figure 6-11. Variation of average temperature and average temperature difference in the module with air temperature

In order to further investigate the effects of proposed BTMS design parameters on the module temperature distribution, two dimensionless parameters are defined as follow:

$$\theta = \max(\frac{T_{max(t)} - T_{ave(t)}}{T_{ave(t)}})_i, \quad i = 1, 2, 3 \qquad 0 < t < 1400 \ s \tag{6.9}$$

$$\psi = \frac{\text{Volume of the module}}{\text{Volume of batteries in the module}} - 1 \tag{6.10}$$

θ represents the relative temperature non-uniformity caused by inadequate heat rejection form the batteries and Ψ indicates the module volume increase due to the utilization of the cooling system.

Fig. 6-12 exhibits the effects of PCM layer thickness and air temperature on the dimensionless temperature difference, θ. As shown in this figure, for all PCM samples the temperature distribution is more sensitive to the thickness of the plates (Ψ) and the module temperature uniformity enhances with nanoparticles mass fraction due to higher thermal conductivity of NePCM samples compared to pure wax. This suggests that conduction in the BTMS is the dominant thermal resistance, and optimization attempts should mainly focus on enhancing conduction in the battery module. Additionally, this figure shows that a more compact and effective BTMS design can be achieved by using nano-enhanced PCM compared to pure wax.
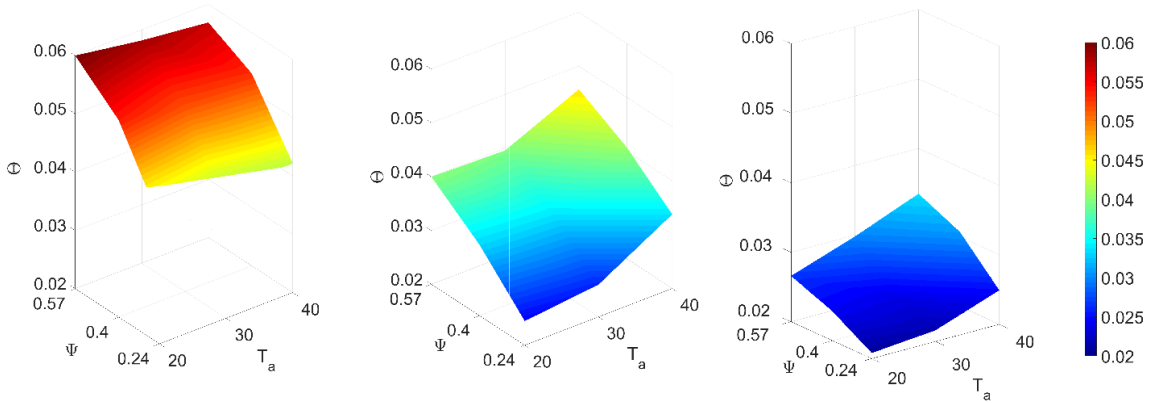
Figure 6-12. Dimensionless temperature difference (θ) in the module as a function of T_a and Ψ under pure wax (left), 5% NePCM (center) and 10% NePCM (right)

As can be seen in Fig. 6-12, when the air temperature increases the pure wax system shows a different trend compared to the NePCM samples. Higher values of air temperature decrease the values of θ in the pure wax system while they increase θ in the NePCM cooling systems. As mentioned above, at elevated values of air temperature a melted layer of the PCM sample is formed close to the batteries surface. The high viscosity of NePCM (Fig. 6-4) degrades the natural convection in the liquid phase materials and leads to a weak heat dissipation from the batteries. However, the natural convection heat transfer in the pure wax improves with temperature which results in lower values of θ at higher air temperatures.

The module temperature distribution at the end of driving cycle is shown in Fig. 6-13. This figure illustrates the results of the limiting cases corresponding to the conditions where the values of θ are maximum and minimum (worst vs best case of temperature uniformity). In both designs, the maximum temperature is shifted to the top center of batteries due to the presence of cooling channels at the sides of batteries. The maximum

136

temperature location is slightly to the left because of higher heat generation in the batteries positive tab.
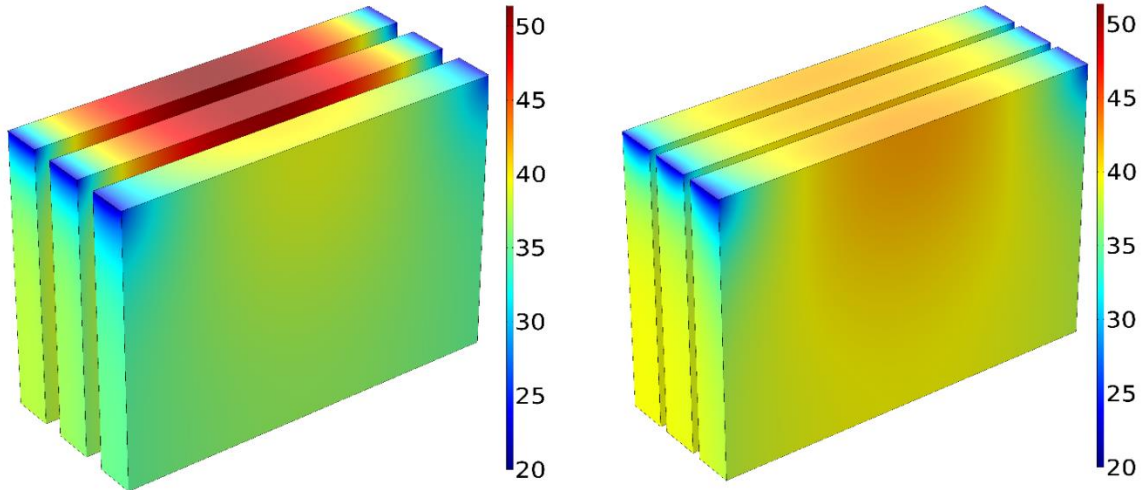
Figure 6-13. Temperature distribution in the module with 3mm thick pure wax (left) and 1mm thick 10% NePCM (right) at the end of driving cycle

Table 6-8 compares the average and maximum temperature of batteries in these designs. Although both designs can maintain the batteries temperature within the safe limits, the high temperature non-uniformities in pure wax system may result in capacity difference between the batteries and lower the lifespan of the module. However, the 10% NePCM system is able to successfully maintain the temperature difference between batteries lower than 0.5°C and the maximum temperature difference over a single battery is 3.9°C (battery #1). Therefore, this design is a promising system to control the temperature of the batteries and keep the module temperature relatively uniform during the driving cycle.

Table 6-8. Average and maximum temperature of batteries under various BTMS designs

Design	Average/Maximum Temperature, °C		
	Battery 1	Battery 2	Battery 3
Pure wax, t=3mm, $T_a = 20^0C$	35.8/40.7	39.5/50.6	40.6/51.2
10% NePCM, t=1mm, $T_a = 20^0C$	38.8/42.7	39.0/42.0	39.3/42.0

Conclusions

A hybrid air-cooled active-passive thermal management system is developed to address the raising concerns regarding the potential failures of passive PCM-based thermal management systems. A fast simulation coupled electrochemical-thermal model is used to predict the thermal responses of Li-ion batteries during a standard driving cycle. The results show that the PCM layer make the active control of air velocity and/or temperature unnecessary or complementary, and therefore provide a simplified, compact and low cost design. The PCM can absorb batteries heat generation during the highly dynamic driving cycles and transfer the stored heat at a relatively constant temperature to the air flow. Furthermore, the presence of PCM enhances temperature uniformity over the batteries surface by absorbing more heat from the region close to the battery tabs.

The techniques used to enhance the thermal conductivity of the pure PCM, i.e. utilizing graphite nanopowder and highly oriented pyrolytic graphite sheets, demonstrate promising capability to solve the problem of inherently low thermal conductivity of the organic PCM. A highly conductive PCM improves the heat transfer from the batteries to the cooling air and maintain the batteries temperature within the safe limits. Forced Air cooling has a critical role in thermal storage capacity recovery of PCM. The lack of effective active cooling may result in heat accumulation and thermal runaway in the battery module.

The proposed strategy offers excellent temperature uniformity among the batteries in the module by using a constant air flow during the driving cycle. The results revealed that there is a trade-off between average temperature and temperature uniformity of batteries that can be achieved by selecting an appropriate thickness of PCM layer. Furthermore, it is experimentally shown that the thermal conductivity of pure wax and NePCM samples drop during the melting process, which may result in the heat accumulation in the material. This suggests that the PCM should remain in the solid or mushy phase during the driving cycle to prevent temperature non-uniformities in the module. The proposed hybrid thermal management system demonstrates advantages such as simple structure, no need for complex coolant control, low operating and maintenance costs and high efficiency compared to conventional cooling systems.

References

[1] T.M. Bandhauer, S. Garimella, T.F. Fuller, A Critical Review of Thermal Issues in Lithium-Ion Batteries, J. Electrochem. Soc. 158 (2011) R1. doi:10.1149/1.3515880.

[2] G. Karimi, X. Li, Thermal management of lithium-ion batteries for electric vehicles, (2013) 13–24. doi:10.1002/er.

[3]   W. Tong, K. Somasundaram, E. Birgersson, A.S. Mujumdar, C. Yap, Numerical investigation of water cooling for a lithium-ion bipolar battery pack, Int. J. Therm. Sci. 94 (2015) 259–269. doi:10.1016/j.ijthermalsci.2015.03.005.

[4]   A. Alrashdan, A.T. Mayyas, S. Al-Hallaj, Thermo-mechanical behaviors of the expanded graphite-phase change material matrix used for thermal management of Li-ion battery packs, J. Mater. Process. Technol. 210 (2010) 174–179. doi:10.1016/j.jmatprotec.2009.07.011.

[5]   S. Wilke, B. Schweitzer, S. Khateeb, S. Al-Hallaj, Preventing thermal runaway propagation in lithium ion battery packs using a phase change composite material: An experimental study, J. Power Sources. 340 (2017) 51–59. doi:10.1016/j.jpowsour.2016.11.018.

[6]   M. Zolot, A. a. Pesaran, M. Mihalic, Thermal Evaluation of Toyota Prius Battery Pack, (2002). doi:10.4271/2002-01-1962.

[7]   L. Fan, J.M. Khodadadi, A.A. Pesaran, A parametric study on thermal management of an air-cooled lithium-ion battery module for plug-in hybrid electric vehicles, J. Power Sources. 238 (2013) 301–312. doi:10.1016/j.jpowsour.2013.03.050.

[8]   R. Sabbah, R. Kizilel, J.R. Selman, S. Al-Hallaj, Active (air-cooled) vs. passive (phase change material) thermal management of high power lithium-ion packs: Limitation of temperature rise and uniformity of temperature distribution, J. Power Sources. 182 (2008) 630–638. doi:10.1016/j.jpowsour.2008.03.082.

[9]   Y. ping Liu, C. zhi Ouyang, Q. bai Jiang, B. Liang, Design and parametric optimization of thermal management of lithium-ion battery module with reciprocating air-flow, J. Cent. South Univ. 22 (2015) 3970–3976. doi:10.1007/s11771-015-2941-8.

[10]   S.K. Mohammadian, Y. Zhang, Thermal management optimization of an air-cooled Li-ion battery module using pin-fin heat sinks for hybrid electric vehicles, J. Power Sources. 273 (2015) 431–439. doi:10.1016/j.jpowsour.2014.09.110.

[11]   Q. Wang, B. Jiang, B. Li, Y. Yan, A critical review of thermal management models and solutions of lithium-ion batteries for the development of pure electric vehicles, Renew. Sustain. Energy Rev. 64 (2016) 106–128. doi:10.1016/j.rser.2016.05.033.

[12]   Z. Rao, S. Wang, A review of power battery thermal energy management, Renew. Sustain. Energy Rev. 15 (2011) 4554–4571. doi:10.1016/j.rser.2011.07.096.

[13]   Y. Huo, Z. Rao, X. Liu, J. Zhao, Investigation of power battery thermal management by using mini-channel cold plate, Energy Convers. Manag. 89 (2015) 387–395. doi:10.1016/j.enconman.2014.10.015.

[14]   L.W. Jin, P.S. Lee, X.X. Kong, Y. Fan, S.K. Chou, Ultra-thin minichannel LCP for EV battery thermal management, Appl. Energy. 113 (2014) 1786–1794. doi:10.1016/j.apenergy.2013.07.013.

[15]   T. Zhang, C. Gao, Q. Gao, G. Wang, M.H. Liu, Y. Guo, C. Xiao, Y.Y. Yan, Status and development of electric vehicle integrated thermal management from BTM to HVAC, Appl. Therm. Eng. 88 (2015) 398–409. doi:10.1016/j.applthermaleng.2015.02.001.

[16]   S. Al Hallaj, J.R. Selman, A Novel Thermal Management System for Electric Vehicle Batteries Using Phase-Change Material, J. Electrochem. Soc. 147 (2000) 3231. doi:10.1149/1.1393888.

[17]   X. Duan, G.F. Naterer, Heat transfer in phase change materials for thermal management of electric vehicle battery modules, Int. J. Heat Mass Transf. 53 (2010) 5176–5182. doi:10.1016/j.ijheatmasstransfer.2010.07.044.

[18]   N. Javani, I. Dincer, G.F. Naterer, B.S. Yilbas, Heat transfer and thermal management with PCMs in a Li-ion battery cell for electric vehicles, Int. J. Heat Mass Transf. 72 (2014) 690–703. doi:10.1016/j.ijheatmasstransfer.2013.12.076.

[19]   W.Q. Li, Z.G. Qu, Y.L. He, Y.B. Tao, Experimental study of a passive thermal management system for high-powered lithium ion batteries using porous metal foam saturated with phase change materials, J. Power Sources. 255 (2014) 9–15. doi:10.1016/j.jpowsour.2014.01.006.

[20]   R. Kizilel, A. Lateef, R. Sabbah, M.M. Farid, J.R. Selman, S. Al-Hallaj, Passive control of temperature excursion and uniformity in high-energy Li-ion battery packs at high current and ambient temperature, J. Power Sources. 183 (2008) 370–375. doi:10.1016/j.jpowsour.2008.04.050.

[21]   L. Liu, D. Su, Y. Tang, G. Fang, Thermal conductivity enhancement of phase change materials for thermal energy storage: A review, Renew. Sustain. Energy Rev. 62 (2016) 305–317. doi:10.1016/j.rser.2016.04.057.

[22]   J.M. Khodadadi, L. Fan, H. Babaei, Thermal conductivity enhancement of nanostructure-based colloidal suspensions utilized as phase change materials for thermal energy storage: A review, Renew. Sustain. Energy Rev. 24 (2013) 418–444. doi:10.1016/j.rser.2013.03.031.

[23]   H. Fathabadi, High thermal performance lithium-ion battery pack including hybrid active–passive thermal management system for using in hybrid/electric vehicles, Energy. (2014). doi:10.1016/j.energy.2014.04.046.

[24]   Z. Ling, F. Wang, X. Fang, X. Gao, Z. Zhang, A hybrid thermal management system for lithium ion batteries combining phase change materials with forced-air cooling, Appl. Energy. 148 (2015) 403–409. doi:10.1016/j.apenergy.2015.03.080.

[25] F. Bahiraei, M. Ghalkhani, A. Fartaj, G.-A. Nazri, A pseudo 3D electrochemical-thermal modeling and analysis of a lithium-ion battery for electric vehicle thermal management applications, Appl. Therm. Eng. (2017). doi:10.1016/j.applthermaleng.2017.07.060.

[26] Y. Tang, M. Jia, J. Li, Y. Lai, Y. Cheng, Y. Liu, Numerical Analysis of Distribution and Evolution of Reaction Current Density in Discharge Process of Lithium-Ion Power Battery, J. Electrochem. Soc. 161 (2014) E3021–E3027. doi:10.1149/2.004408jes.

[27] C.R. Pals, J. Newman, Thermal Modeling of the Lithium / Polymer Battery - II. Temperature profiles in cell stack, J. Electrochem. Soc. 142 (1995) 3282–3288. doi:10.1149/1.2049975.

[28] A. Eddahech, O. Briat, J.M. Vinassa, Thermal characterization of a high-power lithium-ion battery: Potentiometric and calorimetric measurement of entropy changes, Energy. 61 (2013) 432–439. doi:10.1016/j.energy.2013.09.028.

[29] N.S. Dhaidan, J.M. Khodadadi, T.A. Al-Hattab, S.M. Al-Mashat, Experimental and numerical study of constrained melting of n-octadecane with CuO nanoparticle dispersions in a horizontal cylindrical capsule subjected to a constant heat flux, Int. J. Heat Mass Transf. 67 (2013) 523–534. doi:10.1016/j.ijheatmasstransfer.2013.08.001.

[30] Y. Feng, H. Li, L. Li, L. Bu, T. Wang, Numerical investigation on the melting of nanoparticle-enhanced phase change materials (NEPCM) in a bottom-heated rectangular cavity using lattice Boltzmann method, Int. J. Heat Mass Transf. 81 (2015) 415–425. doi:10.1016/j.ijheatmasstransfer.2014.10.048.

[31] L.W. Fan, Z.Q. Zhu, Y. Zeng, Q. Lu, Z.T. Yu, Heat transfer during melting of graphene-based composite phase change materials heated from below, Int. J. Heat Mass Transf. 79 (2014) 94–104. doi:10.1016/j.ijheatmasstransfer.2014.08.001.

[32] R.M. Al Ghossein, M.S. Hossain, J.M. Khodadadi, Experimental determination of temperature-dependent thermal conductivity of solid eicosane-based silver nanostructure-enhanced phase change materials for thermal energy storage, Int. J. Heat Mass Transf. 107 (2017) 697–711. doi:10.1016/j.ijheatmasstransfer.2016.11.059.

[33] H. Care, S. Net, E. Marion, E. Lewin, S. Altman, C. Market, M. Care, F. Viability, S.N. Providers, M. Isbn, T. Pdf, N.A. Press, N. Academy, National Research Council. Review of the Research Program of the Partnership for a New Generation of Vehicles, fourth report, National Research Council, Washington, DC, 2000.

[34] A. Santucci, A. Sorniotti, C. Lekakou, Power split strategies for hybrid energy storage systems for vehicular applications, J. Power Sources. 258 (2014) 395–407. doi:10.1016/j.jpowsour.2014.01.118.

[35]   K. Gokce, A. Ozdemir, A Rule Based Power Split Strategy for Battery /
Ultracapacitor Energy Storage Systems in Hybrid Electric Vehicles, Int. J.
Electrochem. Sci. 11 (2016) 1228–1246.

Chapter 7 Conclusions

The conclusions of different parts of the present study were discussed extensively in chapters 2 to 6. In chapter 7, the overall conclusions and the main contribution of this research are summarized and suggestions for future works are also presented.

The main challenges for the deployment of Li-ion batteries in electric vehicles, including capacity/power fade and thermal runaway, are coupled to the thermal behavior of the battery modules. Ideally, all batteries in a module should operate within an identical narrow temperature range. A number of methods have been proposed to control the operating temperature of batteries in electric vehicles by using active or passive techniques. A reliable prediction of the effectiveness of these methods requires an accurate and computationally affordable modeling of the heat generation in Li-ion batteries.

In working towards this goal, understanding the effects of various thermal management design and operating parameters on the electrochemical-thermal responses of batteries are pursued in this research. At the first step, a new streamlined coupled modeling approach was developed. The model was employed in active, pure passive and hybrid active-passive thermal management systems to determine the most efficient design in terms of temperature uniformity. To achieve the goals of this study, a series of nanocomposite phase change materials are synthesized and characterized to be employed in the battery cooling system.

In this chapter, the performance of various thermal management approaches studied in the previous chapters are compared, and the concluding remarks are summarized.

7.1. Concluding Remarks

To conduct an overall investigation on the effect of all studied thermal management systems on the batteries thermal behavior, the variation of their average temperature with time are compiled and shown in Figure 7-1. The battery temperature during the driving cycle under single and double channel liquid, as well as 10% PCM/HOPG hybrid cooling systems is shown in this figure. In all systems, the module total volume ($\psi \approx 37\%$), coolant inlet Reynolds number (Re=1000) and temperature (Tin=20°C), as well as initial temperature (T0=20°C) are identical.

The operating temperature of NCA Li-ion batteries should be kept lower than 60°C for their safe performance. As can be seen in the Fig 7-1, all systems can successfully maintain the module average temperature in the safe limits. The batteries experience the

minimum and maximum temperature rise under liquid double channel and hybrid PCM/HOPG systems, respectively. Generally, the performance of Li-ion batteries improves with temperature due to lower electrolyte resistance at higher temperatures. Therefore, the electrochemical efficiency of batteries is higher when the hybrid PCM/HOPG system is utilized.
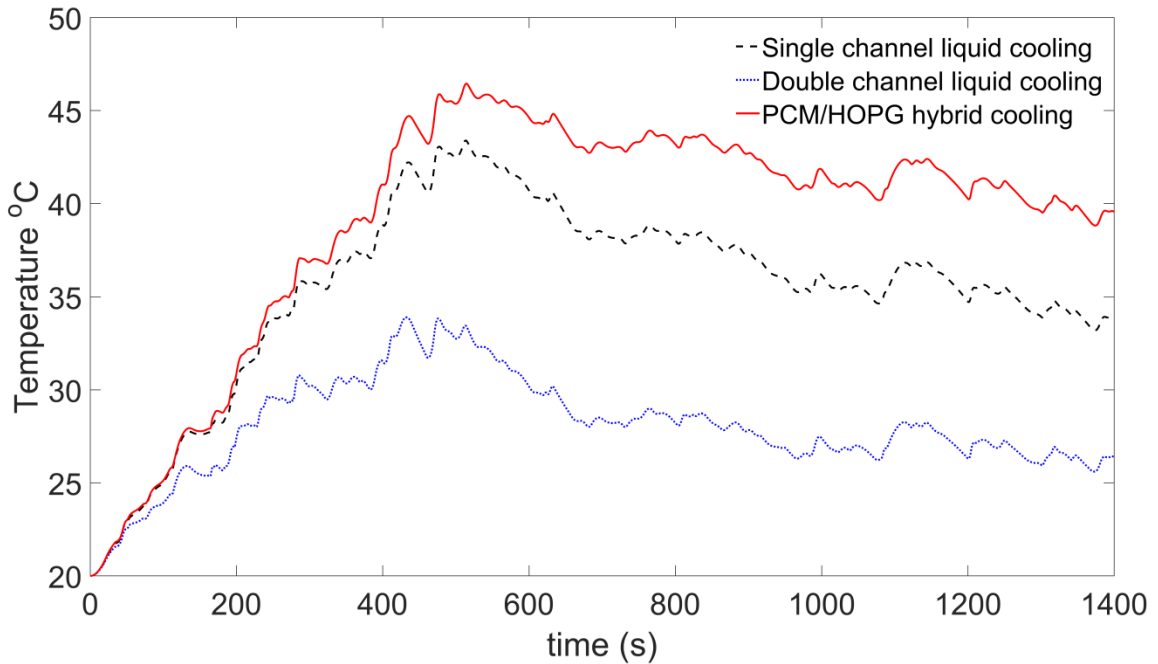
Figure 7-1. Module average temperature variation during the driving cycle under various cooling systems

The average temperature of individual batteries under the cooling systems is listed in Table 7-1. A cooling method with lower temperature difference among batteries will minimize the risk of SOC mismatch between the batteries and will enhance the module performance and lifespan.

Table 7-1. Average battery temperature under various cooling systems

Cooling system	Average Temperature (^{o}C)		
	Battery #1	Battery #2	Battery #3
Single channel liquid	34.8	35.6	35.9
Double channel liquid	27.5	28.2	28.4
10% PCM/HOPG hybrid	38.8	39.0	39.3

Table 7-1 shows that the PCM/HOPG hybrid system provides the most uniform temperature distribution amongst the batteries. In this table battery #1 and #3 are the outermost and innermost batteries in the module, respectively. The values of average temperature of batteries #2 and #3 are close in all thermal management methods, however, there is a relatively big difference between the temperature of battery #1 and #2 in the liquid systems. The inner batteries are surrounded by two heat generation sources which increases their temperature compared to the outer battery. In the PCM/HOPG system, the thin layers of NePCM absorb the inner batteries heat generation and prevent heat accumulation, and consequently, large temperature difference between the inner and outer batteries. The maximum difference between two individual battery temperatures is 1.1oC, 0.9°C and 0.5°C in single channel, double channel and PCM/HOPG systems, respectively.

The non-uniform temperature distribution in a battery may lead to localized deterioration of battery liquid electrolyte which will accelerate the capacity fading of the cells. The temperature distribution over the batteries surface under the three cooling scenarios mentioned is illustrated in Fig. 7-2.
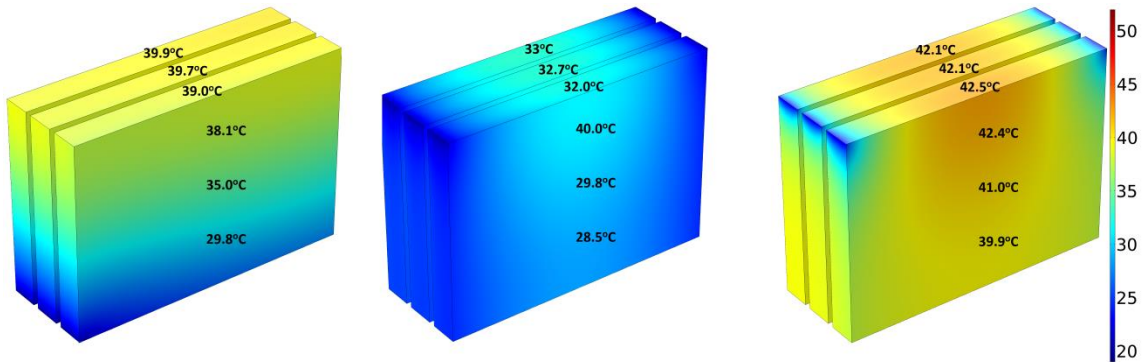
Figure 7-2. Temperature distribution of batteries under single channel (left), double channel (center), and 10% PCM/HOPG (right) systems

The temperature at the center of the upper battery surface and different heights ($z/h_{battery}$=0.9, 0.6, 0.3) are shown for more clarification. As shown in this figure, the hybrid system offers the most uniform temperature distribution compared to other cooling system. As discussed in chapter 3, current density in very high in the vicinity of tabs at the top of batteries due to constriction of the current flow. This leads to higher heat generation, and consequently, higher temperatures at the top of batteries. In the hybrid system, the NePCM layer absorbs more heat at warmer areas in a relatively constant temperature which leads to a more uniform temperature distribution. The heat

stored in the NePCM is transferred to the cooling air through HOPG sheets. The temperature difference along the battery height in the single channel, double channel and PCM/HOPG systems are 8.3, 11.5, and 2.5oC, respectively which represents the superior temperature uniformity of the PCM/HOPG system. In the double channel and hybrid designs, the maximum temperature is shifted to the top center of batteries due to the presence of channels at the sides of batteries, while in the single channel design system the maximum temperature located at the top right of the batteries due to flow direction from left to right.

In this study 67 cooling system configurations, including 20 single channel, 20 double channel and 27 PCM-based systems, are investigated. Fig 7-3 summarizes the dimensionless temperature difference (θ) of all configurations investigated. As shown in this figure, the 10% PCM/HOPG system provides the most uniform temperature distribution at the smallest volume consumption (ψ=0.24% at Fig 7-3 (e)). This figure depicts another advantage of the proposed hybrid system which is more uniform temperature distribution at a more compact configuration. In both liquid cooling systems (Fig. 7-3 (a) and (b)), a more uniform temperature distribution is achievable only at the expense of a bulkier design, however, in the PCM-based systems the temperature is more uniform at smaller system sizes (smaller values of ψ).
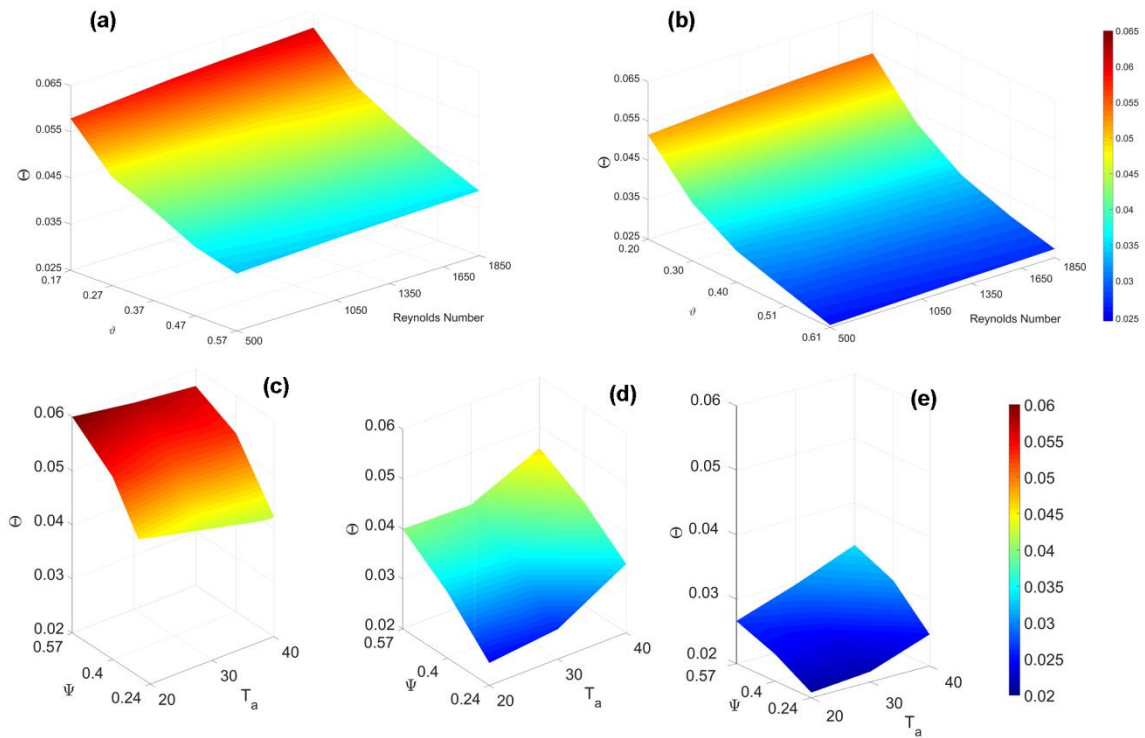
Figure 7-3. Dimensionless temperature variation in (a) single channel active, (b) double channel active, (c) pure wax hybrid, (d) 5% NePCM hybrid, and (e) 10% NePCM hybrid cooling systems

It may be concluded the cooling method operating and design conditions, such as coolant flow rate and inlet temperature, and the thickness of heat spreader plates, strongly affect the thermal behavior of Li-ion battery modules in HEV. Eventually, integrating the active air cooling with the improved PCM-based passive thermal storage system showed the best thermal performance among the thermal management systems examined.

7.2. Suggested future works

A coupled electrochemical-thermal modeling approach of Li-ion batteries is developed and used to evaluate the thermal responses of battery modules under different thermal management systems. The assessments were based on a single FUDC driving cycle. It is a good idea to investigate the performance of cooling systems after multiple repetitions of the driving cycle.

Furthermore, the effects of the contact resistance in the battery cell components, as well as the battery capacity fade are neglected. The battery model can be extended to include the effects of the electrical and thermal contact resistance between the cell components, and the effects of solid electrolyte interface (SEI) layer which can result in more accurate

estimations of the temperature gradient, capacity fade and rate capability of the Li-ion batteries.

To design an optimal BTMS, it is worthy to assess the effects of the cooling system on the capacity fade and rate capability of the batteries after multiple repetitions of the driving cycle.

Chapter 8 Uncertainty Analysis

A.1. Introduction

In this chapter some details of uncertainty analysis of PCM-based samples thermophysical properties measurements are explained.

The total uncertainty associated with each parameter consists of bias and precision uncertainties [1]. The sources of uncertainty that are assumed to be constant for the duration of the tests and are associated with the instrument result in the bias error (B_i).

Random uncertainty, that cause scatter in the data, is obtained using the standard deviation of the elemental random source i, as follows:

$$S_{x,i} = [\frac{\sum_{j=1}^{N_i}(x_{i,j} - \bar{x}_i)}{N_i - 1}]^{1/2}$$

(A.1)

where N_i is the number of data points.

The standard error of the mean for error source i, is calculated as follows:

$$S_{\bar{x},i} = \frac{S_{x,i}}{\sqrt{N_i}}$$

(A.2)

The combined effect of the several random uncertainties on the test result that is calculated by:

$$S_{\bar{x},R} = \left[\sum_{i=1}^{N_i}(S_{\bar{x},i})^2\right]^{1/2}$$

(A.3)

The total uncertainty with 95% confidence (U_{95}) is calculated using the bias uncertainty (b_R), the total random standard uncertainty ($S_{\bar{x},R}$) with the Student's t at 95% confidence (t_{95}) as follows:

$$U_{95} = [b_R^2 + (t_{95}S_{\bar{x},R})^2]^{1/2}$$

(A.4)

The Student's t is determined using the degrees of freedom for the sample ($N_i - 1$) [2].

A.2. Uncertainty analysis of heat capacity measured by DSC

A Mettler-Toledo DSC822 differential scanning calorimeter is used to find the specific and latent heat of PCM samples. The main factors that influence the readings of the DSC

are sensor cleanliness, crucible positioning, vibrations and purge gas flow fluctuations [master thesis]. In each test, brand new aluminum crucibles are used. The crucibles are placed into the measurement chamber by an automatic robotic arm and a two stage gas regulator is used to minimize purge gas (Nitrogen) fluctuations. Three melting-solidification runs per sample without changing the crucibles positions are recorded and the average of the runs is reported.

Commonly, the DSC manufacturers report the bias uncertainty of their instrument using single-crystal sapphire disks under a reference temperature range, purge gas flow and temperature variation rate (in K/min) [3].

The bias uncertainty for the DSC822 used in this investigation is determined by performing heat capacity calculations using a sapphire disk provided by the manufacturer. The known values of heat capacity of sapphire are included in the instrument STARe software based on standard ASTM E-1269-05. The measurements for the both sapphire and PCM samples are carried out with an identical procedure.

The heat capacity of the sapphire samples was indirectly measured by STARe software. The error of the measurement was then determined by subtracting the expected heat capacity value (from ASTM) from the measured value. The results are listed in Table A-1. The average error for the temperature range from 30 to 70°C is $b_R = 0.004$ J/gK.

Table A-4. The measured and reference values of heat capacity of the single-crystal sapphire disk

Temperature, °C	30	40	50	60	70
Reference C_p (J/g.K)	0.780	0.799	0.819	0.838	0.856
Measured C_p (J/g.K)	0.776	0.795	0.815	0.835	0.853

The specific and latent heat of PCM samples are measured using a similar approach. The purge gas flow rate is kept constant at 100 cm^3/min during the measurements. 5 samples of each material are loaded into crucibles and each of the 5 samples is tested consecutively during three heating/cooling cycles without removing them from the measuring crucible. The latent heat is found by integrating the specific heat over the melting temperature range using the STARe software. The average values of latent heat are listed in table A-2.

Table A-2. The measured latent heat of pure wax and nanocomposites

Sample	Latent heat, J/g
Pure wax	119.3
2.5% Graphite	121.4
5% Graphite	116.6
7.5% Graphite	113.5
10% Graphite	110.2
2.5% GNP	120.0
5% GNP	115.9
7.5% GNP	112.4
10% GNP	109.2
2.5% CNF	119.8
5% CNF	115.4
7.5% CNF	112.3
10% CNF	109.1

Using the Student's t for 4 degrees of freedom as 2.776, the maximum uncertainty at 95% confidence (U_{95}) is 4.2%.

A.3. Uncertainty analysis of heat capacity measured by MTPS method

A C-therm thermal analyzer with a measurement range of 0-500 W/mK is used to find the thermal conductivity of PCM samples. The precision uncertainty is calculated using the approach described in the previous section. This instrument accuracy is rated to less than 5% in the range of the thermal conductivities measured in this study. This value is used in calculating the bias uncertainty of measurements.

5 samples of each PCM-based nanocomposite are tested under three consecutive heating/cooling processes between 30°C to 90°C. The consecutive tests minimize the errors caused by the variations in the tested material and contact area between the samples and sensor surface. In all experiments, it is assumed that the thermal equilibrium is achieved when the sample temperature measured by the sensor remains constant (±0.1°C of the specified temperature) after 30 minutes.
The thermal conductivity of samples is directly measured by the thermal analyzer. The average values of the results are listed in table A-3.

Table A-3. The measured viscosity of pure wax and nanocomposites

Sample	Thermal conductivity, W/mK					
	30°C	40°C	50°C	70°C	80°C	90°C
Pure wax	0.250	0.250	0.252	0.163	0.161	0.162
2.5% Graphite	0.703	0.700	0.685	0.165	0.164	0.162
5% Graphite	1.028	1.025	1.004	0.169	0.168	0.167
7.5% Graphite	1.557	1.553	1.512	0.175	0.174	0.174
10% Graphite	2.771	2.762	2.725	0.187	0.184	0.175
2.5% GNP	0.458	0.456	0.440	0.162	0.160	0.160
5% GNP	0.551	0.549	0.525	0.165	0.165	0.163
7.5% GNP	0.624	0.625	0.618	0.168	0.167	0.167
10% GNP	0.703	0.701	0.687	0.170	0.170	0.168
2.5% CNF	0.312	0.310	0.305	0.161	0.161	0.160
5% CNF	0.332	0.330	0.321	0.162	0.162	0.161
7.5% CNF	0.380	0.372	0.364	0.163	0.162	0.161
10% CNF	0.414	0.411	0.401	0.165	0.163	0.162

Using the Student's t for 4 degrees of freedom as 2.776, the maximum uncertainty at 95% confidence (U_{95}) is ±2.6% and ±6.25% for solid and liquid samples, respectively.

A.4. Uncertainty analysis of dynamic viscosity measured by rotational viscometer
A Brookfield LVT viscometer is used to measure the viscosity of the melted PCM samples. During the experiments, the temperature of samples is controlled using a Caron 2050 water bath. All measurements are performed after reaching the thermal stability (±0.1°C change in sample temperature after 60 minutes). The viscometer is accurate to ±1% of any full scale spindle/speed viscosity range, and therefore, this value is used to calculate the uncertainties in all measurements.

Each measurement is repeated five times and the average values are reported in Table A.4.

Table A-4. The measured viscosity of pure wax and nanocomposites

Sample	Dynamic Viscosity, mPa s			
	60°C	70°C	80°C	90°C
Pure wax	15.7	12.9	11	10
2.5% Graphite	838	721	609	532

5% Graphite	50493	30274	25446	25250
7.5% Graphite	134572	97534	84567	75150
10% Graphite	313554	197148	145710	117806
2.5% GNP	739	628	542	496
5% GNP	45501	27111	22508	20724
7.5% GNP	115760	83316	72764	61543
10% GNP	266695	167419	119946	99889
2.5% CNF	536	439	361	329
5% CNF	35850	22195	17993	17174
7.5% CNF	102678	73251	60097	55762
10% CNF	250286	153797	99766	85158

Using the Student's t for 4 degrees of freedom as 2.776, the maximum uncertainty at 95% confidence (U_{95}) is $\pm 3.83\%$.

References

[1]   Figliola, R.S., and Beasley, D.E., 2011, Theory and Design for Mechanical Measurements, 5th edition, John Wiley and Sons, Inc., New York, USA.

[2] Dieck, R.H., 2007, Measurement Uncertainty: Methods and Applications. ISA: The Instrumentation, Systems, and Automation Society, Fourth edition, New York, USA.

[3] Matteo Luisi, 2014, Characterizing the measurement uncertainty of a high-temperature heat flux differential scanning calorimeter. Master of Applied Science thesis, Graz University of Technology.

VITA AUCTORIS

NAME: Farid Bahiraei

PLACE OF BIRTH: Kermanshah, Iran

YEAR OF BIRTH: 1986

EDUCATION: TizHooshan High School, Kermanshah, Iran, 2004

                    Isfahan University of Technology, B.Sc., Isfahan, Iran, 2008

                    Sahand University of Technology, M.Sc., Tabriz, Iran, 2011

                    University of Windsor, Windsor, ON, PhD Candidate, 2017